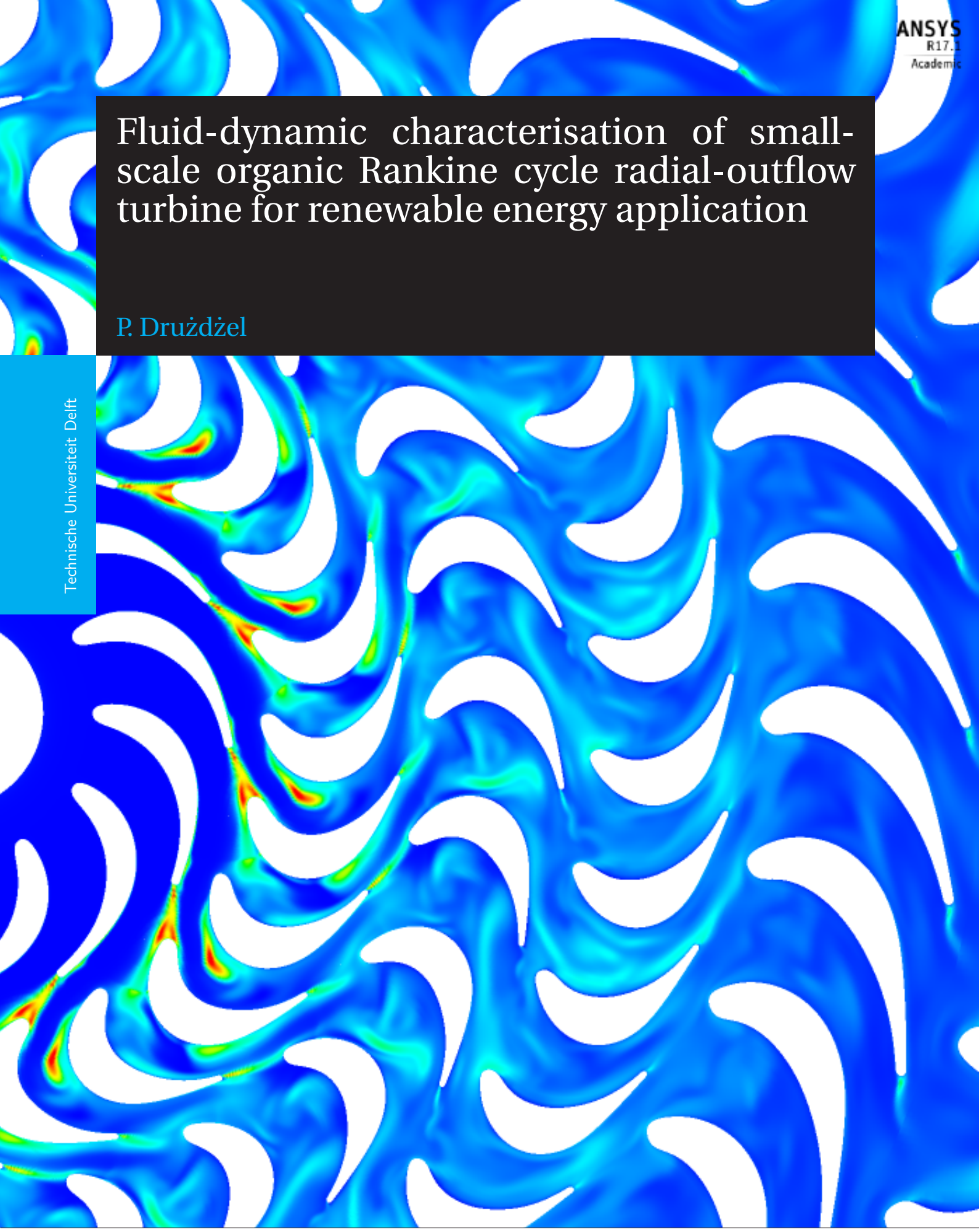

Fluid-dynamic characterisation of small-scale organic Rankine cycle radial-outflow turbine for renewable energy application

P. Drużdżel

Technische Universiteit Delft

TU Delft Delft University of Technology

Challenge the future

FLUID-DYNAMIC CHARACTERISATION OF SMALL-SCALE ORGANIC RANKINE CYCLE RADIAL-OUTFLOW TURBINE FOR RENEWABLE ENERGY APPLICATION

by

P. Drużdżel

in partial fulfilment of the requirements for the degree of

Master of Science
in Aerospace Engineering

at the Delft University of Technology,
to be defended publicly on Monday January 30, 2017 at 09:30 AM.

Supervisor:	Dr. ir. M. Pini	
Thesis committee:	Prof. Dr. ir. P. Colonna,	TU Delft
	Dr. ir. M. Pini,	TU Delft
	Dr. ir. A. Viré,	TU Delft
	Ir. A. Rubino	TU Delft

An electronic version of this thesis is available at http://repository.tudelft.nl/.

TU Delft Delft University of Technology

PREFACE

I would like to express my gratitude to supervisors: Matteo and Antonio for guiding me throughout this thesis. Many hours of meetings, conversations and presentations contributed to shaping the final version of this report. Your experience and insight were invaluable and helped me to discover fields of turbomachinery and CFD with passion.

I want to also thank my friends for always being there for me when I needed and a lot of good conversations. It was not only a large research project but also a long learning process.

Finally I would like to thank my parents for always supporting my ideas and without whom I would not be here. I always looked up to my father who obtained his Phd at the Faculty of Mechanical Engineering at this university and who has always been for me an inspiration during my career path. Thank you dad!

P. Drużdżel
Delft, January 2017

SUMMARY

Since the problem of global warming has been broadly considered as vital and due to constantly rising oil prices, further fossil fuels exploitation requires diametrical changes immediately. The demand for environmentally friendly improvements does not only entail searching for new resources but also utilizing those which are available and more importantly, renewable. Organic Rankine Cycle (ORC) is possibly the most flexible technology in terms of temperature level and capacity nowadays. It is often the only applicable means of conversion for external energy sources and is therefore a very active research area in the field. Project investigates performance of an unconventional, small-scale, three-stage radial outflow, ORC turbine as this component has proven to be critical in the system. Main content embraces steady and transient computational fluid dynamic simulations by means of Ansys CFX software and evaluation of loss mechanisms.

The main project objective is to evaluate the performance of the machine at its design conditions and fluid-dynamic characterisation of the flow. Geometrical data has been obtained from TU Delft in-house mean-line code zTurbo for preliminary fluid-dynamic design of turbomachinery. The main findings of this work involve performance evaluation of an innovative mini-turbine configuration and the applicability of available loss estimation models. Although there are guidelines on designing conventional, larger, axial power plants, still little is known about research in the field of small-scale, radial outflow machines working with molecularly complex fluids.

Overall total-to-static efficiency of the machine is 65.3 % for a 0.1 mm tip leakage gap and sealed stators. It is higher, and in close proximity to the one of 63.1 % obtained by mean-line prediction tool zTurbo. Thermodynamic processes undergone by the working fluid in mini-ORC ROT can be represented by velocity triangles at midspan with a 2.2% discrepancy in overall efficiency w.r.t. two-equation, steady RANS. Relatively uniform blade load, ability to apply tight clearance, tangential deflection in rotors due to Coriolis force and the relative motion w.r.t. the casing contribute to a decrease in 3D effects. This efficiency is expected to be slightly lower if tip leakage is imposed also on the stationary domains, possibly with even better match.

Total pressure loss coefficient for the first stator, for the steady-state case without tip leakage is of exactly the same value (23%) as the one for transient simulation with free-slip endwalls, accounting only for two-dimensional effects, averaged over the oscillation period. For the rotor, where the endwall boundary layer is more disturbed, steady state case predicts this loss by 3 points higher w.r.t. transient case, which gives 28%. Together with small secondary losses predicted in the stator, accounting for only 14% of the overall loss, 2D estimation/optimisation methods can be possibly used to predict the performance. Naturally growing passage area, allowing for smaller flaring angle, contributes to a decrease in span-wise velocity components and diminishes 3D effects.

Stage 1 proved to be more susceptible to tip leakage increase. Small aspect ratios, in the order of 0.5, in mini-ORC ramp up the impact of tip leakage vortex compared to larger blades. The poorest performance (total-to-total efficiency of 51.2%) has been noted for the third stage, which requires profile optimisation and stagger angle modification. Expectedly, increase in tip leakage gap in rotational domains, leads to rise in entropy, which is even slightly more perceivable in low-aspect ratio blades, such as Rotor 1.

Good match has been found between CFD and zTurbo in terms of overall loss estimation. Discrepancies for Rotor 1, Stator 3 and Rotor 3 are 0.1%, 0.1% and 0.2%, respectively. For Stator 1, Stator 2 and Rotor 2 these discrepancies are higher, of 3.3%, 7.7% and 3.0%, respectively. The main design problems are: profile losses and 2D design, including shock interaction shown in the results from the transient simulation. It is expected that this work will make a long-standing contribution to the body of knowledge on loss mechanisms in small-scale ORC machines and it will help to build a more sustainable and cleaner world.

CONTENTS

1

INTRODUCTION

1.1. MOTIVATION

In the last decades, global economies have been struggling with finding appropriate energy sources required not only for its survival but also for further technology development [1]. An interest towards decentralised power generation has recently arisen [2] but the broadly available renewable energy sources often feature comparatively low exploitable power capacity of the single site [3] [4]. Consequently, small to medium power range applications (between a few kW and a few MW) are expected to play an important role on the future energy market [2]. The conversion of renewable and waste thermal energy is in high demand [5]. Partly, due to the broadly known climate effects, but also because of the instability on the oil global market and is therefore the general area of interest in this work. The PESTLE concept i.e. Political Economic Social Technical Legal and Environmental aspect can be mentioned as the economic stability exerts a profound influence on research and technology development which later on is used by the society. In The Netherlands, the vast majority (~ 99%) of electricity is obtained by means of turbomachinery and there is still space for technological development in this segment [6]. From the technical standpoint an attractive system providing energy conversion from low temperature sources is ORC and studies on working fluids are recently of main interest [7], [8]. In terms of reliability and costs in low capacity ranges, ORC stands out w.r.t. steam Rankine cycles [9] [10].

The main aim of this work is performance evaluation of a mini radial-outflow turbine (ROT) in ORC technology by means of set of Computational Fluid Dynamic (CFD) simulations. Owing to this approach, all field quantities are simultaneously available and can be accessed directly without measurement errors [11]. The problematic element in the system is the turbine [2] [12] and more specifically, the first stator due to high load [13]. An expansion process with molecularly complex working fluid, MDM [2] can be seen in figure 1.1a. Pump efficiency is assumed to have a constant value of 75%. The influence of turbine efficiency on the extent to which the added energy is converted to net work output can be seen in figure 1.1b. It becomes apparent that a careful fluid-dynamic design of the expander is paramount, especially if manufactured on a large scale.

Due to limited computational resources, it is vital to choose suitable CFD approach and although Direct Numerical Simulation (DNS) [14] proves the most accurate [15], the challenge of computational time scales with the Reynolds Number (Re) raised to the power of three [11] and therefore becomes almost impossible in everyday engineering applications. For high Re, fluid viscosity is small and low dissipation rate results in very small turbulent eddies with respect to the largest in the domain, therefore computational effort to capture all the dynamics is enormous [16]. This problem has been tackled by modelling the effect of sub-grid turbulence scale on the larger, resolved scales in Large Eddy Simulation (LES) but it is still computationally heavy. An industry solution for less accurate engineering applications became modelling the entire turbulence spectrum - Reynolds Averaged Navier-Stokes (RANS) approach [17], which is a big assumption but has been confirmed by DNS [11]. Additionally, the challenge of loss mechanisms is open to exploration, especially due to the unconventionally small dimensions. Machine length is approximately 10 cm and the gaps between blades are in the order of 0.5-1 mm. Reflectivity makes imposing boundary conditions (BC) cumbersome. Trailing edge wakes contribute to non-uniform pressure distribution at the closely-positioned outlet where local pressure decrease in the vicinity of this boundary results in a back-flow. This phenomenon can be stopped

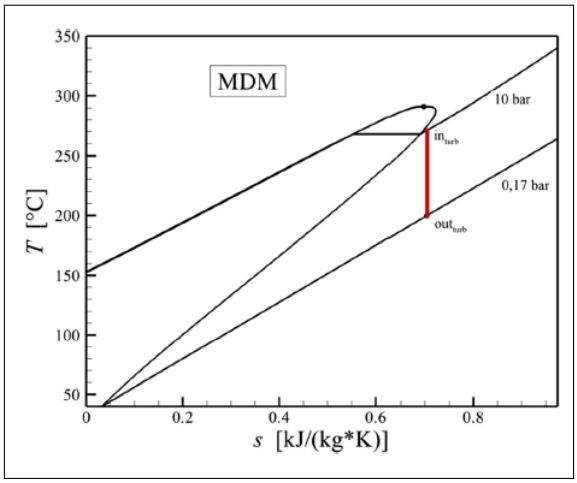

(a) T-S diagram for the expansion process with MDM as a working fluid [2]

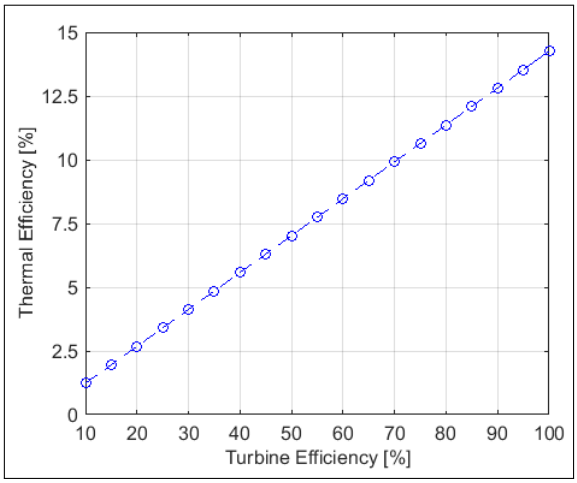

(b) Thermal efficiency dependence on turbine efficiency based on figure 1.1a

Figure 1.1: The impact of turbine efficiency on thermal efficiency

in CFX by imposing local walls which increase complexity and make simulation less physical. Another solution is specifying an opening type of BC which does not neglect inflow at that boundary, hence requires bigger amount of terms to model and larger computational demand. A common solution is prolonging the domain up to point where the fluctuation in static back-pressure is acceptable, e.g. with the relative error of 1-2 %. Since full machine simulation requires real distance between blade cascades, a short outlet mesh with circumferentially-averaged static back-pressure is preferred at this stage. Such assumptions, together with domain discretisation and flow physics definition enable fluid-dynamic characterisation and understanding their consequences is crucial. Entry simulations can provide insight whether e.g. simpler optimisation methods can be used to tackle the most important flow features or whether selected existing loss models are applicable in this type of machines. It can be the case that 3D effects are insignificant and a simpler, 2D analysis or optimisation routine can be used. Loss throughout this work will be associated with the entropy generation originating from: shocks, heat transfer due to temperature difference and viscous effects, especially at the boundary layer (BL) and due to fluid mixing. It is a convenient measure in turbomachinery because its value does not depend whether it refers to stationary or rotating frame of reference [18]. These loss mechanisms do not affect the performance independently and the interplay, such as the one between tip leakage and endwall loss, might be very strong [18].

To the author's knowledge, currently available loss models are based mainly on large power plants and specific treatment is still missing as the majority of ORC machines in the industry are axial or radial-inward [2]. The accuracy of available model becomes questionable due to different flow conditions and geometries considered in these methods [13]. The reason can be: smaller dimensions leading to stronger interference effects, different fluids and operating conditions and also the onset of supersonic flows [13]. Although simpler numerical solutions (e.g. 2-equation models), if converged, can provide a lot of valuable data towards understanding the flow behaviour, their accuracy is still too small to make a sufficient quantitative prediction of unsteady turbulent flow [18]. Strong non-linearity in the governing equations which causes discontinuities such as shock waves or small disturbances exert a profound influence on the flow. "However, progress in numerical methods and computer performance have solved many of these problems and today it is possible to, with at least some confidence, obtain a numerical solution of the flow field around a complete aircraft configuration including all major physical effects, such as e.g., shock waves, turbulent boundary layers and vortices." [16] Since for mass, momentum and energy exchange, responsible is the normal velocity component, internal aerodynamics features some differences with respect to external flows. According to e.g. aforementioned shock-wave, even in supersonic turbomachinery where the normal Mach number is below 1.0, the flow will adopt to the downstream static back-pressure due to existing region of influence [6]. With the challenge of still long computational overhead, strong interference effects, difficulty in splitting loss mechanisms and modelling assumptions a careful methodology is paramount for the performance assessment.

1.2. RESEARCH QUESTIONS

Main questions involve key project objectives and sub-questions help to answer those questions.

1.2.1. MAIN QUESTIONS

1. What is the total-to-static efficiency of mini-ORC ROT in design conditions?

   The most conservative and suitable efficiency definition for machines where outlet kinetic energy is not utilised is total-to-static efficiency. It is readily obtainable from CFD results and optimisation of this parameter implies improvement of total-to-total efficiency as well.

2. What is the fluid-dynamic pattern of a mini-ORC ROT turbine?

   Some flow details can be difficult to comprehend based only on performance parameters. A great advantage of CFD is fluid-dynamic pattern and data immediately available at any point in the domain. Flow features, such as span-wise velocity components are impossible to predict with a mean-line design codes. Interference effects such as shock impingement on blade BL can be easily seen and conclusions can be drawn.

3. What are the associated losses?

   Although contour maps provide a lot of qualitative and quantitative data, numerical assessment is paramount to compare the significance of certain flow features. Various performance coefficients are hence evaluated and compared. With this knowledge, appropriate design and optimisation methodology can be chosen to tackle the most important factors such as e.g. capturing only 2D effects at lower computational expense.

4. What are the main design problems, where are they located and why they occur?

   Based on the aforementioned advantages, it is possible to evaluate design challenges, their location and conclude their origins. Knowing the source of irreversibility can help to make design decisions such as where to modify the blade profile, what are the alternatives and whether they are feasible.

1.2.2. SUB-QUESTIONS

1. What is currently known about ORC technology?

   Research on ORC technology historical development is vital to highlight relevant achievements and what knowledge can contribute to research questions. As proved in the literature review, the topic has been very lively over the last years, however, the recent progress in the field of CFD allows investigate internal flows extent that was not available in the past. Selecting appropriate CFD approach is necessary and can help to allocate e.g. time and computational/financial resources needed for the project. With currently available various turbulence models, selection has an impact on the accuracy and stability of the solution.

2. What criteria are relevant for accessing the efficiency of small-scale ORC radial outflow turbines?

   With the available various performance parameters, it is vital to select only the meaningful ones and account for the difficulty of obtaining them from e.g. cascade test data or CFD results.

3. What methods exist to find these flow parameters at their exact location and evaluate those criteria?

   It can be the case that suitable loss estimation methods are available or quite the opposite, they can pertain to different machine configurations. If the latter is the case, another question arises whether these methods apply to new configurations. Some methods proposed in the past turn out to be irrelevant for fast CFD estimation or not accurate enough.

4. To what extent these results are reliable?

   Reliability of RANS has to be taken into account and the modelling assumptions have been carved in mind during post-processing. These assumptions and any deviations from the real flow behaviour can exert an impact on the final results and conclusions. Some of them, e.g. mixing plane assumptions at the interface between the domains are unavoidable with the available resources and have to be accounted for during assessment.

2

LITERATURE REVIEW

2.1. RESEARCH DONE ON ORC

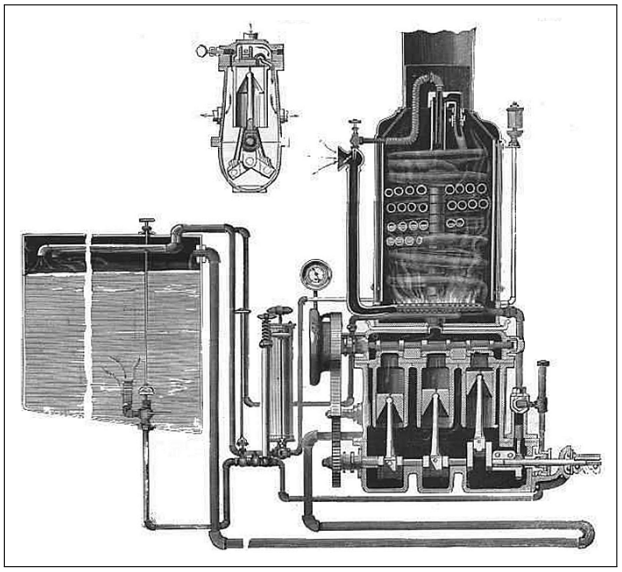

Figure 2.1: One of the earliest ORC engines, designed by Frank W. Ofeldt, 1897. The long, u-shaped tube at the bottom is the condenser. [12] [19]

In the past, attempts have been done towards designing larger ORC turbines such as the concept proposed by T. Howard in 1826 [20] where utilising ether as a working fluid has been patented or in 1898, when F.W Ofeldt patented naphthafed ORC engine utilising reciprocating expander (see fig. 2.1). In 1888, A. Yarrow proposed an ORC engine for launches [21] and in 1891, A. Nobel used one to propel almost 9 m long boat, Mignon [22]. An early application of ORC technology in the solar energy has been done by F. Shuman in 1907 [23] where a solar panel of 110 m^2 has been used to boil ether to ~ 120 $^{\circ}C$ and propel 2.6 kW engine. An immense contribution to contemporary ORC technology had Professor D'Amelio (1893-1967) and his work received large attention, specially in the 1930s and 1940s [12], [24], [25]. Professor Bronicki's study on small solar power plants [26] was inspired by Professor D'Amelio with whom he met during his MSc studies [12]. In terms of mini-ORC particularly, studies were performed in the 1960s on perfluorocarbons [27] and resulted in a few experimental systems [12]. "In these systems, static nonfocusing collectors were adopted, thus achieving comparatively low maximum cycle temperature (around ~ 100 $^{\circ}C$), and solar-to-electric efficiency (typically < 5%)" [12]. Also in this period, researchers under Professor Bronicki manufactured and tested a 2-10 kW small-scale solar ORC unit working with monochlorobenzen [12] and 12 years of successful run without repairs has been noted for some of them [28]. Between 1961 and 1988 thousands of 0.2-6 kW units of this type ORC turbogenerators were installed[12]. Further studies in Italy, conducted by Professor G. Angelino together with Professor M. Gaia and Professor E. Macchi [9] were very prolific and resulted in a 35 kW machine utilising perfluorocarbon as a working fluid and providing 19 % net electric conversion efficiency [29]. A 12 kW solar unit has been built in Tunisia in 1983, employing tetrachloroethylene with recorded net conversion efficiency of 11% [30]. An interesting study was conducted by Professor Jaakko Larjola in Finland in 1998 [31]. In his concept turbine, generator and pump were mounted at the same shaft. It was successfully used as a 25 kW battery charger for a research submersible. In 2013, a design oriented work of M. Pini [2], where a multi-stage machine of approximately 1 MW is considered, attention has been drawn to radial configuration. In 2014, E. Casati [13] published his work on centrifugal mini-ORC turbines. A lot of prolific work on ORC has been attenuated due to low oil prices in the 1980s but these systems receive large attention nowadays [2]. An example are small-scale units recovering waste heat in the automotive sector which is now very lively [32].

2.2. ORC TECHNOLOGY

The main reason for using ORC with low temperature power range is high turbine/thermodynamic cycle efficiency allowing to recover low-grade heat that otherwise would be wasted.

2.2.1. ADVANCEMENTS

1. Ability to replace water with carefully chosen organic compound as a working fluid [12]:
   - 1.1. Thermodynamic cycle can be optimised for given fluid properties which yields the possibility of utilising sources of wide temperature range, including renewables (see: Fig. 2.2a).
   - 1.2. Saturation curve and critical point can be chosen.
   - 1.3. Temperature profile can be matched during heating and cooling processes. Figure 2.2a shows significantly shorter phase change for the organic compound with the constant pinch point.
   - 1.4. Supercritical configuration can be viable even for low temperature sources.
   - 1.5. Possibility to attain a dry expansion process eliminating corrosion problems (see fig. 1.1a).
   - 1.6. No need for lubricant as some organic fluids fully ensure this property.
   - 1.7. Lower freezing temperature to avoid volume increase due to freezing.
   - 1.8. Disc friction can be reduced due to low pressure in the condenser by using high boiling point vapor [33].
   - 1.9. Environmentally friendly, closed loop systems [34].
2. Smaller enthalpy drop for molecularly complex fluids [12]:
   - 2.1. Lower rotational speed allowing smaller or no gear reduction.
   - 2.2. Low mechanical stress at the turbine due to low peripheral speed.
   - 2.3. Larger volumetric flow for given power range [12].
   - 2.4. Fewer stages needed.
   - 2.5. Long life of the plant (> 20 years [35]).
   - 2.6. Relatively smaller temperature changes w.r.t. steam turbines allow using cheaper materials.
   - 2.7. Lower pressure within the ORC cycle result in safer and cheaper evaporator, hence lower operational costs.

2.2.2. CHALLENGES

1. Fewer stages result in higher velocities, especially at the first stator [12]. For a given solidity smaller flow deflection reduces the eulerian work [6] and attempts to reduce the load can increase number of blades lading to larger axial forces and hence, bearings.
2. Low sound speed for organic fluids enhances shock losses [12] which can lead to BL separation at the foot of the shock wave [36].
3. Possibly poor efficiency due to very low mass flow, relatively big expansion ratio along with large specific work over the expansion ratio [12].
4. For lower condensation pressure and temperature, large outlet volumetric flow can necessitate bigger condenser and if used, also regenerator [12] aggravating compactness.
5. Still relatively high temperature and direct contact of the organic compound with the blades, conversion efficiency might decrease [12] due to thermal decomposition of the currently available working fluids (Siloxanes, Hydrocarbons and Perfluorocarbons). The highest thermal stability has been recorded for a pentafluorobenzene and hexafluorobenzene mixture [37].

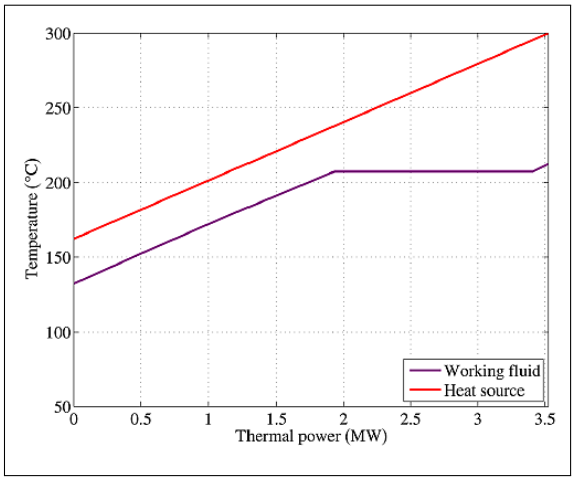

(a) $\dot{Q} - T$ diagram for evaporator in ORC system. Energy source at 300 °C [12]

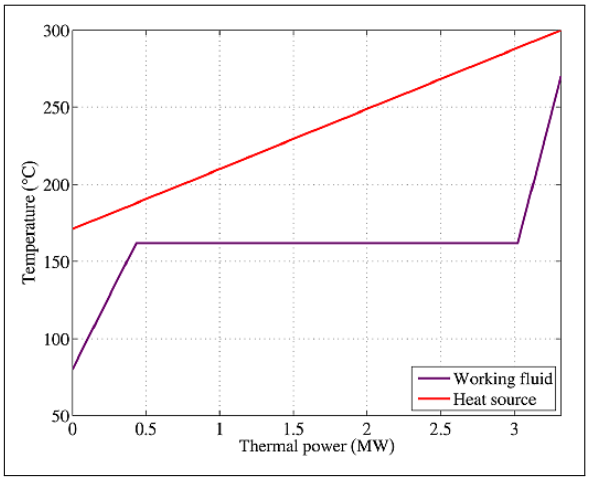

(b) $\dot{Q} - T$ diagram for boiler in a steam power plant. Energy source at 300 °C [12]

Figure 2.2: Comparison between ORC system and simple steam power plant. Notably higher boiling point for organic fluid.

2.2.3. REQUIREMENTS FOR WORKING FLUIDS

1. High thermal stability.
2. Low freezing point (e.g. in the automotive industry, the engine should be able to idle at -40 °C [12]).
3. Good heat transfer properties [12].
4. Low environmental impact including Ozone Depletion Potential (ODP) and the Global Warming Potential (GWP).
5. Safety (non-toxicity, non-flammability, non-corrosivity).
6. Good lubrication characteristics.
7. Availability and acceptable costs.
8. For small to medium power ranges and relatively large temperatures: preferably more complex molecules such as siloxanes or toluene [12].

2.2.4. APPLICATION

Waste heat delivered to the system through heat exchanger can originate from various sources, making the range of applications very broad. Apart from utilisation in geothermal resvoirs, solid biomass combustion, industrial waste heat and concentrated solar radiation, ORC can recover flue gas from other engines (turbine, gas or diesel). An outlook to the future is presented.

HEAT RECOVERY FROM AUTOMOTIVE ENGINES

Unlike in aerospace industry, manufacturing occurs on a much larger scale and requires more standardisation, which is feasible but large units, above 2-3 MW are usually very customised [12]. Recently, of interest is add-on recovery from long-haul truck engines [38] where, unlike in cars [39] extractable power can be enough to avoid drawbacks of very small expanders [12]. By proper choice of working fluid, the size of a small power turbine blades can be increased to almost any desirable dimensions [33]. Several examples of ORC turbogenerators recovering heat from flue gas in gas and diesel engines already exist and the number is increasing [12]. Combined cycle power trains feature integrated optimised gas and steam turbine systems where relatively big part of heat dissipated by the cooling system can be still extracted [12]. It is possible to utilise flue gases directly as a heat source or in landfill sites [40], but usually the gas is used in an internal combustion engine, while ORC can be added as a heat recovery system for the engine exhaust [12], [41]. The flue gas can originate from many sources at a time and can be combined into one, larger ORC unit [12]. There however, are still few units working as bottoming cycles of gas turbines [42] but this number is rising [12], [43]. Importantly, if this sector proves successful, it opens doors to domestic applications [12].

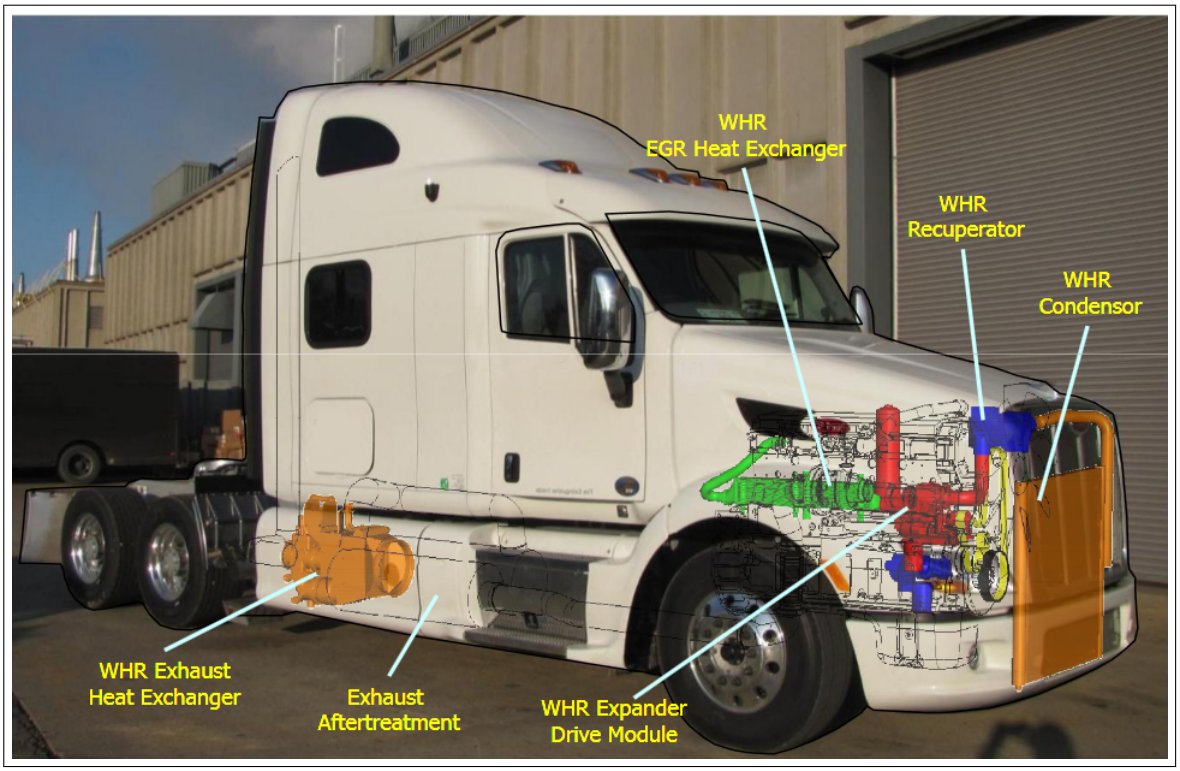

Figure 2.3: An example of heat recovery system in a heavy-duty truck [44]

DOMESTIC COMBINED HEAT AND POWER (CHP)

There is a large market of potential recepients [45], and it can arise in developing countries ("several million units per year, in Europe only" [12]). There are examples of very small, 1kW machines [46] and small, 10-30 kW [47] using usually scroll expanders due to low temperatures and small volumetric expansion ratios [12]. The electric effiiency is low, in the order of 5 – 10% [12].

CONCENTRATED SOLAR POWER (CSP)

Most of the current research focuses on "low-to-medium" temperature solar ORC [12]. Local thermal storage inegration with cogenerating heat and cooling is possible and can be competitive with photo-voltaic panels but the complexity might increase [12]. Small-scale solar/biomass ORC were predicted since the early research in this field [26] and development in this field is still very active [12], [48], [49].

OCEAN THERMAL ENERGY CONVERSION (OTEC)

Temperature difference ($20°C$) between surface and deep-warter (600-1000m) can be sufficient for ORC application and it has been under consideration for years [50]. No commercial application exists because of too low power density [12]. With the progress in off-shore engineering problems with deep-water piping can be resolved and amonia-water solution can be applied provided that heat exchanger are large enough [12]. An interesting study on this subject can be found in [51].

2.3. ALTERNATIVES OF THE ORC TECHNOLOGY

Several solutions already allow recovering heat from lower temperature resources. They mainly find their application in larger power units and are usually not suitable for small-scale applications.

2.3.1. STIRLING ENGINES

Typical Stirling engines are efficient for high temperature source (700-1100 °C) [12]. As a result their low power-to-weight ratio makes them more suitable for large solar power plants, biomass and biogas combustion and domestic microgeneration [12] [52]. Also, fast and effective variations of power are difficult to obtain. Some of the challenges are: complicated kinematic mechanism and leak-prone fluids (air, nitrogen, helium

and hydrogen) which necessitate high-quality sealing system. In terms of price, they are not yet competitive with other, well established means. The main advantages involve high net conversion efficiency, relatively low costs and large power density which make this system very attractive.

2.3.2. CLOSED BRAYTON CYCLE

The second alternative is a Closed Brayton Cycle (CBC) which usually employs simple-molecules working fluid such as CO_2. This implies a challenge for low power range expanders which might result in faster rotational speed and the necessity to use a gearbox. Aplicable in large-scale space exploration and a promising technology for high temperature solar power plants [53] and power generation due to nuclear fusion [54]. "The main advantage of the supercritical CO_2 cycle is comparable efficiency with the helium Brayton cycle at significantly lower temperature (550°C vs. 850°C), but with the disadvantage of higher pressure (20 MPa vs. 8 MPa)" [55].

2.3.3. EXTERNALLY FIRED GAS TURBINE

Successfully applied in the past fifty years, Externally Fired Gas Turbine (EFGT) can deal with a wide range of fuels, even solid, without cleaning systems or fuel compression and injection equipments [56] and is mainly suitable for concentrated solar power plants and biomass combustion. Since turbine performance depends strongly on turbine inlet temperature, it requires high temperature heat exchanger (HTHE) technology [56]. Recent prototypes indicated limited efficiency and poor reliability [12]. Micro EFGT are often used in combination with combined heat and power (CHP) distributed generation units and are suitable for small industries where the energy requirement are relatively low [56].

2.3.4. KALINA CYCLE

Since working fluid is a mixture of usually water and ammonia, unlike in Rankine cycle, heat addition and rejection occur at varying temperature also in the phase change. Due to higher average heat addition temperature and lower heat rejection temperature, the thermal efficiency of the Kalina cycle can be larger compared to Rankine cycle. High concentration of ammonia yields low condensation temperature thereby making the condenser rather large. Thanks to the possibility of varying mixture components and their concentration, it is commonly applied in geothermal reservoirs and waste heat recovery. The possibility of using recuperator and separator are another advantages which, however, complicate the system and make it even less applicable in the small-scale sector.

2.4. RADIAL OUTFLOW CONFIGURATION

To the author's knowledge, the vast majority of publications pertain to large power plants and specific treatment is still missing as the majority of ORC machines in the industry are axial or radial-inward [2]. A lot of knowledge developed mainly in the last several decades in the field of steam turbines extends the body of knowledge to ORC technology [33] [57] [58] [59] [60]. Design is complicated due to lack of open literature on the subject of experimental data from ogranic fluid flows [61] [62] [13]. An example of ROT machine can be seen in the figure 2.4. Simplified design procedures derived from axial turbines can be found in the work of E. Casati [13]. Casati notes that the assumptions used can be only partly realised in radial turbines due to stream-wise variation of the peripheral speed and a new design rules have been established [13]. ROT designed based on the guidelines for axial machines may exhibit different velocity triangles per stage and a peculiar channel shape which converges for the initial stages and diverges for the further stages can be seen in the figure 2.5a and also in [2] and [63]. For mini-ORC systems, this converging-diverging shape might result in insufficient blade height at the inlet whereas the full admission in the first stage is desirable to achieve high efficiency. A change in meridional channel results in additional span-wise velocity component contributing to secondary losses. In 1949 Ljungstrom [64] proposed a counter rotating centrifugal machine working with steam which featured number of advantages over radial-inward and axial turbines. The potential of these machines for ORC technology have been predicted in [57]

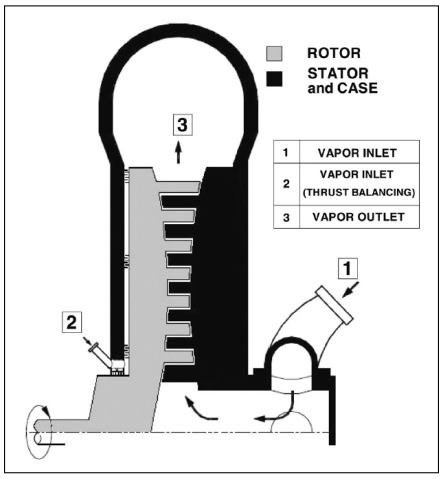

Figure 2.4: An example of ROT [13]

and [65]. The downside of counter rotating configuration is mechanical solution for the shafts and from the aerodynamic standpoint, a non-uniform flow [6]. Although large volumetric flow in [64] led to problems with single-casing arrangement, low specific work in ORC allows for avoiding counter-rotating cascades and applying simpler stator-rotor configuration [2]. ORC turbines feature lower power output (up to a few MW) w.r.t. steam power units and the outlet volumetric flow is rather small allowing for a single-casing configuration [2].

In ROT, relative velocity vector is perpendicular to the angular velocity vector. The Coriolis force acts on the blade surface and deflects the flow tangentially. This has a negative contribution to the rotor blade deviation which rises the work exchange [66]. Even small change in the flow angle yields a strong effect because the flow is highly tangential [66]. ORC features small temperature changes, in the order of 50 $^{\circ}C$ [2]. Resulting smaller thermal gradients allow using cheaper materials compared to steam machines and the ability to machine the blades on the single disk [2].

Unlike in axial machines, blade chords affect stage diameters along the machine and the potential of centrifugal force acts against work extraction [2] which depends on the change in peripheral speed [13]. As a result, volumetric flow rate changes and the passage area as well. This passage area is also affected e.g. by the presence of blade sections and boundary layers which are accounted for by means of a certain correction factor. According to [13] flaring angle of the i-th row can be expressed as:

$$\delta^i \approx \frac{H_{out}}{H_{in}}\Big|^i \propto \underbrace{\frac{\rho_{out}^{i-1}}{\rho_{out}^{i}}}_{\text{A}} \cdot \underbrace{\frac{V_{out}^{i-1}}{V_{out}^{i}}}_{\text{B}} \cdot \underbrace{\frac{\cos(BDA^{i-1})}{\cos(BDA^{i})}}_{\text{C}} \cdot \underbrace{\left(\frac{D_{in}}{D_{in}+b}\right)^{i}}_{\text{D}} \tag{2.1}$$

where: H is the blade height in mm, ρ is the density in $\frac{kg}{m^3}$, V is the mean-flow velocity in m/s, BDA is the blade geometric discharge angle in degrees, D is the cascade diameter in mm and b is the chord in mm. In ROT, term B is lower than one due to the rise in peripheral speed along the machine. From the conservation of rothalpy in rotating cascade it also implies rise in the rotor outlet velocity with respect to axial machine having the same stator outlet velocity, inlet rothalpy and static outlet enthalpy. Thus term B has a negative influence on the flaring angle in the equation 2.1. Due to assumption of the same BDA [13] term C is equal to one and the meridional channel shape is mainly a function of terms A and D.

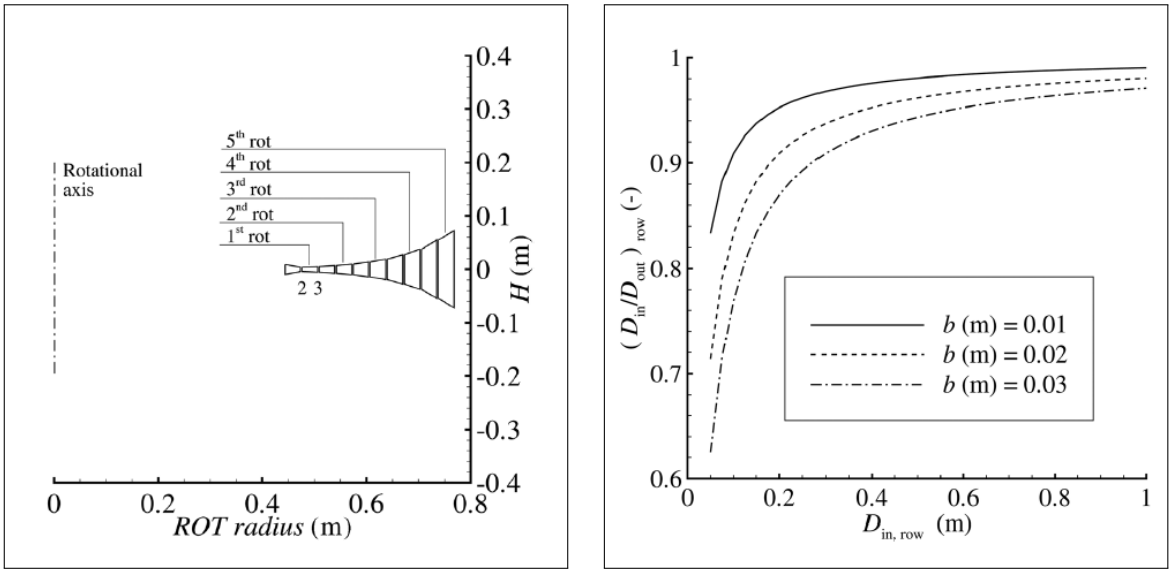

(a) Meridional section of ROT with the characteristic convergent channel shape for the first stages [13]

(b) Diameter ratio for a centrifugal row D_{in}/D_{out} as a function of the row diameter D_{in} and of the radial chord b [13].

Figure 2.5: Centrifugal turbine configuration for mini ORC power systems [13]

Plotting term D of the equation 2.1 w.r.t. row inlet diameter (see figure 2.5b) shows that as the diameter rises, this term becomes closer to one, hence its influence on the flaring angle vanishes. It has been concluded

that: "centrifugal stages characterized by small values of the ratio b/Din tend to behave as axial stages, with the chord size having little influence in determining the meridional channel shape, which is rather determined by the expansion process, i.e., by term A in equation 2.1" [13]. In small-scale machines, when the ratio b/D_{in} is relatively large, term D is smaller than one leading to convergent meridional channel [13]. It has been shown that this methodology is not suitable for mini-ORC and a new design approach is necessary.

New design approach proposed in [13] allows e.g. for including diameter and shaft speed of revolution in optimisation routine which rules out the estimation based on statistical data [67], [68]. Due to small volumetric flow in mini-ORC turbines blade heights can be low and lower bound is based on the mechanical resistance and limits from the manufacturing and similarly for trailing edge thickness and tip clearance [57], [69]. The optimisation of radial gap between cascades is not possible with the mean-line prediction methods, hence needs to be fixed [13] and it has a strong influence on performance of the machine [70]. For ROT, this impact may be expected even larger [13] because an increase in the passage area in the radial direction due to gap leads to flow diffusion. An advantage of keeping this gap longer is more uniform flow at the inlet of each stage, hence an optimal vane-rotor match [2]. From the experience on axial machines the suggested distance is 1-2 tenths of vane chord [70]. Compensating this difference with the smaller channel span in the gap region could lead to complex geometry [13] and possibly, additional manufacturing issues.

According to research on small gas turbines conducted in 1969 by C. Rodgers [71] it has been shown that it is difficult to maintain clearances less than about 0.4 mm. However, in ROT, due to the possibility of applying almost hermetic seals on the shaft [57] tip leakage on the stationary domains can be neglected [13]. This is a large asset when using CFD prediction tools as number of leakage gaps in the model, where variables such as velocity or temperature can locally go out of bounds leading to convergence problems and the necessity of using very small time-step or other measures (see chapter 3), even in steady RANS approach.

The choice of blade types depends on the velocity regime and for mini-ORC, which are often exposed to off-design conditions it becomes a challenge. According to [13] converging blade rows can handle flow up to approximately Ma = 1.4 due to post-expansion [72]. For higher Mach numbers dissipative shock patterns can affect the performance. This can be specifically adverse in off-design conditions [72] [73] and theoretically can be resolved by convergent-divergent configuration. These however, are usually used when the size is a strong constraint [59] at the expense of performance. The advantage of ROT is the ability to relatively easily increase the number of stages which compared to highly supersonic passages are characterised by high efficiency, smaller manufacturing costs and "reasonable size" [13].

In ROT, just like in any turbine configuration as opposed to compressors, boundary layer is exposed to negative pressure gradients [12]. Separation is alleviated and allows for bigger curvatures to achieve larger specific work. Also, larger angles of attack and pressure ratios are possible leading to further reduction of number of stages. Thus less complex profile design process is possible in e.g. shape optimisation or discretisation.

ROT, compared to radial-inward or axial machine with the same power output and similar application [76] features much lower shaft rotational speed. In [13], author quotes 15400 rpm and even 12400 rpm for three-stage and five-stage configurations respectively. This is a result of reduced stage load due to using larger amount of stages. Also, as seen in the figure 2.6a, channel height is increasing quite smoothly. The quoted flaring angle is maximum at the third stage and is of 9 degrees. Small values of this parameter can reduce the aforementioned three dimensional effects. Interestingly, as also seen in the figure 2.6a, obtained optimal blade chords are the largest for the last stage as a result of mass conservation [13]. First stages, to avoid converging channel as seen in the figure 2.5a, result in short radial chords. For a given pitch, shorter blade chords result in higher aerodynamic loading. In axial turbines, peripheral speed can be assumed constant and the aerodynamic load is normally proportional to specific work converted by the stage but it is not the case for ROT [13]. Because peripheral speed rises along the turbine, a reduction in aerodynamic load does not directly imply smaller specific work. Figure 2.6b shows higher profile losses for initial stages. Obtained load coefficient decreases along the machine whereas the specific work of the stages increases [13] leading to smaller specific total enthalpy drops and larger aerodynamic loadings and flow deflections. It has been noted that the overall efficiency of the machine is weakly affected by the comparatively large stage losses [13]. As seen in the figure 2.6b, secondary losses are higher for initial stages, possibly due to stronger tip leakage interaction with the secondary flows due to smaller aspect ratios w.r.t. further cascades. For these last stages, the ratio

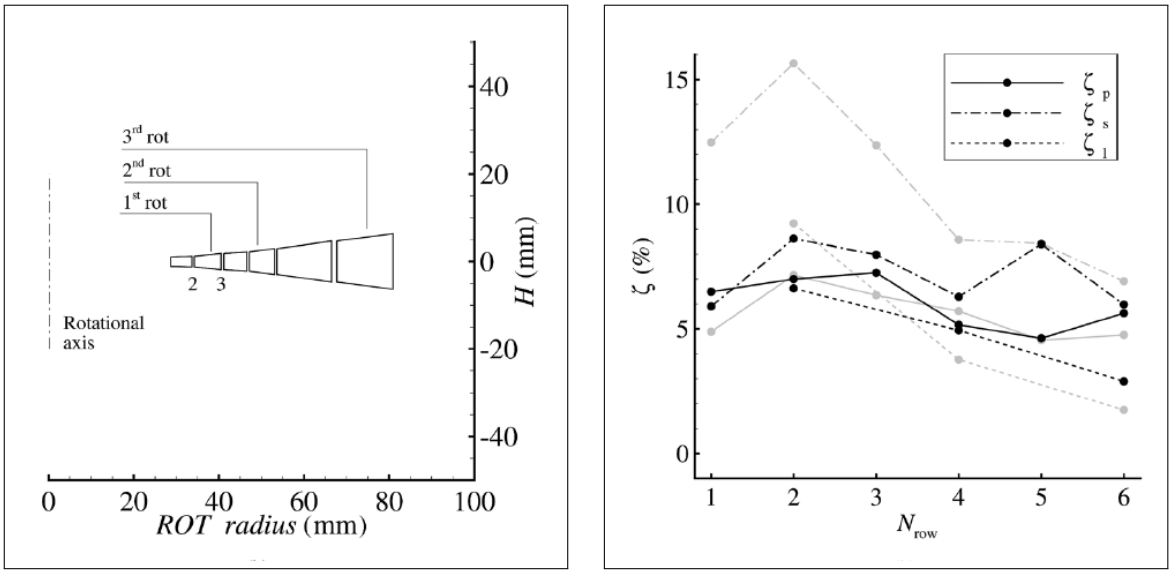

(a) Meridional section with gradually increasing blade height row by row and notably growing optimal radial chords [13]

(b) Row evolution of the kinetic energy loss coefficients. Black lines - Traupel loss estimation method [74], gray lines - Craig and Cox [75] [13].

Figure 2.6: Three-stage ROT configuration for mini ORC power systems [13]

between the blade height and the leakage gap is larger and hence tip leakage losses are smaller. Although volumetric expanders are often applied in low temperature and low power range systems (1-100 kW) [12], the limit of small volumetric expansion ratio rules them out from high temperature applications. ROT, which are not suitable for the low molecular weight fluids (water) due to significant number of stages needed, become more profitable for the molecularly complex fluids such as Hexamethyldisiloxane (MM) [77]. The possibility to choose working fluid and smaller enthalpy drop for molecularly complex compounds make ROT feasible even though it has been temporarily phased out in the industry mainly by axial machines [77]. The possibility to accommodate several stages on the same disk significantly minimises vibrations, disk friction losses and static and dynamic loads at the bearings. It also reduced seal requirements and thermal losses [78]. The distance between the centre of gravity of the turbine and those bearings is smaller [77]. Since the radial distance from the rotation axis is constant for each blade height, the peripheral speed remains the same and no radial equilibrium establishes span-wisely [79]. The same velocity triangles maintain at both hubs and tips allowing for simpler, prismatic blades and hence lower manufacturing costs. Importantly, the velocity triangles can be chosen as an optimum for a certain degree of reaction and work coefficient at mid-span location [2]. Apart from certain secondary endwall effects, these conditions are valid along the entire midspan [2].

The power output of a given unit can be adjusted by changing the turbine blade heights appropriately without any significant impact on the turbine housing [78]. Along with the radius, cross section rises proportionally which helps to accommodate the volumetric flow better than axial machines where typically flaring angle would have to increase. It has instead a low specific work per stage due to change in peripheral velocity while expanding the vapor [77]. The outward direction of the fluid decreases the three-dimensional effects and hence results in smaller turbulence levels which further decreases the entropy generation. Higher blades at the inlet can diminish the tip leakage, its interplay with the endwall loss and eliminate the necessity of partial admission. Also, lower blades at the outlet lead to mechanical advantages [80] [81] [82]. The inlet pressure can be higher whereas the pressure at the condenser can remain the same hence the thermodynamic efficiency can raise [77]. A cumbersome issue is choosing a suitable loss prediction method because classical approaches are questionable [13] due to their application range [83]. The applicability of conventional methods, e.g. Traupel [74] or Craig and Cox [75] can decrease even further with the rise of compressibility effects and with a decrease in flow passage area [13]. According to [66], methods derived for axial machines tend to underestimate the performance.

2.5. LOSS MECHANISMS

When considering turbomachinery, the efficiency of the system is usually the most critical factor [18]. The way of defining it strongly depends on whether the exit kinetic energy is utilised or wasted. When it contributes to the thrust of a jet engine or when it is used in subsequent stage of a multi-stage machine, it is considered as used and defining total-to-total efficiency is usually more useful [72]. In case of mini-ORC ROT machine at hand, kinetic energy is not utilised, therefore total-to-static efficiency is more relevant to estimate what amount of this kinetic contribution is wasted. It is not possible to entirely eliminate this kinetic energy component due to the need of having a mass-flow through the exit. Optimising total-to-static efficiency leads to optimisation of total-to-total one but not vice-versa [6]. Loss will be treated as "any flow feature that reduced the efficiency of the turbomachine but this does not include factors that affect cycle efficiency" [18].

2.5.1. RESEARCH IN THE PAST

Turbomachinery-related research was very lively in the 1940s when A.R. Howell (1945) [84] published his work on fluid dynamics and design of axial compressors. There have also been examples of analytical methods for loss estimation such as Carter (1948) [85], but this approach was strongly idealised [18]. In the 60s and 70s earlier developed methods were still popular and sometimes changed for the need of manufacturers. The extrapolation lead to the possibility of predicting new designs and their accuracy was of approximately ±2%. According to J. D. Denton (1992) [18] these modifications of former loss estimation methods resulted in erroneous trend of relying on them without critical validation. Invention of hot wire significantly contributed to the understanding of the flow physics and also new numerical methods such as the famous $k-\epsilon$ model by W. P. Jones and B. E. Launder (1972) [86]. The geometric influence on the inviscid flow can be determined numerically but the specific effect on the loss cannot be quantified exactly [18]. Although the general understanding of the flow improved over time, "most practical performance prediction methods continue to be based on correlations, [which] tell us nothing about new design features that were not available at the time the correlation was developed" [18]. It is important to be aware of these shortcomings.

In 1951, Ainley and Mathieson [87] published work on design methods for axial machines. They were based mostly on experimental results for cascade tests and from the machines applied in the industry. Turbine blades had a "circular-arc" shape and were thought of as "conventional" type and most of the data featured low exit Mach number [88]. Total pressure loss coefficient could be predicted within ±15% and overall efficiency of the stage within ±2%. Although the same behaviour can be expected for similar machines, it might not hold for mini-ORC ROT. Losses were divided into profile, endwall and tip leakage contribution but the model is rather complex for fast estimation. This approach is not convenient for fast CFD estimation due to the necessity of obtaining various incidence angle configurations in profile loss computation.

In 1970, J. Dunham and P. M. Came improved the correlations of Ainley and Matthieson [89]. Importantly, approach by Ainley and Mathieson [87] proved to be inapplicable to small and unconventional machines [88]. Modifications involved mainly secondary and tip leakage losses and also Reynolds number effect and subsonic outlet Mach number.

In 1980, S.C Kacker and U. Okapuu [90] presented a mean line prediction for axial flow turbine efficiency. They introduced a lot of modifications to method presented by Dunham and Came including testing 33 turbines of various sizes that were typical that time. New correlations for profile, secondary and tip leakage have been introduced but also a new approach featuring trailing edge influence as a separate source of loss rather than a fraction of profile and secondary loss presented by [87] and [89]. Profile loss features similar approach to the previous models with the small modification allowing to include negative inflow angles.

Model presented by H.R.M. Craig and H.J.A. Cox in 1970 [75] accounts for gas and steam turbines, which can have a negative impact on prediction accuracy if only gas turbine is considered w.r.t. models tailored for this type of machines [88]. According to the author, prediction resides within "accuracy of ±1.25% percentage point" [88]. Profile and secondary loss correlations were based on the linear cascade test data and tip leakage was obtained from turbine cascade tests. According to Craig, different working fluid, Re, size, Ma and surface roughness can be all accounted for [88] [75] but discrepancies due to "differences between uniform and disturbed flow, linear to annular flow and stationary to relative movement between blade and wall are more difficult to account for" [88] [75].

In 1969, M. K. Mukhatarov and V.I Krichakin [91] proposed procedure of estimating losses in axial turbines for linear cascades with small cone angles and subsonic exit Ma. Inlet and outlet angle flows should be within 5-100 and 15-50 for inlet and outlet respectively [91]. In the same year, an interesting work on optimal pitch-to-chord ratio in turbine cascades [92] has been presented and it is still used in the industry, such as Siemens in-house tool CTC [88].

In 1990, S.H Moustapha, S.C Kacker and B. Tremblay [93] introduced another modification. The general approach for that time remained, that is, profile loss was measured at midspan and treated as uniform in the span-wise direction. Secondary loss was obtained from subtracting profile loss neglecting tip leakage from total measured loss and the correlation from 1990 involved corrections for off-design conditions [88]. In 1997, this model was further continued by Benner [94] and later on also in 2005 by J. Zuh and A. Sjolander [95].

Physically unsatisfactory assumption of uniform loss generated in the airfoil surface BL across the span in conventional scheme resulted in erroneous values of the secondary component at high positive incidence [96]. In 1987, O. P. Sharma and T. L. Butler [97] proposed a scheme including correlation for the span-wise penetration depth of the passage vortex separation line at the trailing edge but is was based on the small database [98]. This scheme accounted for flow turning but neglected the effect of blade solidity. In 2006, M.W. Benner [98] proposed a new loss breakdown scheme involving not only flow turning but also the effect of pitch-to-chord ratio. The author puts an emphasize on the off-design conditions, especially in case of change in the incidence angle, which has "perhaps the most significant effect" [98]. From the viewpoint of mini-ORC turbines, which are likely to work in off-design conditions [13], this is particularly important. In 2016, J. D. Coull referred to the work of Benner et al. from 2006 [99] pointing out that the data was relatively "sparse" and "did not exhibit clear trends" [100] and also, some measurement inconsistencies. In the work of Coull and Hodson from 2013 [83] it has been noted that available that time models vary significantly in their estimations and proved sensitive to different design parameters.

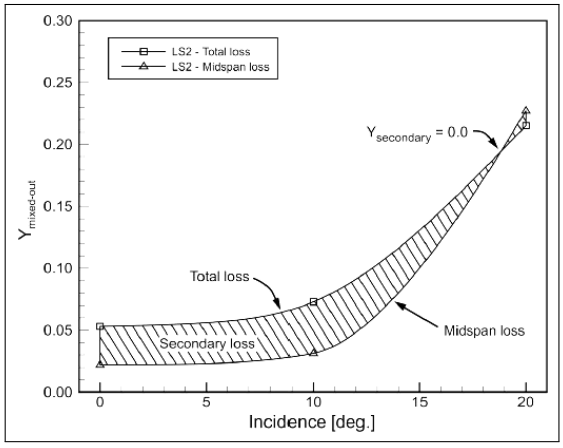

(a) Negative endwall loss in old scheme [98]

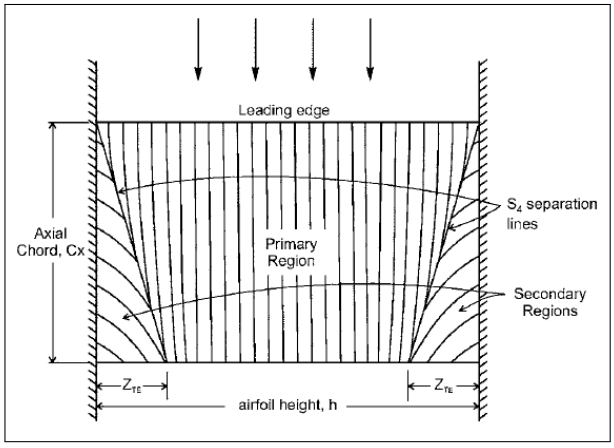

(b) Suction surface for the new loss breakdown scheme [98]

Figure 2.7: Loss scheme proposed in the work of Benner [98]

Approach proposed by Benner is based on tests for large-scale, low-speed, linear turbine cascades which, as treated earlier, exhibit discrepancies w.r.t. mini-ORC ROT. To the author's knowledge there is no correlation accounting for fast loss estimation for small-scale, ORC ROT and taking into account soaring interest in this technology [12] it leaves space for new research questions. From Fig. 2.7a it can be seen that for a conventional scheme [96], for a certain angle of attack, secondary loss can be negative and hence, up-physical, especially for low aspect ratio blades [100]. Coull [100] pointed out avoiding such problems for aspect ratios in the order of $h/C_x = 3$ and thin inlet BL of $\Theta/C_x = 0.01$ where h is the blade height, C_x is the axial chord and Θ is the BL momentum thickness. Based on oil visualisation results [101] two different regions in BL have been found: prime and secondary, bounded by the passage vortex separation lines. Loss in the first region is mostly affected by Ma (if transonic), Re and airfoil pressure distribution whereas the loss in the secondary region is affected by the passage vortex strength and probably chord-wise pressure distribution has a smaller influence [98]. According to Benner [98], profile loss can be expressed as:

$$Y_{profile} = Y_{mid}(1 - \frac{Z_{TE}}{h}) \tag{2.2}$$

where: Z_{TE} is the span-wise penetration depth of the S_4 separation line from the endwall at the trailing edge (see Fig. 2.7b), Y_{mid} is the mass-averaged total pressure loss coefficient and h is the span. Therefore profile loss represents the midspan loss accounting for the fraction of suction area with nominally 2D flow and secondary loss includes endwall loss and the loss generated in the airfoil BL secondary region [98]. Correlation for this penetration depth proposed by Benner in 2006 is the following:

$$\frac{Z_{TE}}{h} = \frac{0.1 \cdot F_t^{0.79}}{\sqrt{CR} \cdot (\frac{h}{c})^{0.55}} + 32.7(\frac{\delta^*}{h})^2 \tag{2.3}$$

where: F_t is the tangential loading coefficient, $CR = \cos\alpha_1 / \cos\alpha_2$ is the convergence ratio, h/c is the airfoil aspect ratio and $\frac{\delta^*}{h}$ is the non-dimensional inlet endwall boundary layer displacement thickness where $\delta^* = \int_0^\delta (1 - V/V_e)dz$ with δ being the boundary layer thickness, V and V_e the velocity and the velocity free-stream respectively. F_t is defined as:

$$F_t = 2(\frac{S}{Cx})\cos^2\alpha_m(\tan\alpha_1 - \tan\alpha_2) \tag{2.4}$$

where α_1 and α_2 are the inlet and outlet flow angles respectively, α_m is the mean vector angle defined as:

$$\tan\alpha_m = \frac{1}{2}(\tan\alpha_1 + \tan\alpha_2) \tag{2.5}$$

With the new approach, also an empirical prediction method for secondary losses in turbines has been established [99]:

$$Y_{secondary} = \frac{0.038 + 0.41 \cdot \tanh(1.2 \cdot \delta^*/h)}{\sqrt{\cos\gamma} \cdot CR \cdot (h/C)^{0.55} \cdot (\frac{C \cdot \cos\alpha_2}{Cx})^{0.55}} \tag{2.6}$$

where γ is the stagger angle measured from the axial direction, in degrees. This equation holds for $h/C \leq 2.0$.

2.5.2. DIFFERENT DEFINITIONS OF LOSS

A popular and effective way of defining loss coefficient is Total Pressure Loss Coefficient because it is readily available from the test results measured for the cascade and also during the CFD post-processing. For turbines, it is defined as:

$$\zeta_p = \frac{P_{t1} - P_{t2}}{P_{t2} - P_2} \tag{2.7}$$

where: P_{t1} and P_{t2} are the total pressures at the inlet and outlet respectively and P_2 is the average static back-pressure. Another popular factor is Enthalpy Loss Coefficient defined for the turbine as:

$$\zeta_e = \frac{h_2 - h_{2is}}{h_{t2} - h_2} \tag{2.8}$$

where: h_2 and h_{t2} are the static and total enthalpy at the outlet respectively and h_{2is} is the outlet static enthalpy for the isentropic expansion.

The flow within conventional contemporary turbines is almost adiabatic therefore thermodynamic irreversibility can be considered as the main reason of loss. For stator blades, we can assume that the loss of total pressure can be proportional to an increase in entropy [18]. Entropy Loss Coefficient can be defined as:

$$\zeta_s = \frac{T_2 \Delta s}{h_{t2} - h_2} \tag{2.9}$$

where Δs is the change in entropy and point 2 refers to expanded/outlet flow conditions. For more, see: [18].

2.5.3. RELATION BETWEEN THE DRAG AND THE LOSS

Although drag is a very suitable factor for external aerodynamics, its application in turbomachinery is rather small. This is due to the problem in defining its direction [18]. Although it contributes to lift and axial force in turbines, it is cumbersome to determine what part of this contribution actually accounts for the pressure difference. Entropy can rise in non-uniform flows even if there is no friction and it tends to increase when high viscous forces meet with substantial velocities [18].

2.5.4. REHEAT EFFECT

Flow with a fixed loss coefficient and flow velocity produces less entropy at high temperature as compared to the same process at lower temperature [18]. Since the entropy is created inversely proportionally to the local temperature in the machine (e.g. $T\Delta s = \zeta \cdot \frac{V^2}{2}$ [18]) big amount of entropy can be expected in the last turbine stages where the flow is expanded to lower pressure. Even though the first stator is exposed to adverse pressure and shock waves, the loss due to thermodynamic irreversibility might be still large in the further stages where temperatures are lower. It is aggravated when the ratio of the temperatures increase, specifically in high speed machines [18].

2.5.5. BOUNDARY LAYER AND ENTROPY

The production of entropy in BL is directly related to the viscous shear work developed into heat at a certain temperature. At larger Re numbers, an exchange of mass, momentum and energy in the turbulent BL results in big velocity gradients, the scale of mixing cannot be computationally handled by molecular viscosity alone and requires Eddy Viscosity modelling. In the vicinity of the blade wall we can distinguish two important sublayers [102]:

1. Viscous Sublayer located next to the wall where the flow is almost laminar, and the viscosity plays a dominant role in momentum and heat transfer.
2. Logarithmic Layer where the mixing is mainly dominated by turbulence.
3. Buffer Bayer located between these two, where the effect of turbulence and viscosity play equal role.

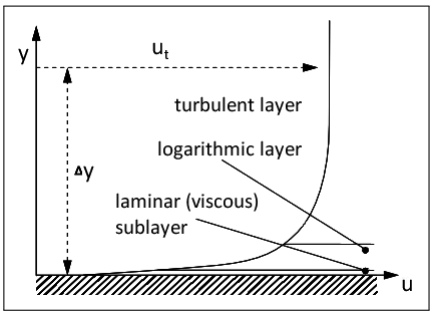

Figure 2.8: Sublayers in the near wall region [102]

The biggest amount of BL entropy is expected to be created within those layers. Turbulent BL dissipation coefficient is less dependent on shape factor and occurs at 2-5 times bigger rate [18] as compared to laminar cases. Comparing to compressor blades, turbine blades BL are characterised by the smallest dissipation coefficient which decreases further with an increase of Re number [18] (see Fi. 2.9).

On this context, transition prediction can be mentioned, as important to determine what part of the airfoil is dominated by turbulent flow and hence influences the performance factors. We can distinguish two types of BL transition, namely:

1. Natural - triggered by inherent BL instabilities
2. By-pass transition resulting from external factors such as free stream turbulence, diffusion, wakes, surface roughness effects and convection.

The first one is impossible to predict with the contemporary CFD codes but the by-pass transition prediction has been achieved in the past with a low-Re 2-eq code, which was however, tailored to this special case [103]. In this work, due to using RANS, BL will be assumed turbulent all along the airfoil resulting in an over-prediction and under-prediction of losses in this region depending on the Re domain. It can be noted that this does not affect e.g. regions further away from the walls or e.g. freestream, where flow can be laminar.

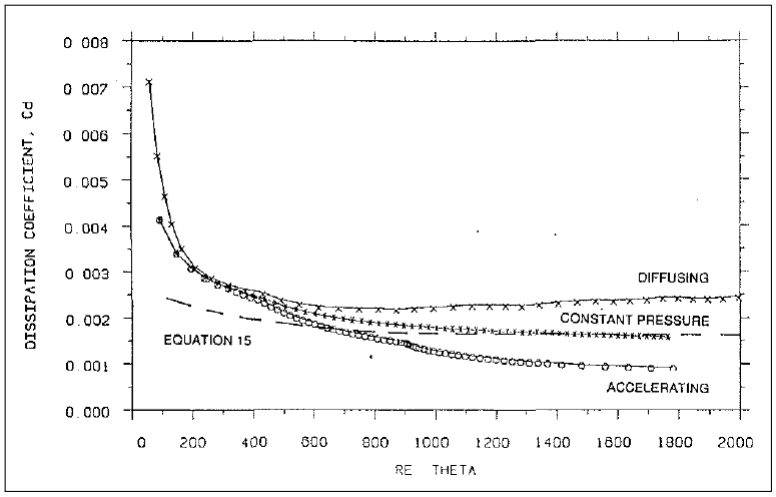

Figure 2.9: Dissipation coefficients for turbulent BL [18]

2.5.6. MIXING PROCESS

In every flow in which shear forces exists entropy is generated. Regions where entropy creation due to mixing is high are particularly wakes, e.g. behind blade trailing edges due to the rounded shape of the blade. They cannot be sharpened due to structural loads in the aft part of the airfoil to allow a high aerodynamic lift to structural weight ratio. A big impact on the trailing edge loss exerts the so called Base Pressure Coefficient[18], which as a term contributes towards approximately 0.0075 of the profile loss coefficient which is usually around 0.03 and accounts for about 30% of the profile loss [18]. To improve this behaviour several solutions have been tested [18]. For the blunt trailing edge blades a "splitter plate" reducing the dissipation can raise the base pressure. An elliptical end has the similar effect and also reduces the loss. J.D. Denton [18] provides a theory which applies when the BL separates at the trailing edge (see figure 2.10a), "provided that the static pressure just upstream of the trailing edge can still be assumed to be uniform" [18]. Then, BL displacement thickness can be possibly larger than the one of the trailing edge. It has been concluded that only bigger wakes will significantly curb the performance [18].

The same author quotes that 10% 'blockage' causes a loss of 1% for the thin trailing edge. This is important in design decisions, such as the problem of separation and the wake at the first, highly loaded stator characteristic for small-scale centrifugal ORC turbines [13]. According to the same author, separation increases the size of vortices which results in larger dissipation in the wake region compared to trailing edge only. Arguably, total dissipation can be roughly proportional to separation and trailing edge thickness [18]. In turbines, the flow acceleration during expansion alleviates the velocity gradient and decreases the loss due to separation. Also eddies and leakage flows are characterised by strong shearing, but it is cumbersome to estimate the rate of entropy created locally. The details of the mixing itself are not necessary because the flow at the certain downstream boundary is uniform. It has been proven [18] that this process occurs within the entire mainstream flow, not only with the layers in the vicinity of the injected, mixing fluid. This allows for neglecting details of the mixing itself during the numerical solutions as long as the trailing edge is correctly predicted [18].

2.5.7. SHOCK WAVES

High thermal conduction and viscous forces inside shocks result in strong irreversibility which is aggravated by a very thin spectrum in which this phenomenon occurs (thickness in the order of 10^{-8}m depending on the Mach number [104]). The significance of the interplay between the losses becomes apparent when the shock occurs in the vicinity of the trailing edge. Although transonic turbines involve compression shocks, the pressure differences within the blade passage are relatively small and hence do not affect the performance significantly [18]. This is not the case when shock is located at the trailing edge. The low pressure at the suction side at the end of the blade results in redirection of the flow towards this point which is immediately compressed by the incoming shock. "The most serious consequence of transonic flow in turbines is the shock system at the trailing edge, as shown in figure 2.10b. The low base pressure formed immediately behind the

trailing edge can generate a very large trailing edge loss" [18]. An application and loss estimation of the control volume to model these effects in choked turbine blades can be found in [105].

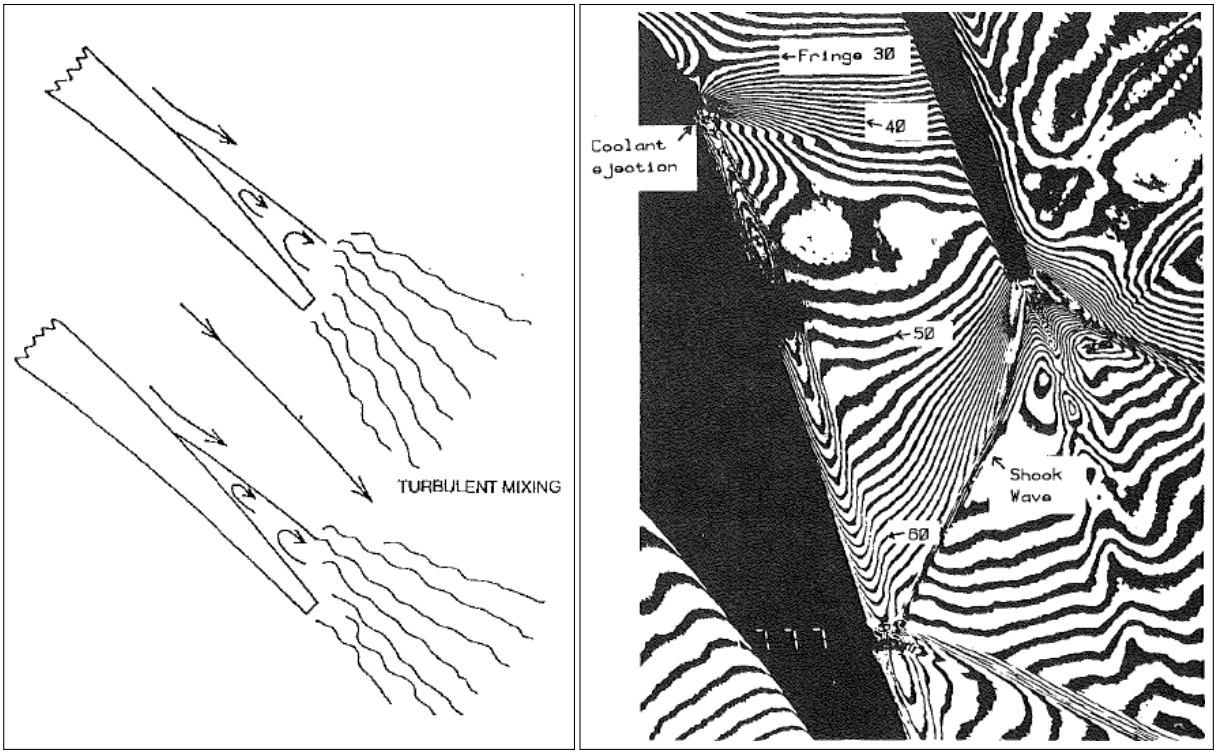

(a) Trailing edge with a separated boundary layer and a wake

(b) Shock wave in turbine blade with suction surface coolant ejection

Figure 2.10: Loss mechanisms in turbomachinery [18]

2.5.8. BOUNDARY LAYER SEPARATION AND SHOCK WAVE

Shock waves are usually deleterious by leading to: drag rise, flow separation, adverse aerodynamic loading, strong aerodynamic heating and poor performance [18]. In two dimensional flows, separation becomes apparent when the wall shear-stress or the skin-friction coefficient vanishes at a certain point. After this separation point, the wall shear stress becomes negative. For three dimensional phenomena it is not enough because there is no privileged direction along which the sign of the wall shear-stress has an intrinsic significance (except a few special cases such as symmetry planes or infinitely swept wings) [106].

One of the first landmark definitions of three dimensional flow separation originate from concepts proposed by Legendre (1952 and 1977) and Lighthill (1963) [106]. The idea introduces a limited number of singularities into a family of skin friction lines and an obstacle. They can be defined as isolated surface points where there is no skin-friction vector and no surface vorticity. Among them, we can distinguish nodal points and saddle points. Authors make a distinction between global and local separation and underline the distinction between two dimensional separation phenomena and three dimensional, real case. This plays an important role while choosing between 2D and 3D domains in CFD where the secondary effects can be large. Both nodal and saddle points however, are "characterised by a particular skin friction line, also called the separation line that "separates" the skin-friction lines into two sets" [106].

External streamlines are only slightly deflected, whereas skin-friction lines turn abruptly on approaching the separation line. It is important for analysing Mach contours and streamlines of turbine blades. "The surface flow pattern could give a misleading impression that the entire flow field is highly skewed from the streamwise direction, which is not the case." [106] The vast part of the BL might be utterly not affected. The big part of the skewed flow occurs in the thin low energy fluid region in the wall vicinity. Wall shear-stress usually does not vanish on a separation line therefore the elimination of this vector should not be used as a criterion for

separation in three dimensional flows. "It is of no help in identifying separation from wall shear-stress measurements" [106]. "The separation phenomenon is characterized by a very rapid turning of the skin-friction lines when they approach the separation line from upstream. This could give the impression that they are tangent to the separation line. On the other hand, the tendency towards the separation line from downstream as well as the tendency towards a reattachment line is far more progressive." [106]. In case of shock, a BL separation bubble might occur at the foot of the shock with accompanying dissipation downstream and loss. This high pressure rise, although acceptable in the compressor blades, is indeed detrimental in the turbine. In the Re number regime concerning small-scale ORC turbines ($2 \cdot 10^5 - 6 \cdot 10^5$), the roughness greatly affects the turbulent boundary layer.

2.5.9. HEAT TRANSFER

Although the heat transfer to the environment occurs for big machines on a very small scale and is often treated as negligible, this is not the case for smaller turbines. Relatively large surface area and comparatively small volume characteristic for small machines contribute to violation of this assumption [18]. Relatively small temperature range characteristic to ORC technology and hence smaller heat transfer are favourable for using this adiabatic assumption.

2.5.10. TRAILING EDGE LOSS

It has been found that for a low speed turbine blade, approximately 1/3 of total loss was generated behind the trailing edge [18]. Velocity profiles (see figure 2.11) at and downstream of this turbine blade showed a still significant change at 10 diameters downstream [107] and exert a deleterious effect on downstream components.

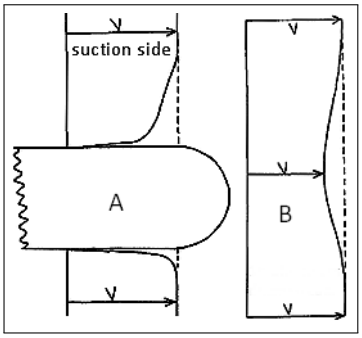

Figure 2.11: Velocity profiles at and downstream of a simulated turbine blade trailing edge [18]

2.5.11. TIP LEAKAGE

One could think of the tip leakage phenomena as of the effect similar to the induced drag on the wing where wing tip vortices change the speed and direction behind the trailing edge inducing downwash behind the wing. This inviscid effect indeed creates additional kinetic energy but from the turbomachinery viewpoint - it does not create entropy[18]. A more extensive elaboration on tip leakage measurement can be found in [108] and [109]. Leakage gap is usually a compromise between manufacturing difficulty and aerodynamic requirements [72]. Unshrouded turbine blades (see Fig. 2.12a and 2.12b) imply much stronger interplay between the leakage and the main flow as compared to shrouded blades, hence shrouded blades are generally preferred [65]. As a result of a decrease in cross section in the tip channel the flow accelerates leading to higher meridional velocity and impinges on the main flow behind the blade enhancing mixing. This effect can be smaller if difference between the leakage flow and stream-wise velocity of the mainstream in the suction side is smaller [18]. The resulting reduction in lift due to smaller mass flow does not only affect the tip region, but the vast span-wise region. This phenomena has inviscid background and might not be related directly to entropy generation but rather loss of lift [18].

Usually, a separation bubble forms right behind the edge (see figure 2.12a) next to the pressure surface and the scale of this flow contraction depends on the radius of the corner between the tip and the pressure side [18]. Some sources indicate that the vortex ensuing from the leakage jet has a blocking effect and implies lower static pressure than it would result from a two dimensional case [110]. A resulting from velocity difference and shearing between the flows vortex street occurs and rolls up downstream. This mixing continues to the subsequent blade rows and hence it is cumbersome to estimate its contribution towards the overall loss as the diffusion may still increase. Another issue is the relative motion between the casing and the tip of the blade. According to [18], available methodologies on leakage flows do not account for this phenomenon. In turbines, this relative motion reduces the leakage flow. In centrifugal machines, due to increasing peripheral along the machine, this implies stronger reduction in the leakage in the last passages. This phenomenon has been investigated in [111] and [110].

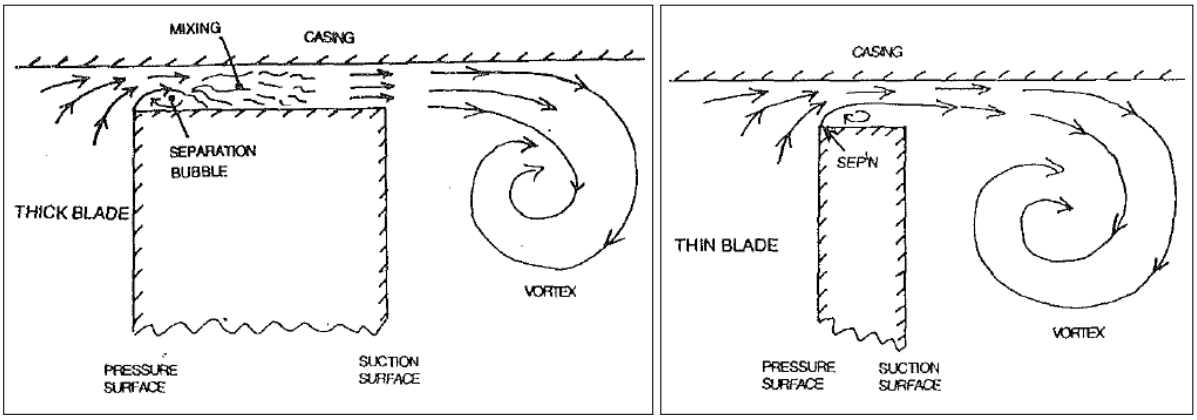

(a) Thick blade (b) Thin blade

Figure 2.12: Flow over the tip gap for an unshrouded blade [18]

2.5.12. ENDWALL LOSSES

A summary of main features of the secondary flows can be found in the work of G. Persico [112]. Several main characteristics have been pointed out as follows.

1. Passage vortex, "located in the suction side region of the passage downstream of the trailing edge" [112]. This vortex is esentially induced by the presence of the BL in the span-wise direction [6] by "redistribution of the inlet BL vorticity" [112]. The flow in BL deviates from the pressure side to the suction side due to pressure difference because the momentum is lower than in mid-span flow.

2. Shed vortex, located in the downstream wake region [112]. It is generated by the interaction of the passage vortices with the wake [112]. This vortex is counter-rotating w.r.t. passage vortex.

3. Horse-shoe vortex, forming at the leading edge endwall BL [112]. It is created due to stagnation of the flow and splits into two vortices, which subsequently merge with the passage vortex [112].

4. Corner vortex, "generated in the corners between the blade tips and the endwalls by the action of the passage vortex" [112].

5. Tip leakage vortex due to tip leakage phenomenon explained earlier. The vortex is generated due to "rolling up of the flow in the tip leakage region" [112].

Although interaction between the shock and BL and the mixing behind the t.e. is cumbersome and still under development, the prediction of secondary effects at the annulus walls belong to the most difficult loss mechanisms and to the vast extent is still based on empirical knowledge [18]. One of the factors affecting the secondary effects is the upstream BL thickness and the geometry which forces streamlines to skew. The greater these factors are, and the bigger the aerodynamic load, the sooner the endwall BL rolls off onto the suction surface. This inviscid secondary phenomenon is a result of vorticity which originates from viscous shearing in the annulus vicinity. From the suction surface it still traverses downstream towards the trailing edge where in the endwall corner, above the suction surface, it occurs as a high entropy region. Strong cross flow pressure gradient which tilts the BL towards the suction side makes the endwall BL thinner. This cross flow induces a so called "corner vortex" [18] which rotates in the opposite direction with respect to the "main passage vortex". Since the endwall BL remains thin at the trailing edge, as it travels downstream, it grows and along with a decrease of the main vortex and cross flow induced it becomes again more two-dimensional.

Due to change in the frame of reference resulting from gap separating rotors and stators the endwall BL will be skewed from the main streamlines except the first stator. This aggravates the secondary effect and has been investigated by Bindon [113] and Walsh [114]. They underline that this skewing had a big impact on secondary effect and hence loss. The dissipation rate is expected to be similar to the one in the BL, however, to the author's knowledge there is no publication about BL dissipation due to cross flow. Nevertheless, the change in the streamlines due to skew and due to aggravating effect of secondary flow field the resulting vortex will enhance the kinetic energy production also called "secondary kinetic energy" (SKE) [18]. Apart from

the aforementioned factors it rises with the turning of the blade and even from the endwall BL. This effect is alleviated by the viscous forces originating from the inlet BL which is primarily responsible for the secondary flow. SKE increases with the vortex length resulting from the flow acceleration during the expansion. This is the point where the dissipation leads to a big entropy generation. Fig. 2.13a and Fig. 2.13b visualise secondary flows according to Coull [100] and Sharma and Butler [97], respectively.

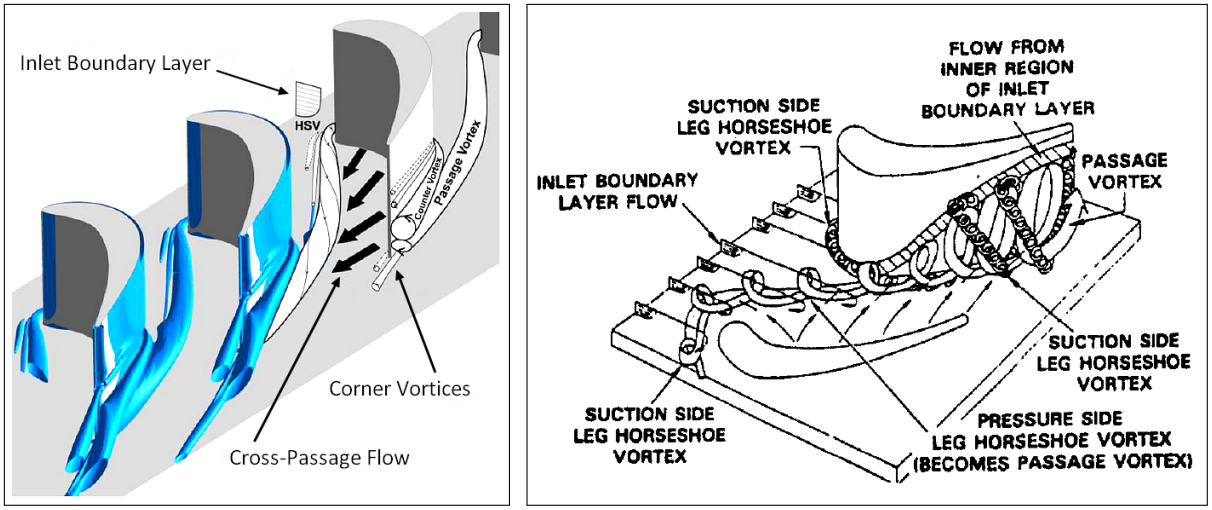

(a) Secondary flow in a turbine cascade [100]

(b) Vortex pattern described by Sharma and Butler [97]

Figure 2.13: Secondary flow in a turbine cascade

It has been concluded that the biggest (around 2/3 [18]) part of the entropy accounting for the endwall loss originates from the annulus BL which is inversely proportional to the aspect ratio. The second big contribution comes from mixing aggravated by the secondary effects. The third contribution comes from the SKE, accounting for approximately 1/4 of the endwall losses. Other factors are: local separations, premature transition and BL thickening.

2.6. COMPUTATIONAL FLUID DYNAMICS

The strategy applied in this work is based on the Finite Volume approach where each node of the domain is accompanied by a small volume. By using divergence theory, volume integrals in Partial Differential Equations (PDE) which involve divergence are converted into surface integrals. The resulting surfaces allow to establish the respective fluxes at the boundaries of each small surrounding volume [115]. They determine the time evolution of the cell averages which are associated with the cell centre nodes, however, they represent the mean solution within the entire cell. This approach has been preferred as it is advantageous in terms of memory requirements and speed which plays an important role for larger problems, big Reynolds numbers and also phenomena which are source-term dominated such as chemical reactions (e.g. combustion) [116]. The governing PDE: NS equations, mass, energy conservation and turbulence relations are re-written in a conservative form. This approach has its advantage in solving discontinuous solutions due to the integral form. For further details, the reader is advised to investigate the work of R. Herbin [115]. When dealing with a shock-wave such as the one expected on the upper side of the first stator airfoil, this leads to Rankine-Hugoniot relation (in a form of 3 equations: conservation of mass, momentum and energy) and results in a correct shock speed. This conservative approach is mainly visible in the way the derivatives are split before being written into a numerical form.

2.6.1. CLOSURE PROBLEM

An example of a simplified approach is Reynolds Averaged Navier Stokes (RANS) equation model where the quantities are split into the mean and fluctuating parts due to application of Reynolds Averaging. After simplifying the terms it becomes apparent that an additional, convective term occurs which can be re-written as Reynolds Stress Tensor [11]. Derivation of a conservation laws for this tensor can be expressed as the Reynolds Stress Transport equations (RST). These equations involve: advection, turbulent diffusion, produc-

tion as a source term responsible for the increase of turbulence intensity by energy transfer from the mean flow, viscous diffusion, pressure diffusion, pressure strain correlation and dissipation. For every unknown we could derive a conservation law, which would however include new unknown quantities. Therefore we are not able to resolve the closure problem this way. The approach undertaken in this work is based on empirical approximations in a form of commercially implemented turbulence models.

2.6.2. $k-\epsilon$ MODEL

One of the first successful models was introduced by Jones & Launder in 1972 [86] being the first two-equation turbulence model for RANS simulations, also known as $k-\epsilon$ model. Unfortunately, the assumptions of isotropic turbulence and energetic equilibrium, however acceptable for exterior flows, do not hold in boundary layers and most real flows, therefore this model would not capture anticipated flow behaviour next to the blade wall [11]. The ϵ equation contains a term which cannot be calculated at the wall thus wall functions must be used.

2.6.3. $k-\omega$ MODEL

Another interesting solution was proposed by David C. Wilcox in 1988 [117]. The model is very similar to the aforementioned $k-\epsilon$, yet minute differences indeed make a difference. The first transport equation is also for the turbulence kinetic energy k but the second, postulated transport equation deals with the specific turbulence dissipation rate ω rather than ϵ [11]. The resulting changes in both transport equations result in a model that is able to capture pressure gradients, separation and other boundary layer flows. The model equations do not contain terms which are undefined at the wall and they can be integrated to the wall without using wall functions. The family of these models is accurate and robust for big spectrum of BL flows with (adverse) pressure gradient. The shortcomings of this model appear in terms of sensitivity in the inflow and boundary conditions and an overestimation of turbulence in stagnation points.

2.6.4. SST MODEL

With the aforementioned pros and cons of both models, in 1993, Florian Menter [17] proposed blending $k-\omega$ model with the $k-\epsilon$ one. The resulting Shear Stress Transport (SST) model gained its popularity due to its compromise between good BL approach with acceptable results further away from the wall. Specifically, the $k-\omega$ based SST model uses a blending function to gradually transition from the standard $k-\omega$ model near the wall to a high Reynolds number version of the $k-\epsilon$ model in the outer portion of the boundary layer [11]. It also involves a modified turbulent viscosity definition to include the transport effects of the principal turbulent shear stress. It has to be noted that this model does not provide better results than $k-\omega$ and $k-\epsilon$ models separately. Due to wall-scale equation implemented, this model is slightly computationally heavier than other 2-eq. based models. Mesh independence study proved it is more stable as compared to EARSM.

2.6.5. SPALART-ALLMARAS MODEL

A different approach has been undertaken in 1992 [118], when a popular in the field of aerospace engineering model was invented by P. R. Spalart and S. R. Allmaras. This one-equation model has been based on a postulated transport equation for a functional of the eddy viscosity allowing to resolve it near the wall [11]. A distinguishable feature of this model is that it does not necessitate length scale calculation which is related to the local shear layer thickness. Although there is no underlying theory it has been designed for wall-bounded flows characteristic for turbomachinery. It is characterised by good accuracy for adverse pressure gradient BL separations which unfortunately is not the case for flow reattachment and free shear layers. These challenges make this model less suitable for prediction the decay of homogeneous and isotropic turbulence.

2.6.6. RSM MODELS

The limitation of eddy viscosity modelling can be worked around by using the full Reynolds Stress Models which solve directly model transport equations for each of the six unknown Reynolds Stress Tensor components [11]. It is based on derivation of simplified and closed model transport equations, which involve approximations of higher-order correlations and the dissipation rate tensor. DNS proved that the pressure diffusion is negligible therefore this term is neglected in the model transport equations. It has been assumed that the turbulence dissipation affects only small, relatively homogeneous and isotropic scales. The turbulence production, mainly affected by external energy input and strongly dependent on geometry and BC occurs in large, inhomogeneous and anisotropic turbulent integral scales. The distinction between the large,

long-living scales and the small, low-energy-content ones is assumed to happen due to the so-called "energy cascade" within the inertial range. The dissipation rate tensor is modeled as an isotropic tensor and can be expressed as a scalar. This dissipation of the small scales occurs specifically due to viscous forces which become more dominant for the small scales. This is due to the vorticity conservation which implies larger velocity gradients and hence larger dissipation. More importantly, the pressure-strain correlation is not able to produce or dissipate turbulence energy as it redistributes turbulence energy between the components of the Reynolds stress tensor instead. This specific correlation affects the anisotropy of the Reynolds Stress Tensor and it can be divided into two terms, the slow and the rapid one. The first accounts for relaxation to the isotropic equilibrium state and the second describes the immediate effects of mean flow gradients and external forces, which drive the Reynolds stress to anisotropy. Early in the 1975, Lauder, Reece and Rody (LRR RSM model) [119], proposed a solution which utilised only the first (linear) term of the generic model. Later on, in 1991, Speziale, Sarkar and Gatzki (SSG RSM model) [120] involved also a quadratic term of the generic model. Avoiding isotropic viscosity assumption makes RSM approach suitable for highly swirling flows and the quadratic pressure-strain option improves performance for many basic shear flows.

2.6.7. EARSM - NONLINEAR EDDY VISCOSITY MODEL

The transport equation for the Reynolds stress anisotropy tensor reduces to an implicit algebraic relation provided that anisotropy does not vary significantly in both time and space. "Also in many inhomogeneous flows of engineering interest the flow is steady and the advection and diffusion of the Reynolds stress anisotropy may be neglected. The advection and diffusion of the individual Reynolds stresses scale with those of the turbulent kinetic energy. The set of transport equations for the Reynolds stress anisotropy is then reduced to an algebraic equation system, which is implicit in the Reynold stress anisotropy." [16] Even for the linear pressure strain correlation modelling, the Reynolds stresses are nonlinear. This approach represents the so-called algebraic Reynolds stress models (ARSM) which models Reynolds stresses but ignores the transport terms. Since solving this system of implicit equations results in a large computational time, it diminishes the gain from the ARSM compared to the approach with the full transport form. In 1975, a landmark work of S.B Pope [121] presented an explicit form (EARSM) for two-dimensional flows. EARSM reconstructs the Reynolds stress tensor or an anisotropic eddy viscosity tensor from a reduced number of transport equations [11]. Thus the eddy viscosity assumption has been replaced by a more general constitutive relation for the second-order correlation in the Reynolds averaged equations. These models "are numerically and computationally robust and have been found to be comparable to standard two-equation models in computational effort." [16]

2.6.8. RELIABILITY OF RANS

The experiment performed at TU Darmstadt [122] indicated a noteworthy discrepancies of RANS two-equation models with respect to the in-house LES code and also RANS Reynolds Stress Models. Despite low Reynolds number and incompressible fluid assumption in the experiment, inexpensive two-equation RANS models fail to predict separation bubble which has to be strongly taken into account while performing entry simulations over the first stator. The assumption of the proportionality between mean shear rate and deviation from the Reynolds Stress Tensor expressed as eddy viscosity results in a lack of distinction between the individual elements in the Reynolds Stress Tensor. As a result, anisotropic influences such as streamline curvature and directional volume forces, e.g. gravity are incorrectly predicted. European Research Community On Flow, Turbulence And Combustion (ERCOFTAC) test case 9.2 [11] has been designed for the evaluation and cross comparison of numerical methods (see Fig. 2.14a and Fig. 2.14b).

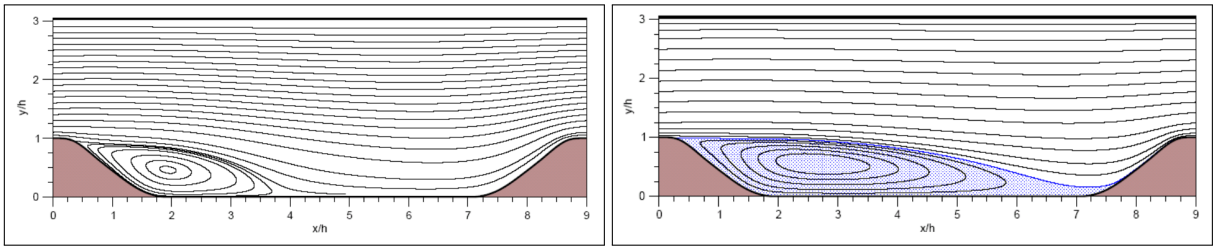

(a) LES with academic flow solver, TU Munich [11]. (b) CFX, 2D RANS, SST model proposed by Menter [17].

Figure 2.14: ERCOFTAC test case 9.2 [11]. Pseudo streamlines based on time-averaged velocity.

3

NUMERICAL MODEL

3.1. GEOMETRY AND DISCRETISATION

Discretisation has been divided into sub-domains wherein each blade row has its own periodic mesh (see Fig. 3.4a). Blade dimensions have been obtained from the in-house tool zTurbo. The geometry has been created by means of short input files representing hub, shroud and blade points. Importing these points to Turbogrid enables full geometry creation. Near wall element size accounts for y+ offset and Reynolds numbers obtained from zTurbo. Because of using SST model, y+ < 1.0 has been maintained for all blades. Quasi 3D meshes are 0.1 mm thick and contain 2 cells in the span-wise direction - a minimum achievable in Turbogrid. 3D meshes involve full blade length and have been simulated for two cases: with and without tip clearance.

All meshes are structured which rules out complex connectivity matrices and allow direct projection onto a Cartesian domain. Mesh cells are topologically similar and the max. amount of connections does not exceed 10. Direct data storage and access have a positive influence on computational time. Structured approach allows for easy application of BL inflation which is paramount to capture adverse velocity gradients near the wall because turbulence production mostly occurs within $y+ < 20$ [11]. Cell position with respect to flow vectors can affect the accuracy, therefore, aligned with the streamlines structured grid lines reduce the effect of numerical diffusion. This truncation error occurs due to discrete approximation of physically, continuous operation and is more profound in transient simulations [11].

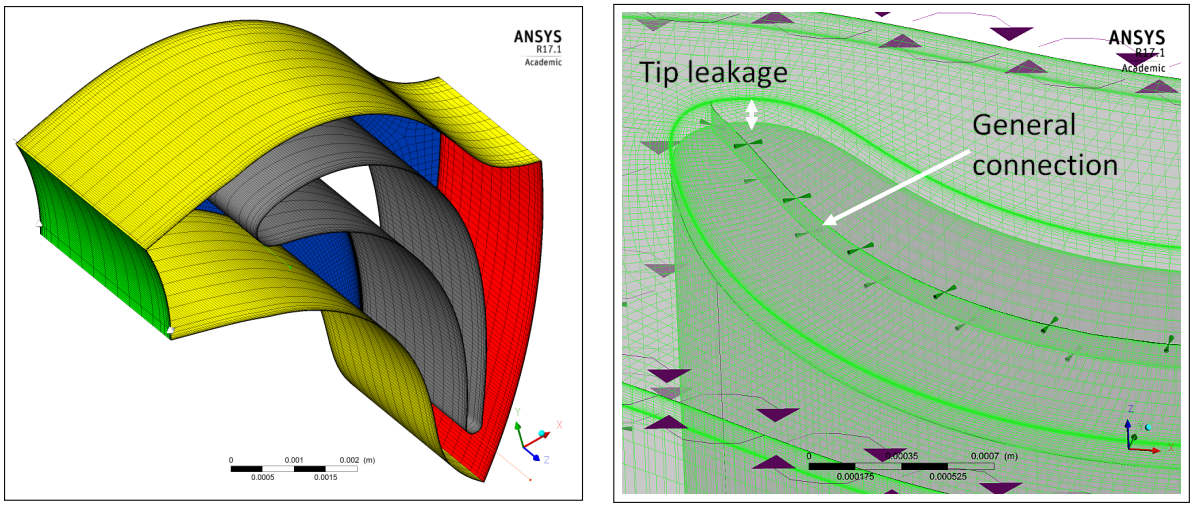

(a) Optimal 3D mesh for the first stator without tip clearance, 750 000 nodes.

(b) General connection and GGI applied in the tip leakage section for the first rotor. Leakage gap of 0.1 mm.

Figure 3.1: Domain discretisation.

The downside with respect to flexible, unstructured grids becomes apparent in blocking strategy, which for complex geometries might be cumbersome. Perfect orthogonality is for most geometries impossible, therefore a quality check is vital. BL inflation always leads to larger edge length ratios which result in faster propagation of information along the shorter edge. One of the most critical factors are Edge Length Ratio, skewness a.k.a. Face Angle and Maximum Volume Ratios - presented in table 3.1 Of poorer quality are cells with large face angles, see figure: B.1a in appendix B, wherein large connectivity also occurs. Optimization algorithm implemented in CFX helps to create a smooth O-type of grid (see figure: 3.2). In case of tip leakage, the shroud does not contain the gap resulting from the blade contour. Grid cells originating from the suction and pressure sides are linked with general connection (see figure: 3.1b). No constraints on mesh motion is applied to nodes. All the interface fluxes in this work (mass, momentum, turbulence, heat transfer) are conservative.

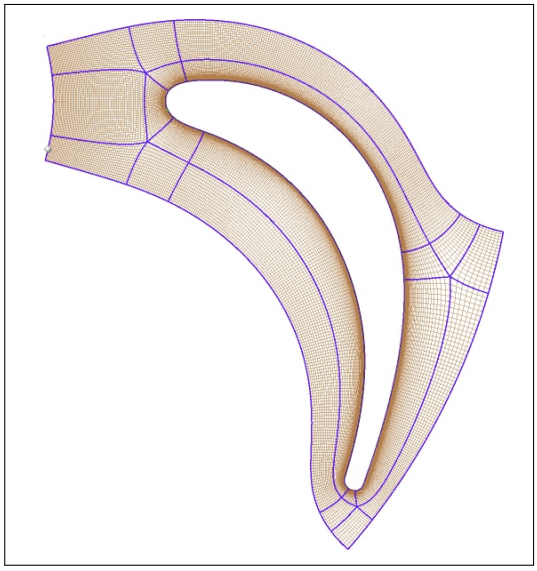

Figure 3.2: The topology and blocking strategy applied in Turbogrid. The same topology applies to 3D meshes.

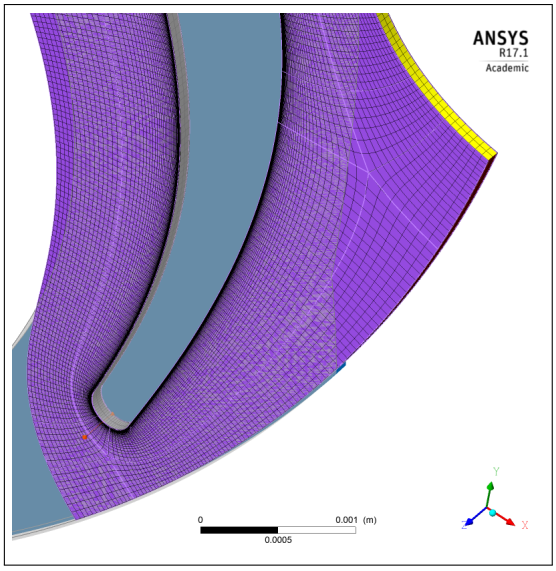

Figure 3.3: Optimal Quasi-3D, 2-cell thick mesh of the first stator, 100 000 nodes.

Face angles are of very good quality and do not diverge far from 90°. The value of maximum edge length ratio for 3D case is slightly big but has been confirmed during the mesh sensitivity analysis. Larger stretch of cells in 3D domains allows for significant reduction of computational overhead.

Table 3.1: Domains' quality for the first stator after mesh sensitivity analyses

Variable	Quasi-3D	3D	Unit
Minimum Face Angle	35.878	39.396	degree
Maximum Face Angle	133.795	129.657	degree
Maximum Element Volume Ratio	1.86	3.82	[-]
Minimum Volume	1.78e-17	2.64e-20	m^3
Maximum Edge Length Ratio	1802.28	10056.6	[-]
Maximum Connectivity Number	10	10	[-]

3.2. MATERIAL PROPERTIES

Hexamethyldisiloxane as a working fluid is specified in a dry, gaseous state. It has been defined in the material library as a pure substance and modelled by means of Peng-Robinson equation of state (1976) [123]. It has become an industry standard for this kind of applications partly due to reasonable accuracy in the vicinity of the critical point, applicability to all fluids and natural gas processes and the possibility to express properties using Acentric Factor and critical parameters. The specific heat capacity is expressed by the zero pressure coefficients by means of a fourth order polynomial:

$$\frac{C_{p0}}{R} = a_1 + a_2 T + a_3 T^2 + a_4 T^3 + a_5 T^4 \tag{3.1}$$

where R is the specific gas constant and T is the temperature.

Table 3.2: Material definition in CFX

Variable	**Value**	**Unit**	**Variable**	**Value**	**Unit**
Specific gas constant (R)	8.31446	J/(K mol)	Minimum pressure	0	bar
Zero pressure coefficient a_1	43.88	-	Maximum pressure	20	bar
Minimum temperature	0	deg C	Dynamic viscosity	1.3538e-05	Pa s
Maximum temperature	1000	deg C	Thermal conductivity	0.036601	W/(mK)

As a reference state, a specified point of the average pressure and temperature is chosen depending on the inlet and outlet conditions of a given domain. E.g. for the first stage e.g. 8 bar and 300°C has been chosen which results in the reference enthalpy of 575 732.7 J/kg. From these parameters a change in enthalpy or entropy can be computed in the solver therefore it is recommended to keep them as average values depending on the domain. CFX creates internal tables for efficient property evaluation, therefore respective bounds have been chosen (see: table 3.2). Table 3.3 contains thermodynamic properties required to model real gas effects with Peng-Robinson [123] equation of state.

Table 3.3: MM properties specified in CFX

Variable	**Value**	**Unit**	**Variable**	**Value**	**Unit**
Molar Mass	162.38	kg/kmol	Critical Volume	0.00063	m^3/mol
Critical Temperature	518.75	K	Acentric Factor	0.418	[-]
Critical Pressure	1.939	MPa	Boiling Temperature	374.4	K

3.3. FLUID MODELLING

The angular velocity of the machine is 43092 rev/min. The axis definition has been done by means of a vector between two points: (0, 0, 0) and (0, 0, -1) - rotation axis points towards monitor screen (see more in [102]). The same can be achieved by choosing the rotation axis in the global coordinate system, in the model "Z" - pointing outside the monitor screen, and applying a 'negative' rotation of -43092 rev/min. The definition method plays a role in the time transformation methods applied initially in the unsteady simulations. Due to the implementation of CFX, they necessitate using global coordinate systems making only the latter option viable. The Continuous Fluid Morphology has been chosen as the continuous phase MM forms a continuously connected region in the domain. Fluid is not present in the un-connected parts of the domain. Because the simulations do not embrace dispersed phases, Minimum Volume Fraction for each phase is left blank in the pre-processor.

Reference pressure can be specified to avoid round-off errors. Because the dynamic pressure changes are substantial compared to the absolute pressure level, the reference pressure has been set up to 0 bar. All pressures in the simulation are measured with respect to this value. Due to radial outflow configuration the buoyancy is negligible and not considered in the model. All the stator domains are defined as a "Stationary Domain Motion". Mesh deformation can be applied to model flows with a varying geometry such as flutter and hence is neglected in this work. Fluid model accounts for the viscous work term in the energy equation. As a turbulence model, k-omega based SST model has been used as it proved the most stable during the mesh independence study. For the quasi-3D mesh of 4 cells thickness, EARSM was able to provide comparable results in a noticeably shorter time but begun to fail for finer meshes (from 250k inclusively).

Heat transfer modelling enables to compute the temperature at different points of the domain and involve: convection, conduction, mixing due to turbulent effects and viscous work. The Total Energy model has been chosen as "it models the transport of enthalpy and includes kinetic energy effects [102]." It is recommended

in applications where the kinetic energy plays an important role, that is from Ma = 0.3 onwards. The turbulent Prandtl Number has been set up to 0.9 by default and it allows to solve the momentum and thermal equations if a specific experimental data or CFX Expression Language (CEL) formula is not provided. For 3D turbulence, eddy viscosity and eddy diffusivity concepts are invalid, hence turbulent Prandtl number has no meaning [124].

The wall function can only be automatic and the algorithm applied requires explanation. Because viscosity influences transport processes, this problem becomes more complex near the wall, which is characterised by large gradients in the dependent variables. Right next to the wall, the so called viscous sub-layer is almost completely laminar and heat transfer and momentum exchange are dominated by molecular viscosity effects. Further away, in the logarithmic region, the mixing is mainly an effect of turbulence. Between the laminar (viscous) sublayer and the logarithmic one (see Fig. 2.8) we can distinguish the so called 'buffer' region where the viscous and turbulent effects are of equal importance [102]. The logarithmic law of the wall is applied in the regions where mesh is insufficiently coarse (over 11.06 [-]). This strongly depends on the computed y+ factor, which in turn is affected by the friction velocity at the nearest wall (u_*), the local kinematic viscosity (ν) and the distance to the nearest wall (y):

$$y+ = \frac{u_* \cdot y}{\nu} \tag{3.2}$$

The friction velocity can be expressed by means of wall shear stress τ_w and density ρ:

$$u_* = \sqrt{\frac{\tau_w}{\rho}} \tag{3.3}$$

The combustion, thermal radiation and electromagnetic modelling are not included in this work. Initialization is neglected in the steady state approach except tip leakage analysis wherein large convergence problems occur. Initialization is used in transient simulations and as an effective initial guess, a steady state, frozen rotor results are applied. This approach allows to model the wake effect on the downstream component performance at a single relative position from which machine starts its rotation. Whether Frozen Rotor or Stage (Mixing-Plane) initialisation is chosen, strongly depends on how fast the transient simulation stabilizes after the initiation. For turbomachinery purposes it is intuitive to apply a frozen rotor results because the machine starts operating at a given blade pitch configuration, however, this does not always decrease the convergence time, which for unsteady problems is considerable.

Blades are treated as adiabatic, no-slip walls with Dirichlet BC for velocity of the fluid directly next to the wall equal to zero ($\underline{u}_{fluid} = \underline{u}_{wall}$). Pressure gradient normal to wall and viscous normal stresses are also zero (Neumann boundary condition) [11]. Although surface roughness might contribute to turbulence production near the wall it has been neglected at this design stage (Smooth Wall). Therefore shear stresses and heat transfer coefficient will be probably larger for the manufactured blades. To obtain a good agreement with experimental data, a careful roughness modelling is advised for future experiments. Hubs and shrouds in quasi-3D domains are adiabatic free-slip walls where the shear at the wall is zero to focus on profile losses and for 3D cases, no-slip walls to account for the influence of annulus BL. 3D cases involving tip leakage feature special approach at the shrouds wherein a Counter-Rotating Wall condition is applied to differentiate between rotating fluid and a stationary casing. This boundary " (...) is assumed to be stationary with respect to the stationary frame, essentially in counter-rotation with the rotating fluid and uses a no-slip condition" [102]. Periodic BC in each domain imposes the same values of the variables at two opposite boundaries [11].

Inlet is defined with the total pressure of 12.186 bar and total temperature of 300.36 $°C$ where the turbulence intensity is assumed standard 5%. Flow at the inlet is subsonic and normal to boundary condition. Outlet static back-pressure varies depending on the domain and is based on results from zTurbo. To enhance convergence a small pressure profile decay is imposed by the recommended default 5% [102]. In such set-up, the calculated mass flow is part of the solution and is very "sensitive to the initial guess." [102] It is also possible to define velocity/mass flow at an inlet and static pressure at the outlet where inlet total pressure is an implicit result. To avoid difficulties in convergence in steady CFD, it is advised to avoid a combination of implicit results for boundary conditions at the inlet.

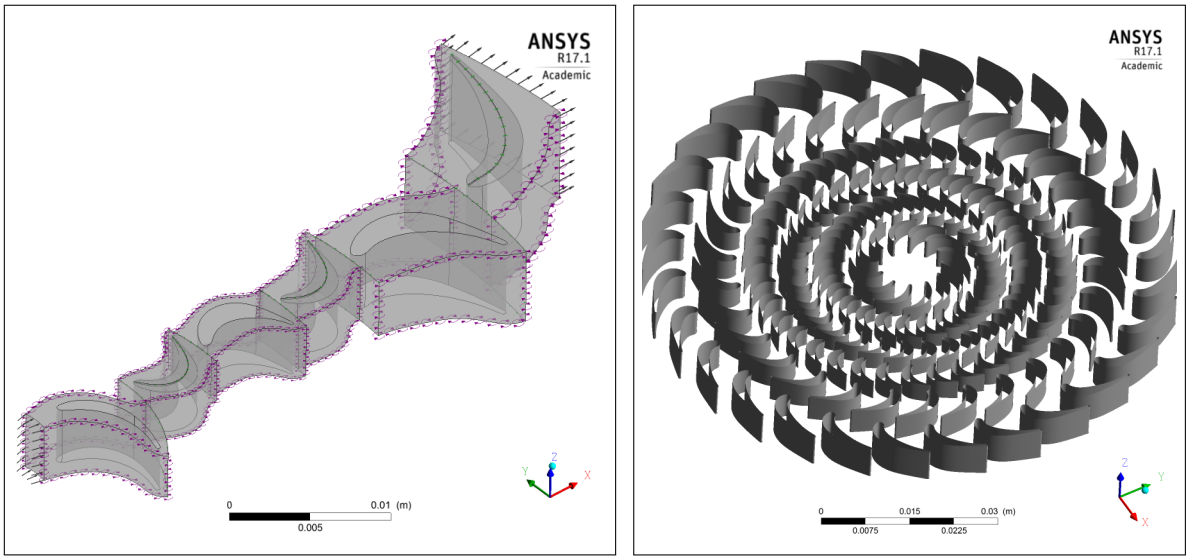

(a) Model definition in CFX-Pre

(b) Simplified 3D model of the mini-ORC ROT turbine

Figure 3.4: Mini-ORC ROT steady-state 3D model

Three types of fluid-fluid, stage interfaces are used throughout this work. Mixing-Plane circumferentially averages the fluxes through bands on the interface. It assumes that mixing from relative motion between domains is big enough to mix out all the upstream velocity profiles before entering downstream region introducing a "one-time mixing loss" [102]. Time-averaged interaction is resolved but transient effects are neglected, hence it is not reliable for models with "large circumferential flow variation w.r.t. pitch ratio" [102]. A downstream velocity constraint at the interface fixes total pressure to allow (downstream) velocity profile to account for influences located downstream. This makes solution in narrow gaps more 'physical'. Frozen rotor cases assumed single relative position of the components, hence a very special position when the effect on downstream components needs to be modelled. It does not involve transient effects and modelling errors arise when quasi-steady assumption do not hold.

Importantly, "losses incurred in the real situation as the flow is mixed, stationary and rotating components are not modelled" [102]. Transient interface yields real unsteady interaction between passages and is updated every time step at the expense of computational overhead. General Grid Interface (GGI) class of connections is applied to all the interfaces therefore allowing for node (Fig. 3.1b) and even flow physics mismatch between the two sides. Although order of magnitude of nodes per each mesh is comparable, the discretisation at both sides can vary, hence it is important to account for these geometry shortcomings. In CFX, it is up to "1/2 of the average depth of the elements touching the connection surface" [102]. Each interface has a specified pitch ratio based on the blade numbers obtained from zTurbo.

3.4. SOLVER CONTROL

The mesh density has been chosen based on mesh sensitivity study. For evaluation, Total Pressure Loss Coefficient based on eq. 2.7 is applied because it is readily obtainable from the cascade data. Further cascades contain blades of relatively similar size, hence the order of magnitude for node number remained the same. Root Mean Square (RMS), one of the main factors for convergence quality check is generally defined for the i-th element as follows:

$$|RMS| = \sqrt{\frac{1}{N} \cdot \sum_{i=1}^{N} (R_i)^2} \tag{3.4}$$

where N is the number of elements. The detailed treatment of the RMS definition can be found in [102]. Mesh independence study can be found in the appendix A. The Advection Scheme and Turbulence Numerics are both set to High Resolution (see more: [102]).

3.5. STEADY STATE

First part of the simulation phase is focused on steady state cases which ignore some of the so called cross terms and higher order terms dependent on time. Due to removed transient non-linearities steady state models often converge easier because of smaller amount of terms to model. It assumes a state that would have been achieved after a relatively long time interval and it can be used for problems that are not strongly unsteady. A fully converged steady state solution should be equivalent to the transient one. Time-scale size affects the convergence behaviour and any difficulties might indicate incorrect flow physics, erroneous time-scale estimation, numerical effect or a transient problem. If changing the time-scale does not affect the oscillation period, the flow is probably transient, otherwise a spurious behaviour can be often a numerical issue [102]. The unsteadiness level can be also done with Strouhal number analysis. Such effects can be damped and have been tried for this work by applying non-reflective BC. These however, are included in CFX as a beta feature and are still under development. Conducted array of simulations during mesh independence study showed that it works well with simple grids, which unfortunately proved mesh-sensitive, and hence unreliable.

Local time-scale can often provide a faster convergence, however, since the domain involves a variety of time-scales, this approach can be often insidious [11]. For this reason, simulations are performed with a physical time-scale based on the boundary conditions, flow physics and the geometry [102]. An algorithm has been implemented in CFX to establish this time-scale, which usually works flawlessly and provides a sound order of magnitude. Due to limited computational resources, the work has been divided to simulations performed on quasi 3D and 3D meshes. The time-scale for the first stage quasi 3D mixing-plane and frozen rotor simulations was: $\sim 4.85E-06s$ and approximately twice larger ($\sim 9.0E-06s$) for the remaining stages. For 3D cases, the time-scale could be even slightly larger, varying between $1.81E-05s$ and $1.97E-05s$ which usually contributes to faster convergence. For models with tip clearance, smaller time-scale of $2.2E-06s$ or even $2E-07s$ was needed. The simulation time of each case took approximately 24-72 hours on computer using processor Intel(R) Xeon(R) CPU E5-1620 v3 3.5 GHz and 64 GB of RAM.

3.6. TIP LEAKAGE AND CONVERGENCE

Creating tip leakage gaps requires introducing new interfaces in the meshes (see the general connection applied in Fig. 3.1b). Nodes have been connected by means GGI (for detailed treatment, see [102]). Shrouds in rotating domains have been extended further away from the hub by appropriate length equal to the respective leakage gap thickness (0.025, 0.05, 0.075 and 0.1 mm). The resulting cells have been subsequently subtracted only from the blade itself in the direction normal to the shroud resulting in the same flaring angle and blade height. This ensures domain augmented by the leakage gap without modifying the blade shape.

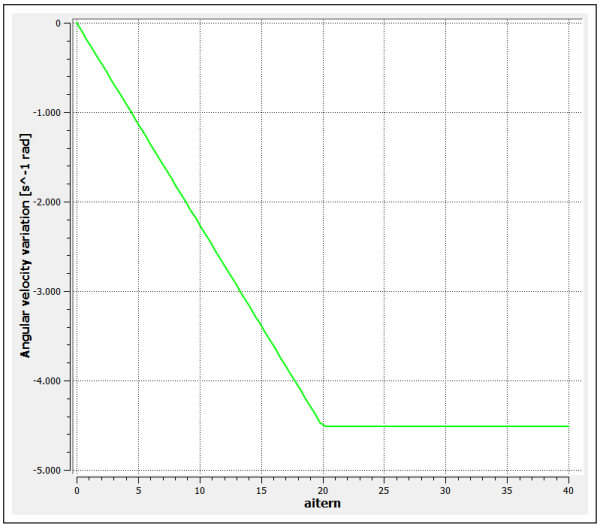

(a) Angular velocity variation for all tip clearance models

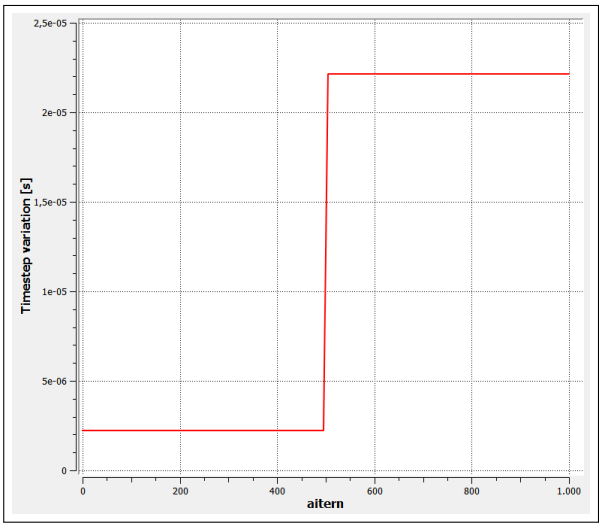

(b) Time-scale variation for 0.1 mm gap model

Figure 3.5: Handling convergence problems

The resulting leakage channel leads to convergence problems and overflow in the linear solver when automatic time-scale is used because variables such as Mach number or temperature go out of bounds. The problem requires careful time-scale selection to avoid the overflow. For this reason several measures have been applied

1. Firstly, shaft angular velocity is initially set to zero rev/min and gradually increases as the machine accelerates and reaches maximum after 20 iterations (see Fig. 3.5a).

2. Secondly, as seen in the Fig. 3.5b time-scale is initially possibly low and increases once convergence factors in a form of various performance parameters (see: 2.5.2) stabilise their oscillations. A sensitivity study was needed and for each leakage gap case, different iteration number was needed. E.g. for 0.1 mm gap in increase in time-scale was possible even after 500 iterations.

These measures are not necessarily paramount to reach convergence because a very small time-scale should at some point also lead to the solution, however, it helps to save a lot of time at the expense of a little more unsteady convergence, when possible. Also, with this approach static back-pressure has to also gradually change in a similar manner.

3.7. TRANSIENT STATE

For the transient simulation time-step is selected based on the angular velocity of the turbine and the number of blades in the given cascade. Passing period has been computed as follows:

$$T_{passing} = \frac{2 \cdot \pi}{\omega \cdot N} \tag{3.5}$$

where: ω is the angular velocity in radians and N the number of blades in the given blade row. This formula holds if the pitch ratio between the blade rows is equal to unity. Due to limited computational and memory resources, 6 passing periods have been chosen with 1600 times-steps per each passing period. This resulted in the time-step of 7.25193E-08 s. Maximum internal loop coefficients have been set-up to 30 and throughout the iteration they looped up to approximately 20 iterations per time-step, however, there were several cases (out of 9600) where these coefficients reached the maximum of 30 iterations. This suggests that the time-step could be still slightly smaller but arguably around this order of magnitude.

The simulation time took 13 days on computer using processor Intel(R) Xeon(R) CPU E5-1620 v3 3.5 GHz and 64 GB of RAM. To obtain more insight about the oscillations in the performance parameters, the number of passing periods should be also larger, however, the size of solution for each time-step takes around 240 MB thus 6 passing periods of a quasi-3D, 2-cell thick mesh takes 283 GB of data provided that only every 8-th time-step is saved on the hard-drive. A solution for every time-step for one full rotation cycle would take 4528 GB of data and as mentioned before this time-step could still be smaller. With the challenge of available memory resources, analysing further stages was not possible at this stage.

4

RESULTS AND DISCUSSION

4.1. EFFICIENCY

Performance has been evaluated for various tip clearance gaps normalised to the average height of the first rotor (R1), see table 4.1. Tip clearance has been imposed only on rotors whereas stators are assumed fixed (see: Chapter 2). Configuration defined in zTurbo contains 0.1 mm gap for both rotors and stators.

Table 4.1: Tip clearance normalisation

Tip clearace gap	Normalised to R1
0.000 mm	0.00 %
0.025 mm	0.82 %
0.050 mm	1.64 %
0.075 mm	2.46 %
0.100 mm	3.28 %

As expected, total-to-static efficiency of the turbine decreases with the increase in tip clearance gap, see Fig. 4.1a. Data from the zTurbo is obtained only for one case, namely with 0.1 mm gap. For this value total-to-static efficiency of the machine obtained by CFD is 65.3% whereas for zTurbo, it is 63.1%.

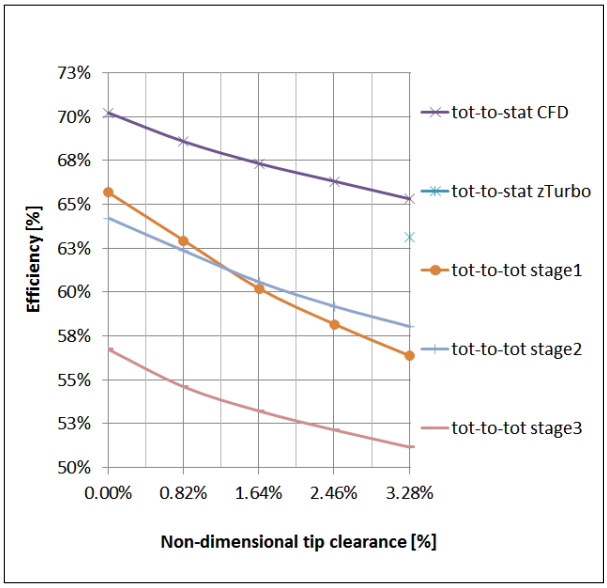

(a) Tot-to-static and tot-to-total efficiency w.r.t. tip clearance

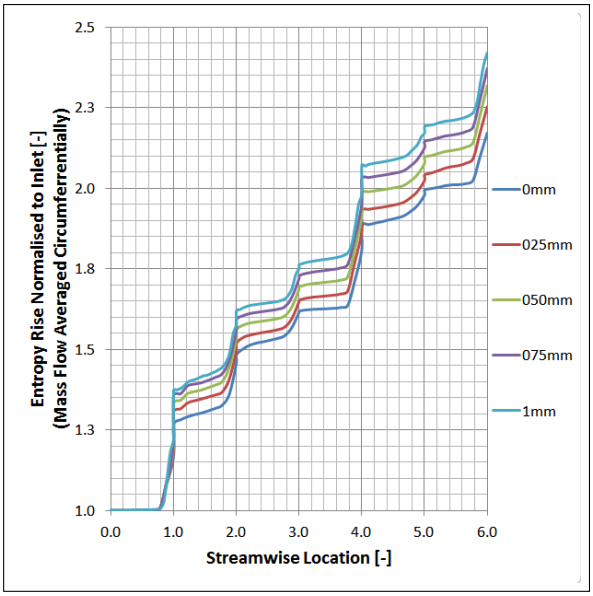

(b) Stream-wise entropy rise for various tip clearance gaps

Figure 4.1: Efficiency and irreversibility for steady-state simulations

Total-to-static efficiency obtained by CFD is expected to be lower if clearance gap will be applied to stationary domains as well, however, this 2.2% discrepancy suggests a good coherence with the mean-line design. As expected, obtained trend in the Fig. 4.1b suggests that increasing the clearance between the blades and the casing introduces entropy generation in the machine. From the same figure, it also becomes apparent that the largest irreversibility generation occurs in the Stator 1, Rotor 2 and Rotor 3, hence these blades require optimisation. Fig. 4.1a shows that the poorest performance is for Stage 3 which for 3.28% gap exhibits total-to-total efficiency by 5% lower w.r.t. Stage1. Further analysis in this chapter shows, that this is a result of a badly chosen stagger angle and blade profile shape for Rotor 3 also seen in Fig. 4.7b. Fig. 4.1a also shows that Stage 1 is more sensitive to tip clearance gap than other stages and although for 0 mm clearance it performs better than Stage 2, for 3.28% gap its total-to-total efficiency is lower. This might be due to the interference between secondary flows and the tip leakage vortex. For larger leakage gaps, tip leakage vortex (see Fig. 4.6b) is bigger w.r.t. cases featuring smaller clearances (see Fig. 4.6a). Also, blades in Stage 1 are characterised by smaller aspect ratio w.r.t. Stage 2. As a result, tip leakage vortex is closer to the secondary vortices resulting in stronger interaction, enhanced mixing and entropy generation.

4.2. TRANSIENT RESULTS

As mentioned in chapter 3, unsteady simulation was only possible for the first stage, Quasi-3D mesh with 2 cells in the span-wise direction. Notably, as seen in the table 4.2, total-to-static efficiency of the stage is by 3% higher than that of 3D steady-state case obtained for zero clearance gap (see: Fig. 4.1a). To make unsteady results comparable with the steady-state cases, transient oscillations are averaged over the entire iteration period (as an example, see Fig. B.1b).

Table 4.2: Transient results

Variable	**Value**	**Unit**
Total-to-static efficiency	53	[%]
Tot. Press. Loss. Coeff. S1	23	[%]
Tot. Press. Loss. Coeff. R1	28	[%]

In the Fig. 4.2a, a clear increase in entropy occurs close to the blade profile, behind the shock-wave. Fig. 4.2b shows more detailed pattern of this phenomenon with the strong temperature gradient in the throat section. High entropy wake spills over the leading edge of the subsequent rotor cascade.

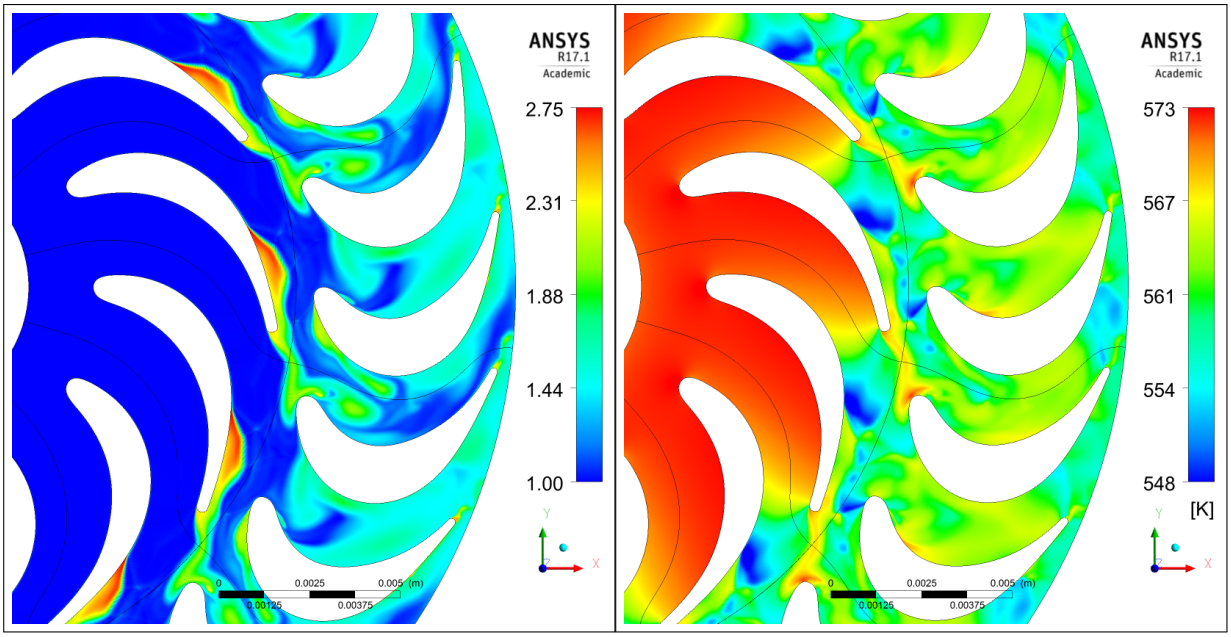

(a) Entropy normalised to inlet [-]

(b) Static temperature in K

Figure 4.2: Transient results on the blade-to-blade plane at mid-span location

Even if local Mach numbers are high, according to [18] oblique shocks generate little direct loss. The largest consequence is when the shock is close to the trailing edge. Low base pressure just behind the trailing edge causes the flow to expand around this trailing edge towards low pressure region which is subsequently re-compressed by a shock wave. Fig. 4.3a shows that this shock is rather oblique and further away from the trailing edge and as seen in Fig. 4.3a the resulting wake decreases towards this trailing edge.

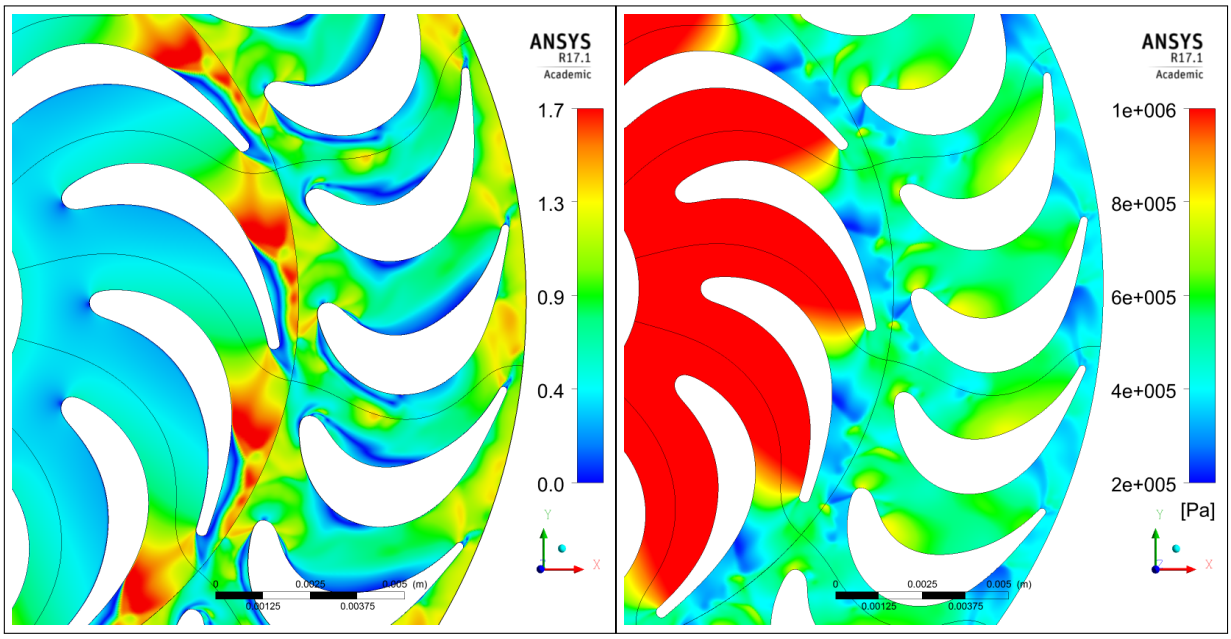

(a) Relative Mach Number (b) Static pressure in [Pa]

Figure 4.3: Transient results on the blade-to-blade plane at mid-span location

Video animation of the flow showed how trailing edge wake of the stator interferes with the shock-wave forming at the rotor leading edge. Obtained animation together with figures 4.2a and 4.2b show that the unsteadiness of the flow is large. Figures 4.4a and 4.4b show the change in the curl of the velocity vector leading to separation in the rotor.

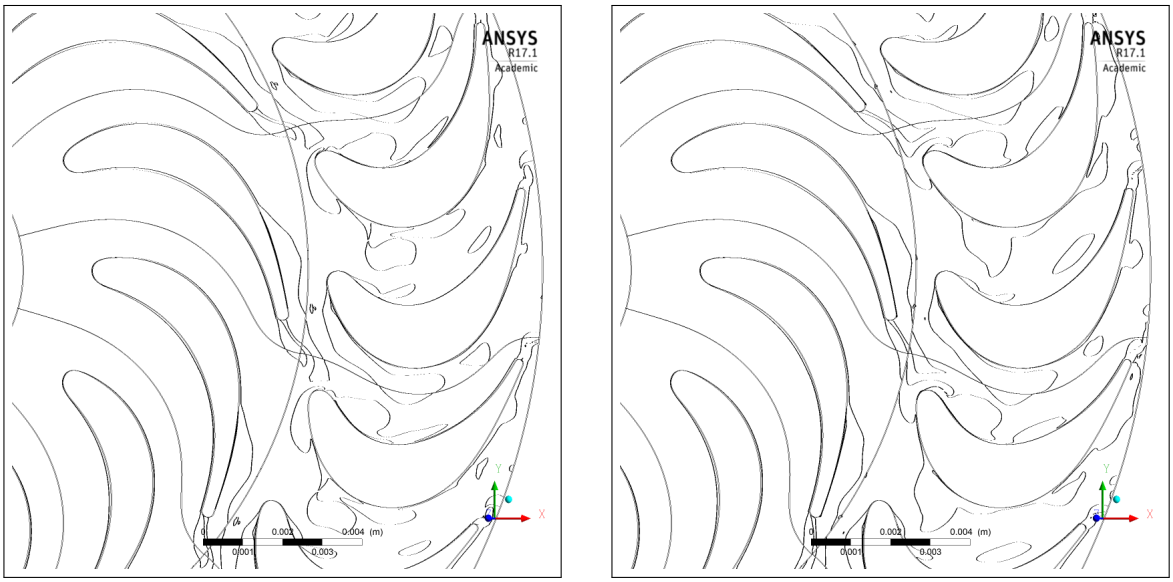

(a) Time-step 7800 (b) Time-step 9400

Figure 4.4: Vortex core region for vorticity level of 0.05%.

Quasi-3D simulation does not include the flaring angle which entails span-wise velocity components but it allows to capture phenomena which are dominated by 2D effects, such as profile losses. Figures 4.5a and 4.5c show a very different streamlines pattern. It is apparent that the BL (especially leading edge) of the rotor is affected by the flow coming from the stator which changes the incidence angle at inlet the rotor.

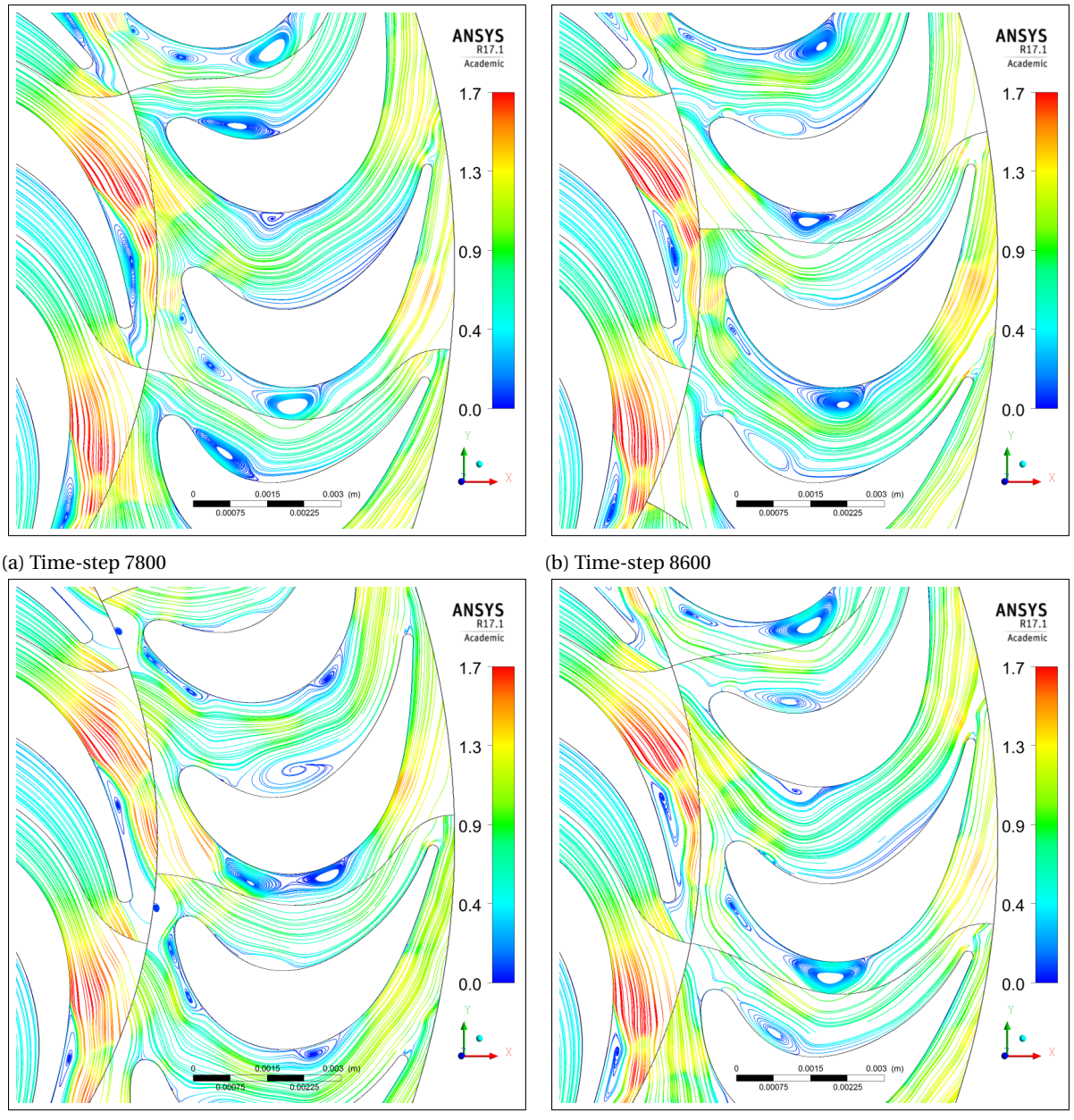

(a) Time-step 7800

(b) Time-step 8600

(c) Time-step 9000

(d) Time-step 9400

Figure 4.5: Streamlines and Relative Mach Number at mid-span. A change in the incidence angle on Rotor 1.

As a result, for the same solidity, velocity triangles change and different flow deflection results in modified aerodynamic load and extracted work. As mentioned in chapter 2, mini-ORC turbines are likely to be exposed to off-design conditions and blade design has to account for it (e.g. leading edge thickness). Stator shock wave, impinging on the rotor might lead to thickening its BL and making more prone to separation. Expansion in the initial part of the Stator 1 is rather smooth due to the gradual rise of the curvature in the initial stream-wise locations. This curvature increases in the aft part of the airfoil leading to larger accelerations. As mentioned earlier, shock entropy generation exerts rather small effect on the profile losses which are dominated by BL and wake mixing losses (see: 4.2a). Quantitative prediction of entropy generated by the shock

can be found in [18]. At this design stage, pitch ratio between S1 and R1 cascades is 0.5. This might result in frequency oscillations and hence large vibrations leading to fatigue. Smaller temperature changes (of ~50°C) peculiar for ORC yield the ability to use cheaper materials w.r.t. steam turbines which can be disadvantaged if such effect is not accounted for in the mechanical design.

4.3. STEADY STATE RESULTS

Table 4.3 presents selected steady state results and it becomes apparent that for Stator 1, total pressure loss coefficient arrives at the same value as in transient case. Steady state, 3D result for Rotor 1 is by 3% higher probably due to the presence of secondary flows which for Rotor 1 are more critical w.r.t. Stator 1 as the endwall BL thickens along the machine [66] and which are not present in the quasi-3D simulation. BL at the inlet of Stator 1 is relatively undisturbed whereas leading edge of the Rotor 1 experiences the wake, corner and passage vortices originating from Stator 1 (see also Fig. 4.11a).

Table 4.3: Steady state results for Stage 1. No tip clearance and no-slip condition at the endwalls

Variable	**Value**	**Unit**
Total-to-static efficiency	50	[%]
Total Pressure Loss Coeff. S1	23	[%]
Total Pressure Loss Coeff. R1	31	[%]

Another feature is the interference between tip leakage vortex and the separation bubbles (see figures 4.6a and 4.6b) on the suction side as a result of adverse pressure gradients and super-velocities due to curvature. This also enhances mixing and hence, entropy generation within the passage.

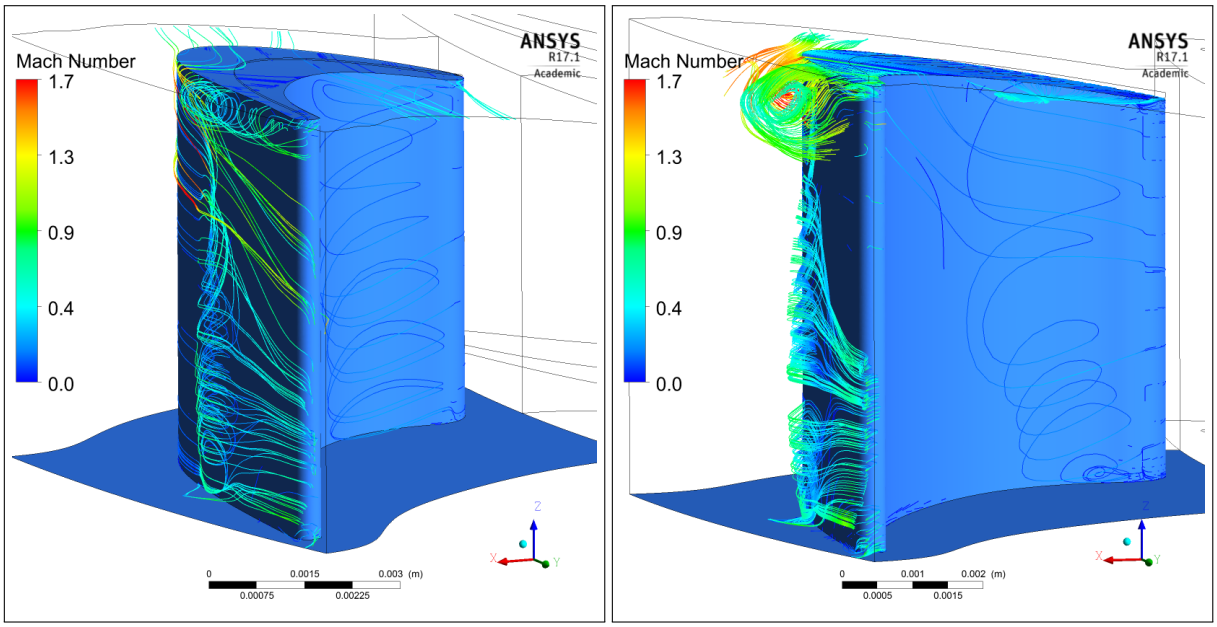

(a) Rotor 3, 0.025 mm gap

(b) Rotor 3, 0.1 mm gap

Figure 4.6: Tip leakage under-turning vortex causing enhanced mixing and work reduction.

In small-scale machines the interaction between leakage flow with the passage vortex is stronger compared to large power plants. This can be also shown more qualitatively on the contour maps in the Fig. 4.7a. Fig. 4.10a shows that the flow enters the leakage gap from the blade pressure side, then subsequently separates from the blade tip and forms a "jet" [18]. From Fig. 4.10a and 2.12b it can be seen that the radius of the pressure surface corner affects this separation. According to [18] the majority of the mixing occurs close to the suction surface but this mixing will continue through the next blade rows and therefore, as seen in the transient results, it is challenging to separate those losses. It does not only enhance mixing but it also deflects the flow in the different direction (an under-turning) causing a reduction of extracted work. This has been visualised in the Fig. 4.9a and 4.6b. Although the phenomena is located at the tip of the blade, changed mass-

flow affects lift generation over the span. According to [18] this lift reduction is primarily inviscid and hence not necessarily associated with a loss of efficiency. Decreased mass-flow over the passage contributes to a small decrease in blade loading for a given cascade (see: Fig. 4.10b). In mini-ORC turbines, blade thickness is relatively small and the scenario shown in Fig. 2.12b might be arguably more likely than the one in Fig. 2.12a. The jet does not mix-out within the gap if the blade thickness is "more than about four times the tip gap" [18]. The velocity chord-wise can affect the corner bubble region. It convects the fluid, which has low energy towards the point where the pressure is minimum in the leakage gap. As discussed in chapter 2 and shown in [13], optimal blade chord for discussed mini-ORC turbine featured largest chords in the last stage. This results in lower ratio between the tip gap and the chord for these stages and possibly larger region of influence, however, the mass-flow is very small and according to [18], "likely to be insignificant". In turbines, the relative motion between the casing and the blade tip acts to reduce the leakage flow [18]. This implies an advantage for ROT because this phenomena can be to some extent decreased towards the outlet as the peripheral velocity increases.

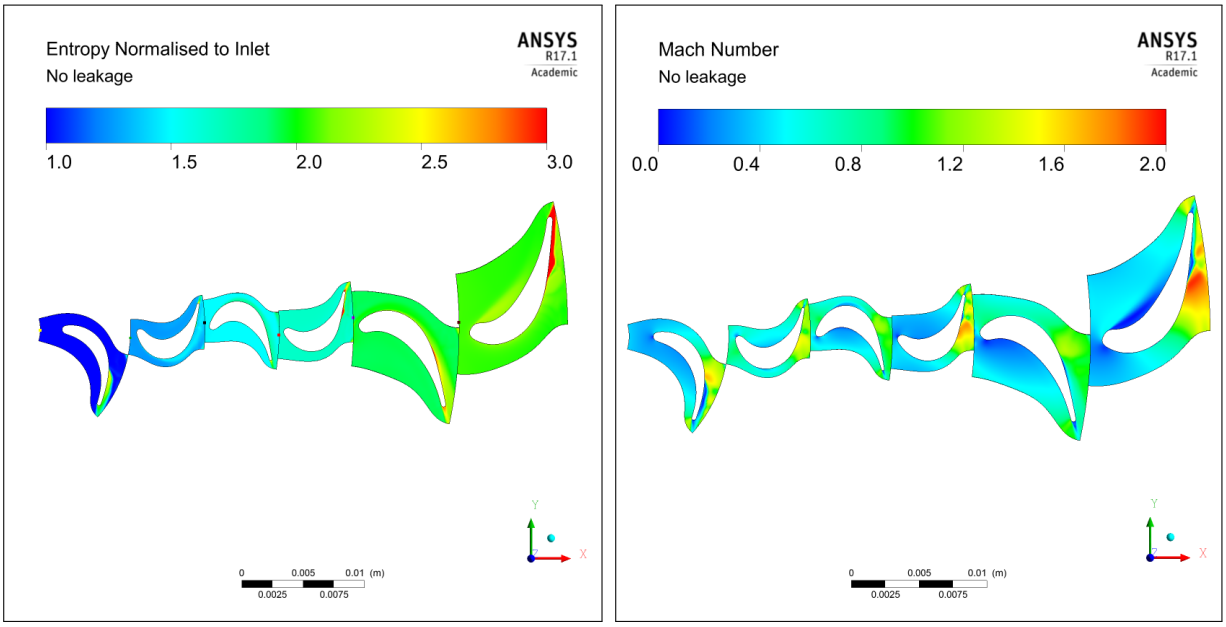

(a) Entropy normalised to Stator 1 inlet

(b) Relative Mach Number

Figure 4.7: Blade-to-blade plane for the case without tip clearance located at 2 mm height from the hub in the span-wise direction

An important issue related to the mixing-plane assumption entails entropy discontinuity at each interface between domains in the Fig. 4.16a and 4.16b. This discrepancy is imposed by the solver upfront and the user cannot influence it. It is related to the assumption of physical mixing due to relative motion between components. It assumes that this phenomenon is sufficiently large to cause any upstream velocity profile to mix out prior to entering downstream blades. In the real case flow will never be entirely mixed at this stage. It is important to carve this assumption in mind as it has an impact on the results. It can be also seen that this discontinuity is the largest at the first interface between the Stator 1 and Rotor 1, a stage which is paramount for small-scale machines due to large load and challenging fluid-dynamic design. Fig. 4.7b features un-physical spots in the contour map which are a result of using mixing-plane approach and resulting circumferential averaging of fluxes through bands on the interface [102]. It accounts for time average interaction effects, but neglects transient interaction. The flow in the Fig. 4.7b exhibits a shock wave in close proximity to the resulting low pressure wake and both these phenomena encounter stage interface between the domains. As a result of strong variation in quantities and little stage gap this results in un-physical pattern. Similarly for Rotor 1, Rotor 2 and Rotor 3 which feature regions of large acceleration in the vicinity of domain boundary. It has to be noted that performance parameters such as total pressure loss, entropy loss or kinetic energy loss coefficients or efficiencies are evaluated on the domain boundaries, not e.g. at the leading edge of the downstream component as in [66]. In the latter case, also the entropy production within the entire stage radial gap is included.

Fig. 4.8b shows that stagger angle in the Stator 3 could be probably also improved. The incidence angle obtained by CFD for Stator 3 is by 2 [deg] larger than the one predicted with the mean-line code. This leads to larger flow deflection which for the same blade solidity ramps up the eulerian work. On the other hand, in Rotor 3 the flow deflection is noticeably lower leading to large separation region at the pressure side and poor performance. As seen in the Fig. 4.6a, the resulting vortex continues towards lower pressure region. It interferes with the free-stream flow and the secondary flow structures (see, e.g.: 4.11b) leading to enhanced mixing and entropy generation. The incidence angle in the first four cascades (see: both Fig. 4.8a and 4.8b) seems to be well predicted with the mean-line design tool zTurbo.

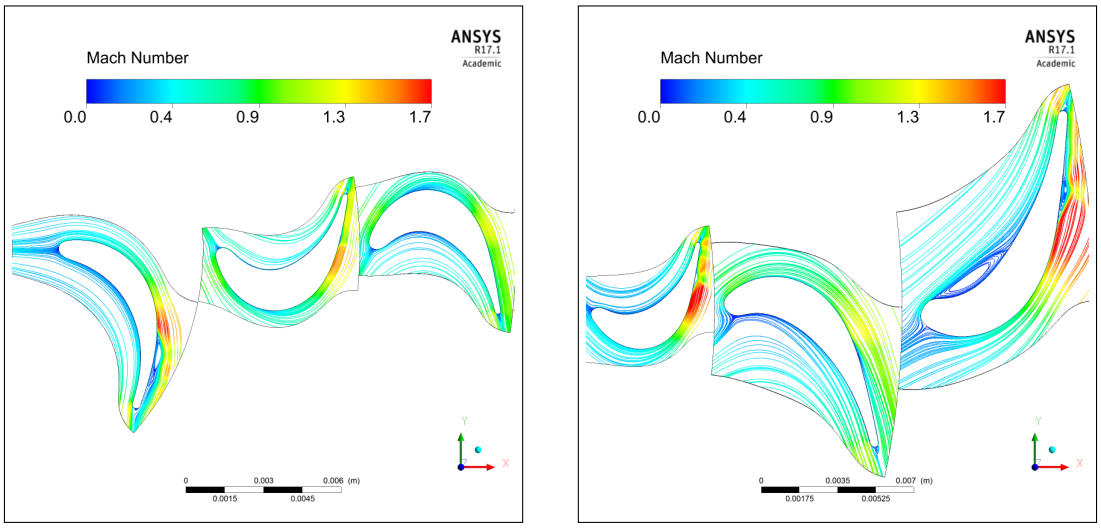

(a) From the left: Stator 1, Rotor 1 and Stator 2

(b) From the left: Rotor 2, Stator 3 and Rotor 3

Figure 4.8: Pseudo streamlines based on time-averaged velocity. Located at 2 mm height from the hub in the span-wise direction

Fig. 4.9a shows entropy generation in the plane located at mid-span of each leakage channels. For stators the off-set is the same, of 0.05 mm from the shrouds. In Fig. 4.9a, Rotor 1, does not feature strong entropy generation spots in both pressure and suction side on the blade. Analysing each cascade separately shows larger entropy gradients, which vanish in comparison with large loss regions, such as in the Rotor 3.

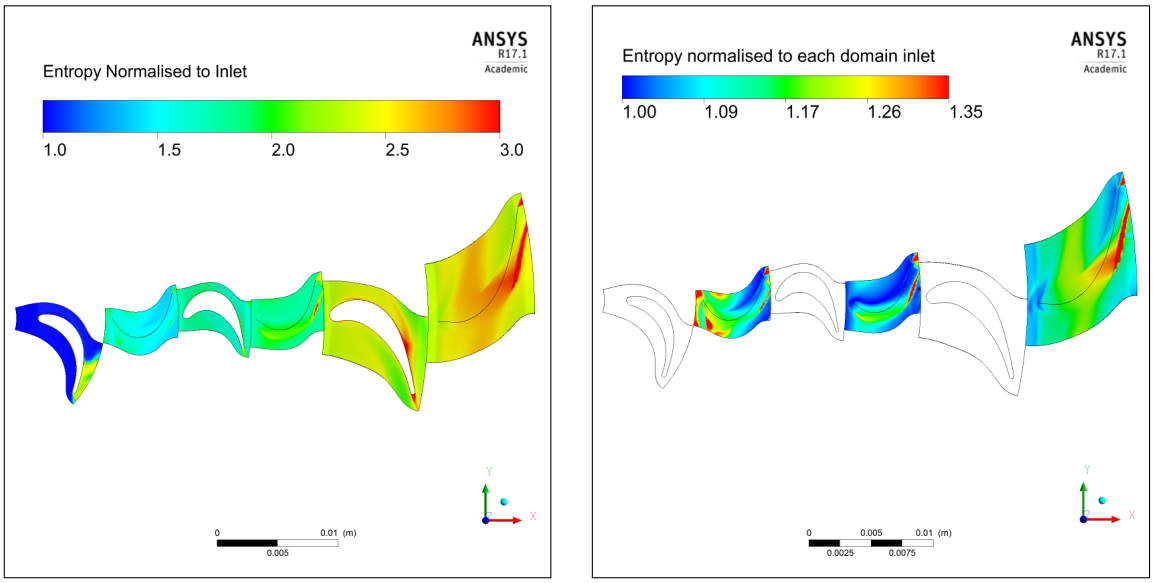

(a) Entropy normalised to Stator 1 inlet

(b) Entropy norm. to respective domain inlets

Figure 4.9: Tip leakage effect on the flow-field for 0.1 mm leakage gap, blade-to-blade view

What is not seen in the Fig. 4.7a and can be noted in the Fig. 4.9a is the entropy generation occurring already in the leakage channel, where mixing starts to occur. Mini-ORC machines, as mentioned earlier, feature relatively thin blades. Whereas for thin blades large entropy creation does not occur directly above the tip, for thicker blades, such as R3 it prominently occurs within this section due to stronger mixing (see Fig. 4.9b).

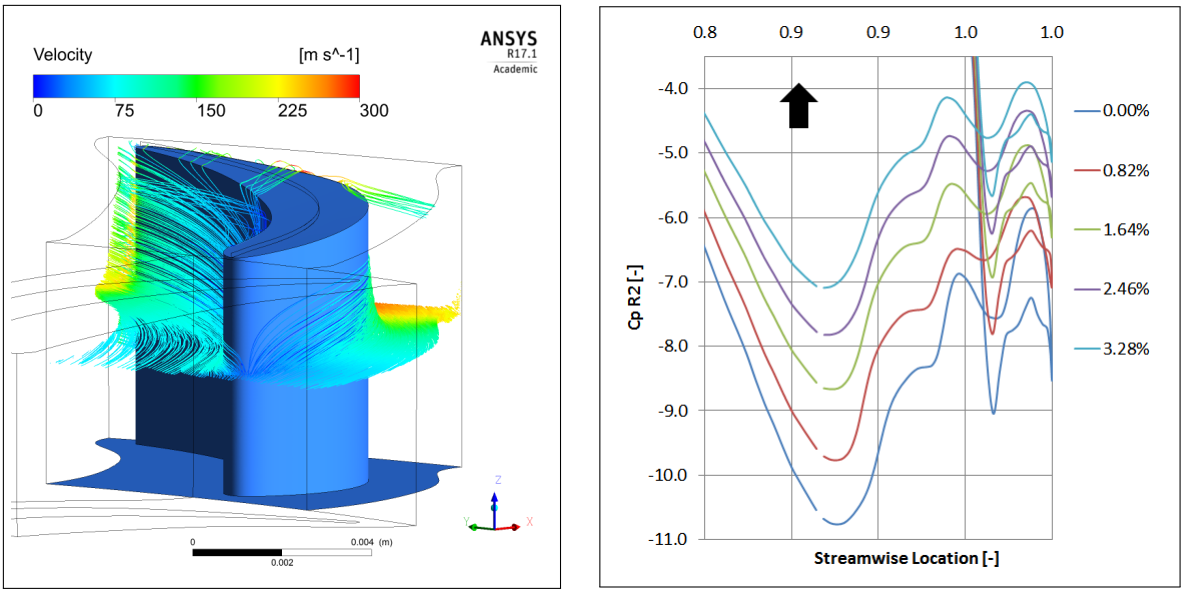

(a) Tip leakage cross-flow in the Rotor 3 corresponding to entropy rise in the Fig. 4.9a

(b) Blade loading reduction on Rotor 2 due to tip leakage and reduced mass-flow over the passage

Figure 4.10: Tip leakage and cross-flow effect on the blade loading

As expected, Fig. 4.11b shows stronger secondary flows for Rotor 3 compared to Stator 1 (see Fig. 4.11a) where the inlet flow is practically undisturbed and the flaring angle smaller than for Rotor 3. Due to one of the major advantages of ROT configuration in a form of naturally growing passage area along the radius, flaring angles can be smaller which results in smaller span-wise velocity components contributing to secondary flow-fields w.r.t. axial machines.

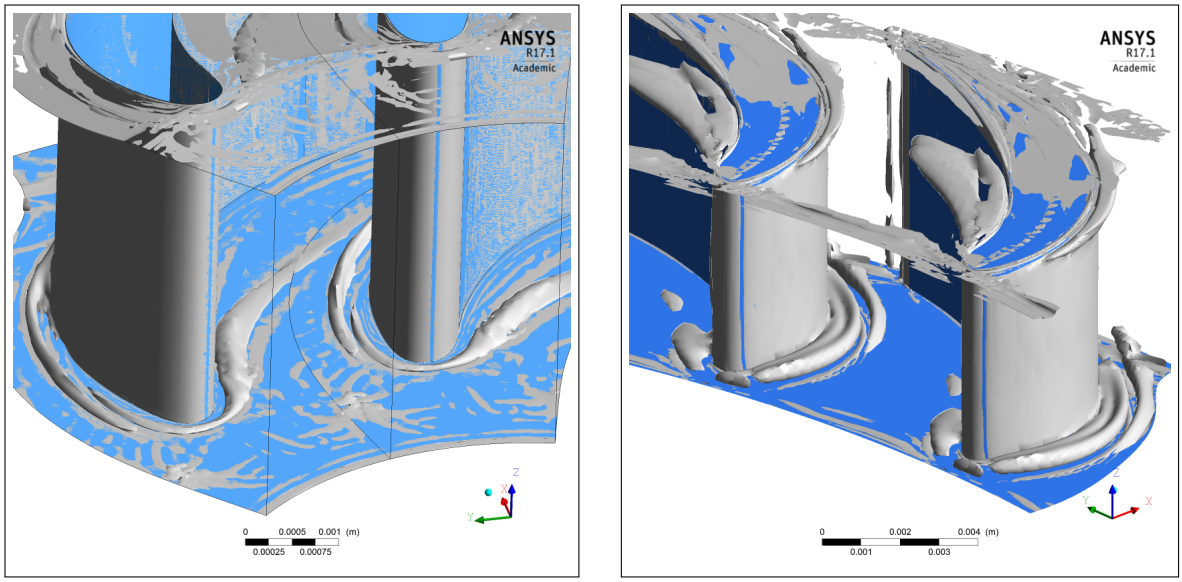

(a) Stator 1

(b) Rotor 3

Figure 4.11: Secondary flow, horse-shoe and passage vortices. Lambda 2 criterion with intensity level of: 0.003%.

Small aspect ratio in mini-ORC and disturbances from the previous cascades lead to onset of 3D effects. To better investigate the flow behaviour in the vicinity of the endwalls, and specifically, to distinguish between the inviscid effects of flaring angle from the viscous phenomena linked to secondary flows, two types of 3D simulations without tip clearance are used with the following discrepancies:

1. 3D with free-slip boundary condition on hubs and shrouds and no-slip condition at the blade surfaces
2. 3D with no-slip conditions and hubs, shrouds and blade surfaces.

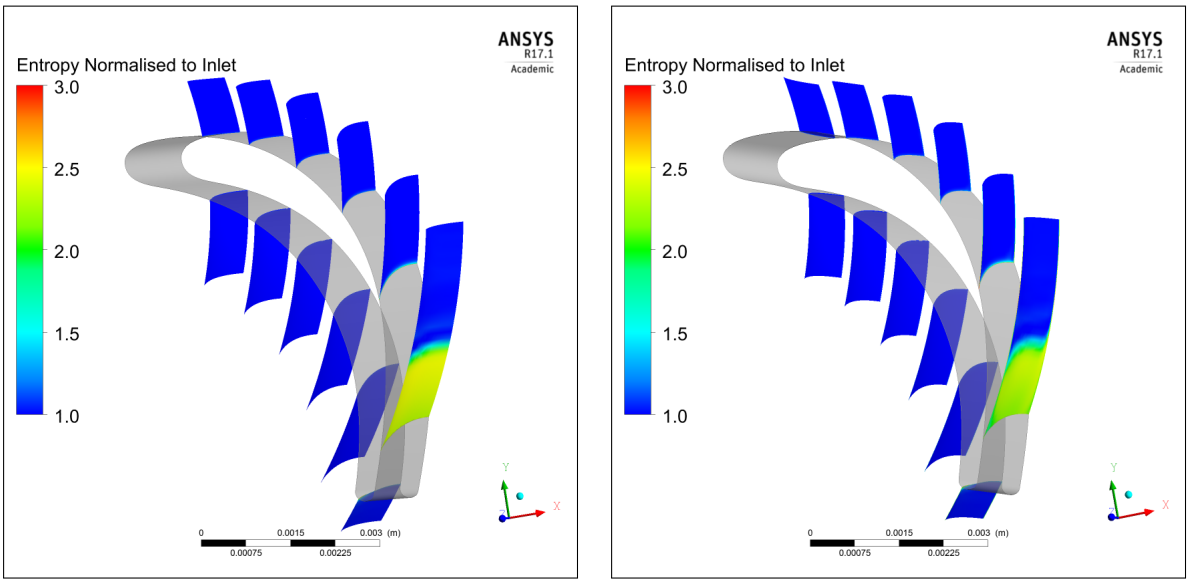

(a) Free-slip (b) No-slip

Figure 4.12: Entropy rise over mini-ORC ROT for Stator 1

According to [66], the first approach allows to simulate the generation of secondary flows , which strongly depend on the endwall BL vorticity. Fig. 4.13a and Fig. 4.13b and also Fig. 4.15a and Fig. 4.15b illustrate these results.

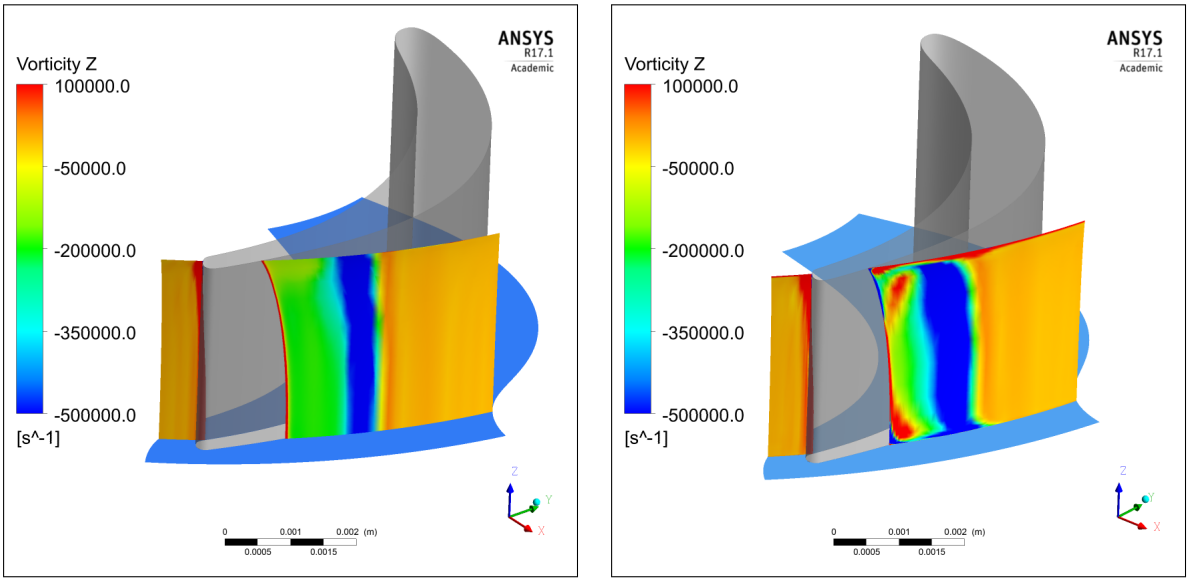

(a) Free-slip (b) No-slip

Figure 4.13: Vorticity for mini-ORC ROT for Stator 1

It becomes apparent that in the free-slip cases, the main source of entropy generation is the wake, which is approximately uniform along the span except endwall regions, possibly due to small change in blade load as in [66]. It can be concluded that flaring itself does not entail significant 3D loss mechanisms. In the no-slip model, losses in the wake are amplified by the secondary effects but it is not directly clear from Fig. 4.12b. Interestingly, it can be seen, that entropy generation in the no-slip case is even slightly smaller. Expectedly, entropy generation rises at the endwalls for no-slip case but further away from the wall this entropy generation is slightly smaller. Mesh sensitivity should not be the case, therefore the effect can occur due to 3D phenomena. As explained, the aspect ratio is small therefore deceleration at the endwalls might affect the flow at the mid-span stronger than in conventional machines. This might not necessarily be sufficient and it is difficult to support this argument without analysing larger amount of configurations. The positive vorticity field in the Fig. 4.13b w.r.t. Fig. 4.13a represents the passage vortex, which meets with the surrounding negative vorticity. According to [66], this kind of structure occurring behind the trailing edge is called Vortex Sheet and affects the flow angle.

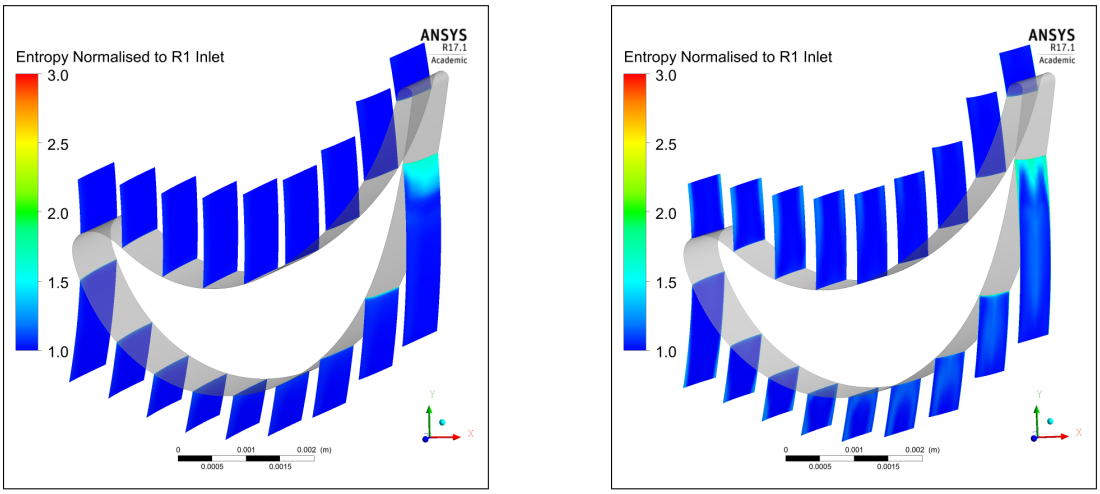

(a) Free-slip (b) No-slip

Figure 4.14: Entropy rise over mini-ORC ROT for Rotor 1.

Inertial forces in rotating domains affect the flow field in centrifugal turbines. In the mini-ORC ROT at hand, Coriolis and centrifugal forces modify the flow field on the blade-to-blade planes resulting in changes in aerodynamics and the extracted work. In ROT, variation of centrifugal force affects the profile losses but not the span-wise flow [66] which affects the strength of the shock-wave (see e.g. Fig. 4.3a).
Importantly, Coriolis force acts on the blade surface and deflects flow in the tangential direction, thus further deflects the flow. This provides negative contribution to the rotor blade deviation and ramps up the work exchange. It acts in the opposite direction w.r.t. the rotor velocity. Even small deflection of the flow angle is significant because the flow in the aft part of the blade is strongly tangential.

Table 4.4 shows the discrepancies in exit flow angles for both stators and rotors. It can be seen that for Rotor 1 and Rotor 2, small increase in tangential deflection occurs contributing to work exchange. Conversely, in the Stator 2 and Stator 3, a reduction in the deflection occurs. These features are coherent with the results proposed in [66] where ROT has been investigated. What does not align with these trends is Stator 1 and Rotor 3. This boils down back to the entropy discrepancy in the Stator 1 but no such discrepancy occurs in the Rotor 3. It can be the case that as mentioned before, domain boundary is close to the blade and the wakes in both cases affect mass-flow averaging the results of the angles of the velocity vectors.

Table 4.4: Exit mass-flow averaged flow angles in degrees at the domain boundaries

Domain	**Free-slip**	**No-slip**	**Domain**	**Free-slip**	**No-slip**	**Domain**	**Free-slip**	**No-slip**
S1	58.6315	65.8943	**S2**	74.7426	74.5548	**S3**	70.8545	70.2495
R1	-70.4416	-70.5946	**R2**	-65.3032	-65.5873	**R3**	-62.7868	-62.5629

Coriolis force depends on the magnitude of the relative velocity. Therefore, within the BL, its value is smaller

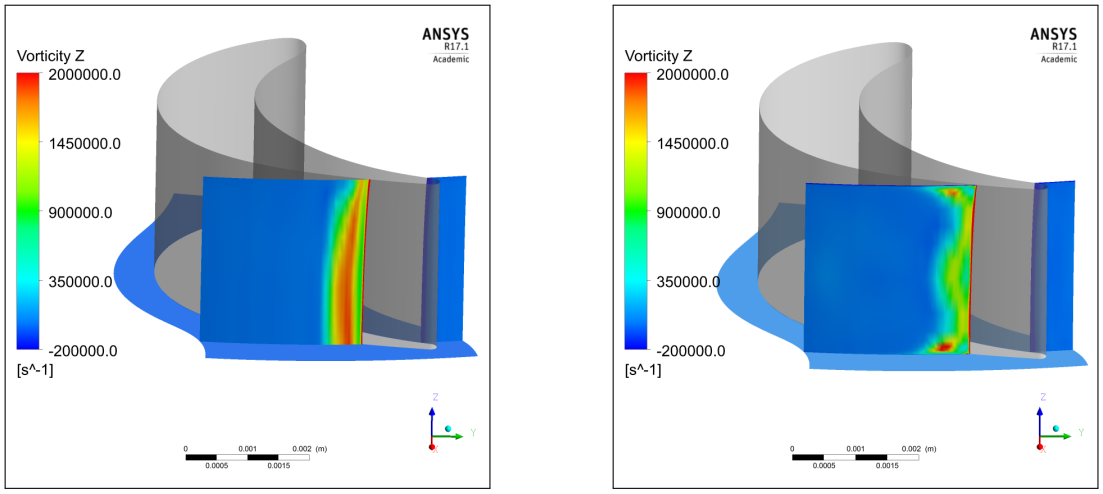

(a) Free-slip

(b) No-slip

Figure 4.15: Vorticity over mini-ORC ROT for Rotor 1.

w.r.t. free-stream and does not create significant impact on the cross-flow. However, further away from the wall, it deflects the flow tangentially and alleviates the secondary flows. It can be also seen (Fig. 4.13b and 4.15b), that the passage vortices at the shrouds are in both cases smaller than the ones at the hubs. The only difference between these cases is the presence of the flaring angle which probably, due to slightly reduced blade load leads to smaller vortex.

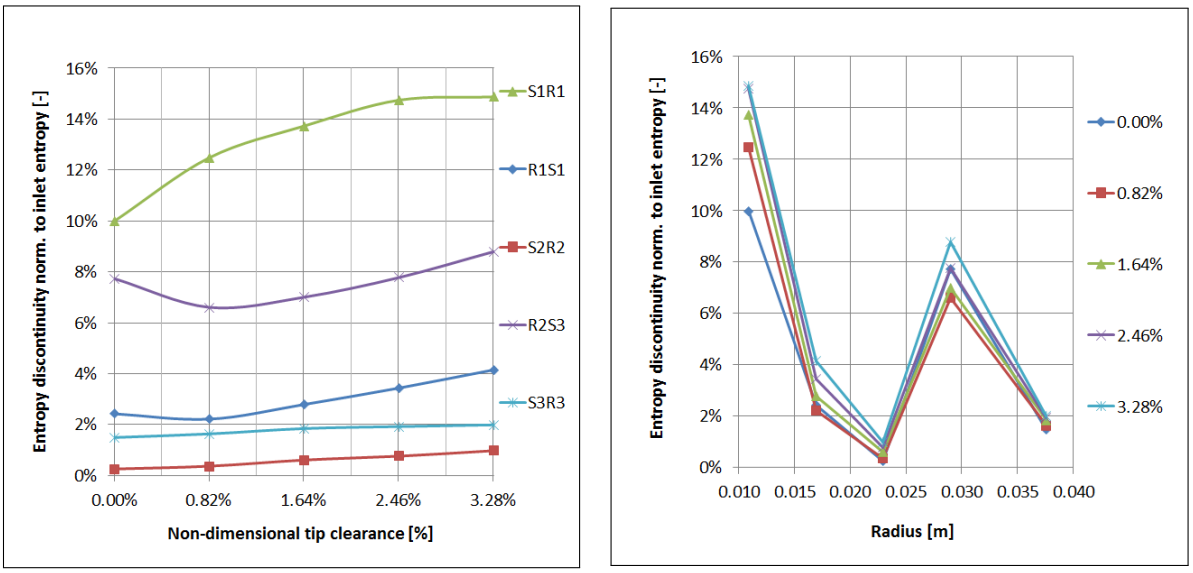

(a) Entropy discontinuity at mixing planes normalised to entropy at the inlet w.r.t. tip clearance

(b) Entropy discontinuity at mixing planes normalised to entropy at the inlet w.r.t. radial position

Figure 4.16: Entropy discontinuity at mixing plane interfaces

Another issue is the over- or under-estimation of losses due to using turbulent BL assumption in RANS. This has been treated by J. D. Denton [18] where the dissipation coefficient has been evaluated w.r.t. Re based on the momentum thickness. Fig. 4.17b has been created for the case without tip-clearance and corresponding to Fig. 4.17a it can be seen that with using RANS an over-estimation of losses occurs for all the domains. This momentum thickness has been evaluated based on the following equation:

$$Re_\theta = \int_0^\infty \frac{u}{U} \cdot (1 - \frac{u}{U}) dy \tag{4.1}$$

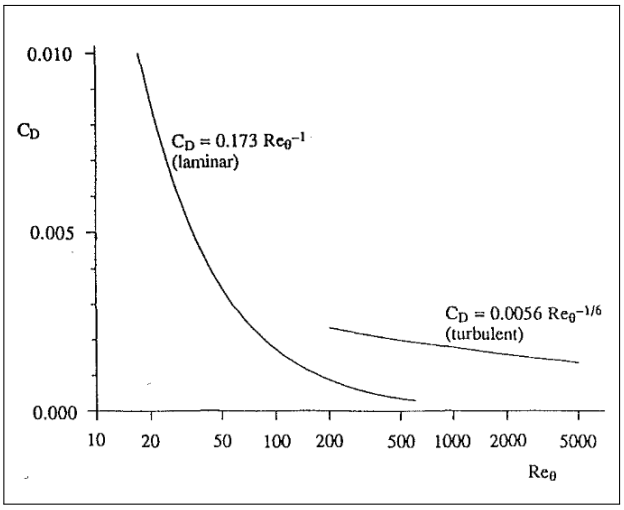

(a) Dissipation coeff. for laminar and turbulent BL [18]

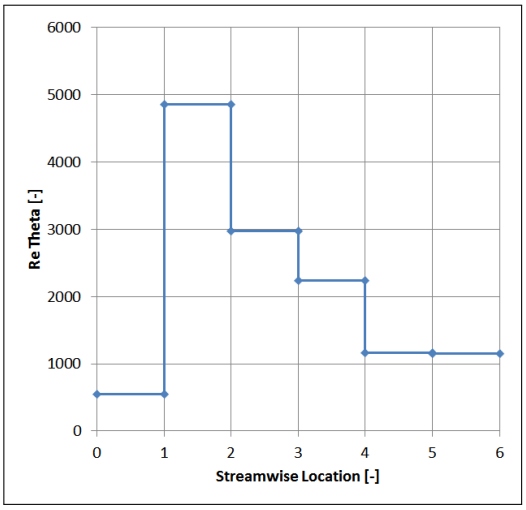

(b) Re aver based on the momentum thickness

Figure 4.17: Entropy discontinuity at mixing plane interfaces

where: u is the velocity within the BL and U is the free-stream velocity. Reynolds Number has been computed using volume-averaged velocity, not the maximum velocity in the domain as in Fig. 4.18a, and hence is more conservative. In the Fig. 4.18a it can be seen that tip clearance does not have a significant effect on the Reynolds Number, hence the Reynolds Number based on the momentum thickness is also expected to remain of similar order of magnitude. It has to be noted that according to loss estimation covered by [98] and [99] BL thickness is evaluated at the inlet of each domain and in the vicinity of the blade, but it can vary between the cases in terms of Theta angle (see more about Turboline in [102]) and hence affect the thickness value. The exact line definitions along which these calculations are performed can be seen in the Fig. 4.18b. It is cumbersome to select exactly the same position w.r.t. blade and additionally, boundary layers developed in previous domains are affected by the mixing-plane assumption. BL profiles at the inlet of the domains can be found in Appendix C.

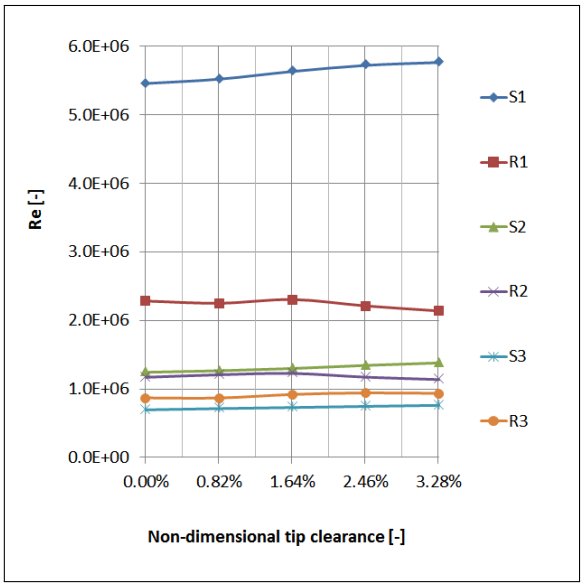

(a) Re dependance on the tip clearance

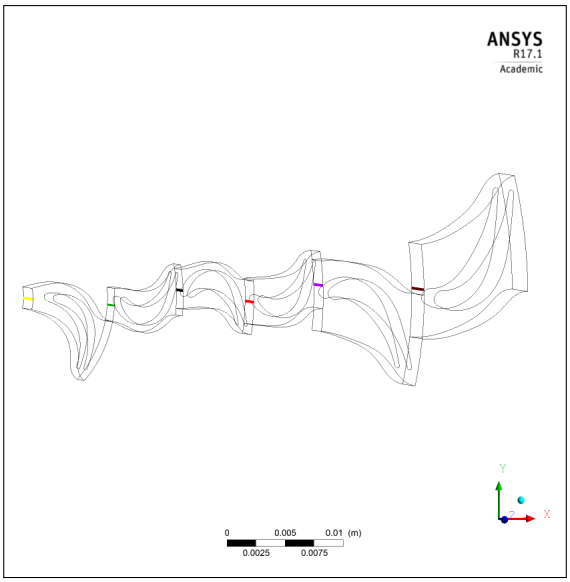

(b) BL evaluation location

Figure 4.18: Entropy discontinuity at mixing plane interfaces

4.4. LOSS BREAKDOWN

Many performance parameters have been checked to evaluate loss mechanisms in the small-scale radial outflow ORC machine configuration (see section: 2.5.1) but due to the fact that these empirical models were based on conventional machines and due to numerical assumptions in this work, some of them led to unphysical secondary-loss or tip leakage estimation. E.g. applying entropy loss coefficient (see eq. 2.9) in conventional approach (see [98]), as foreseen by Benner resulted in larger value for domains with free-slip conditions at hubs and shrouds compared to no-slip condition cases where shearing occurs. The presence of the BL slightly decreases the cross section of the passage leading to higher free-stream velocities and a stronger shock but this again, is not directly clear from the Fig. 4.12b.

Loss breakdown treated by M. W. Benner [98][99] based on total pressure loss coefficient proved to be the most physical amongst the obtained results, even though criticised in [100]. A non-physical negative tip leakage loss occurred for small clearance gaps (see: Fig. 4.19) but it reaches a physical value for 0.1mm gap. It is suspected that this tip leakage trend can be positive if stationary domains will also have clearance gap imposed as it was done in mean-line tool zTurbo.

According to the new model proposed by Benner [98] and [99] and discussed in Chapter 2.5.1, for e.g. Stator 1 we have boundary layer displacement thickness as a result of trapezoidal integration rule:

$$\delta^* = \int_0^{\delta} (1 - V/V_e)\,dz = \int_0^{5.39E-04[m]} (1 - V/57.29[m/s])\,dz = 7.32E-06[m] \tag{4.2}$$

Inlet BL profile for this domain can be seen in Fig. C.1a. The mean vector angle through the airfoil row is obtained with using "Velocity Flow Angle" function in CFX and can be expressed as:

$$\tan\,\alpha_m = \frac{1}{2}(\tan\,\alpha_1 + \tan\,\alpha_2) = \frac{1}{2}(\tan\,(0[^\circ]) + \tan\,(-65.9[^\circ])) = -1.1[-] \tag{4.3}$$

Signs of the angles pertain to the convention described by Benner [98]. Computing arcus tangens of the expression above gives:

$$\alpha_m = \arctan\,(-1.1) = -48[^\circ] \tag{4.4}$$

Tangential loading parameter F_t yields:

$$F_t = 2(\frac{S}{Cx})\cos^2\alpha_m(\tan\,\alpha_1 - \tan\,\alpha_2) = 2(\frac{3.05E-03[m]}{2.96E-03[m]})\cos^2(-48[^\circ])(\tan\,(0[^\circ]) - \tan\,(-65.9[^\circ])) = 2.05[-] \tag{4.5}$$

The key variable - penetration depth, is expressed as:

$$Z_{TE} = h\cdot(\frac{0.1\cdot F_t^{0.79}}{\sqrt{CR}\cdot(\frac{h}{c})^{0.55}} + 32.7(\frac{\delta^*}{h})^2) = \tag{4.6}$$

$$= 3.56E-03[m]\cdot(\frac{0.1\cdot 2.05^{0.79}}{\sqrt{2.4}\cdot(\frac{3.56E-03[m]}{6.85E-03[m]})^{0.55}} + 32.7(\frac{7.32E-06[m]}{3.56E-03[m]})^2) = 5.8E-04[m]$$

Finally, profile loss can be calculated as:

$$Y_{profile} = T_{mid}(1 - \frac{Z_{TE}}{h}) = 0.2624\cdot(1 - \frac{5.8E-04[m]}{3.56E-03[m]}) = 22.00\% \tag{4.7}$$

Secondary loss is computed as:

$$Y_{secondary} = \frac{0.038 + 0.41\cdot\tanh(1.2\cdot\delta^*/h)}{\sqrt{\cos\gamma}\cdot CR\cdot(h/C)^{0.55}\cdot(\frac{C\cdot\cos\alpha_2}{Cx})^{0.55}} = \tag{4.8}$$

$$= \frac{0.038 + 0.41\cdot\tanh(1.2\cdot 7.32E-06[m]/3.56E-03[m])}{\sqrt{\cos 64.43[^\circ]}\cdot 2.4\cdot(3.56E-03[m]/6.85E-03[m])^{0.55}\cdot(\frac{6.85E-03[m]\cdot\cos(-65.9[^\circ])}{2.96E-03[m]})^{0.55}} = 3.58\%$$

Tip leakage losses for 0.1 mm gap are computed as:

$$Y_{leakage} = Y_{total} - (Y_{profile} + Y_{secondary}) = 26.45\% - (22.00\% + 3.58\%) = 0.86\% \tag{4.9}$$

where Y_{total} is the mass-averaged overall Total Pressure losses for a given cascade based on eq. 2.7.

Mass-flow averaged total pressure loss coefficients are evaluated for case with no tip leakage and free-slip at the endwalls, at the outlets of each domain:

1. Stators:

$$Y_{stators} = \frac{P_{t1} - P_{t2}}{P_{t2} - P_2} \tag{4.10}$$

2. Rotors:

$$Y_{rotors} = \frac{P_{tr1} - P_{tr2}}{P_{tr2} - P_2} \tag{4.11}$$

where: P_{t1} and P_{t2} are the total pressures at the inlet and outlet respectively, referring to the stationary frame of reference and P_2 is the average static back-pressure. P_{tr1} and P_{tr2} are the total pressures at the inlet and outlet respectively, referring to the rotating frame of reference.

For Rotor 1, the procedure looks as follows.
Inlet BL profile for the domain can be seen in Fig. C.1b. The mean vector angle through the airfoil row is obtained also with using "Velocity Flow Angle" function in CFX and can be expressed as:

$$\tan\,\alpha_m = \frac{1}{2}(\tan\,\alpha_1 + \tan\,\alpha_2) = \frac{1}{2}(\tan\,(60.8[^\circ]) + \tan\,(-70.6[^\circ])) = -0.5[-] \tag{4.12}$$

Signs of the angles pertain to the convention described by Benner [98]. Computing arcus tangens of the expression above gives:

$$\alpha_m = \arctan\,(-0.5) = -28[^\circ] \tag{4.13}$$

Tangential loading parameter F_t yields:

$$F_t = 2(\frac{S}{Cx})\cos^2\alpha_m(\tan\,\alpha_1 - \tan\,\alpha_2) = 2(\frac{2.91E-03[m]}{4.98E-03[m]})\cos^2(-28[^\circ])(\tan\,(60.8[^\circ]) - \tan\,(-70.6[^\circ])) = 4.22[-] \tag{4.14}$$

The key variable - penetration depth, is expressed as:

$$Z_{TE} = h\cdot(\frac{0.1\cdot F_t^{0.79}}{\sqrt{CR}\cdot(\frac{h}{c})^{0.55}} + 32.7(\frac{\delta^*}{h})^2) = \tag{4.15}$$

$$= 3.04E-03[m]\cdot(\frac{0.1\cdot 4.22^{0.79}}{\sqrt{1.5}\cdot(\frac{3.04E-03[m]}{5.38E-03[m]})^{0.55}} + 32.7(\frac{3.63E-05[m]}{3.04E-03[m]})^2) = 1.1E-03[m]$$

Finally, profile loss can be calculated as:

$$Y_{profile} = T_{mid}(1 - \frac{Z_{TE}}{h}) = 0.1830\cdot(1 - \frac{1.1E-03[m]}{3.04E-03[m]}) = 11.77\% \tag{4.16}$$

Secondary loss is computed as:

$$Y_{secondary} = \frac{0.038 + 0.41\cdot\tanh(1.2\cdot\delta^*/h)}{\sqrt{\cos\gamma}\cdot CR\cdot(h/C)^{0.55}\cdot(\frac{C\cdot\cos\alpha_2}{Cx})^{0.55}} = \tag{4.17}$$

$$= \frac{0.038 + 0.41\cdot\tanh(1.2\cdot 3.63E-05[m]/3.04E-03[m])}{\sqrt{\cos 22.19[^\circ]}\cdot 1.5\cdot(3.04E-03[m]/5.38E-03[m])^{0.55}\cdot(\frac{5.38E-03[m]\cdot\cos(-70.6[^\circ])}{4.98E-03[m]})^{0.55}} = 7.45\%$$

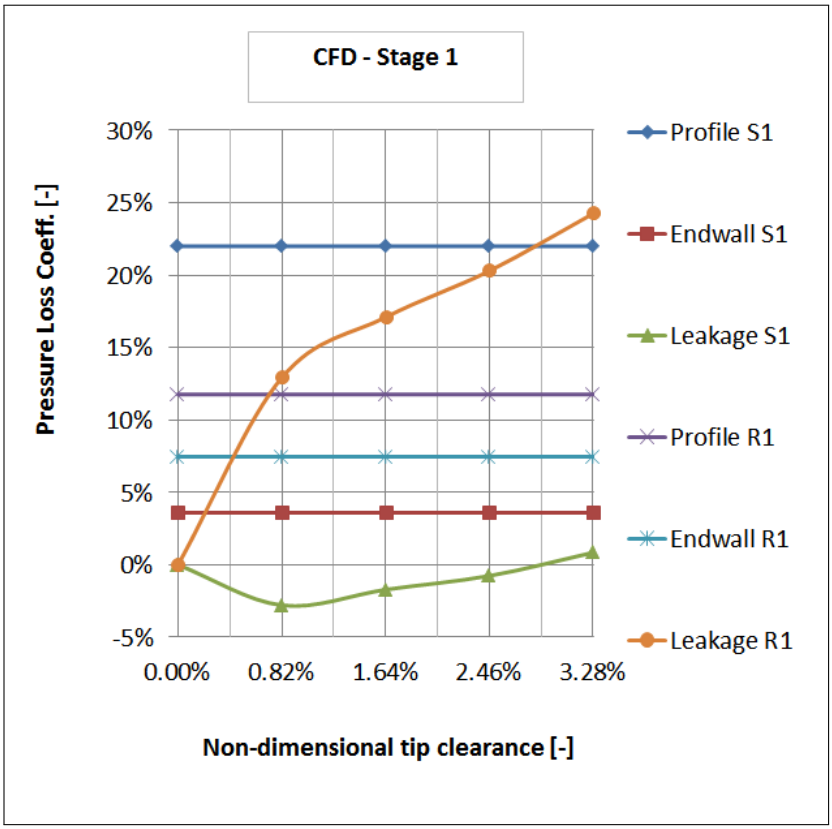

Figure 4.19: Loss breakdown w.r.t. tip clearance based on [98] and [99]

Detailed breakdown showing contribution of each type of loss ca be seen in the Fig. 4.20a and 4.20b. Expectedly, profile loss in the Stator 1 is prevailing due to aforementioned reasons.

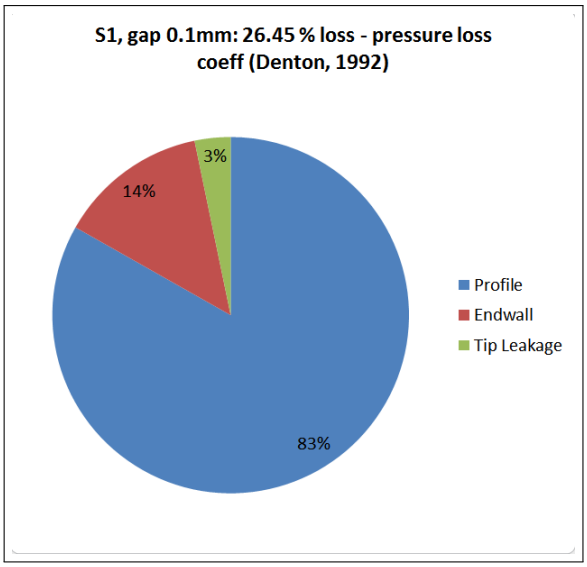

(a) Loss breakdown based for Stator 1

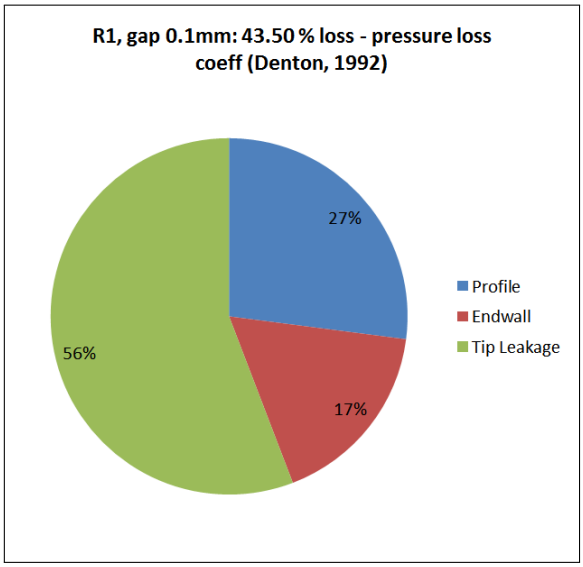

(b) Loss breakdown based for Rotor 1

Figure 4.20: Pressure-based loss breakdown based on [98] and [99]

Expectedly, in the Rotor 1 domain, tip leakage is the most deleterious contribution. Secondary losses are relatively small and hint the possibility of using low-cost 2D optimisation methods.

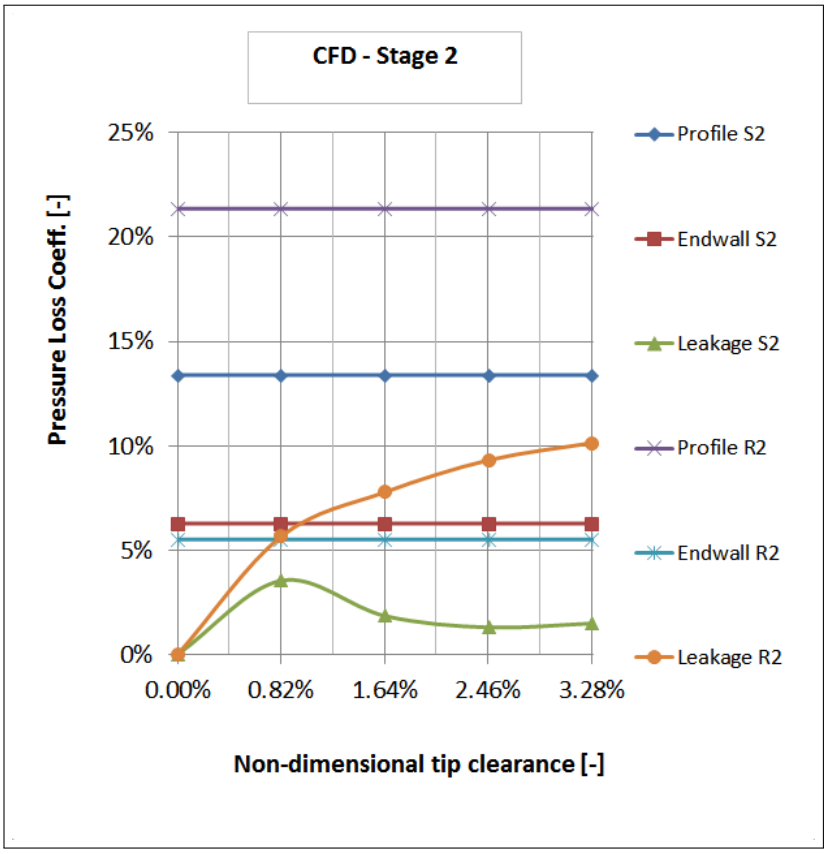

Figure 4.21: Loss breakdown w.r.t. tip clearance based on [98] and [99]

Detailed breakdown showing contribution of each type of loss ca be seen in the Fig. 4.22a and 4.22b. Expectedly, secondary losses are relatively small but for Stator 2 they account for almost 1/3 of overall loss, just like in conventional machines.

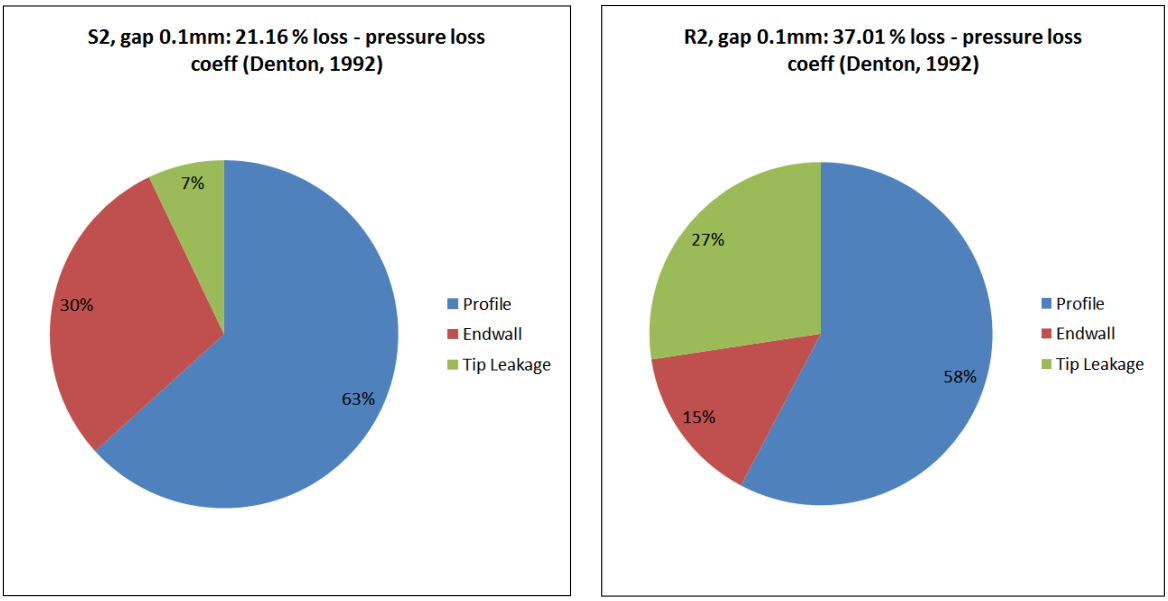

(a) Loss breakdown based for Stator 2

(b) Loss breakdown based for Rotor 2

Figure 4.22: Pressure-based loss breakdown based on [98] and [99]

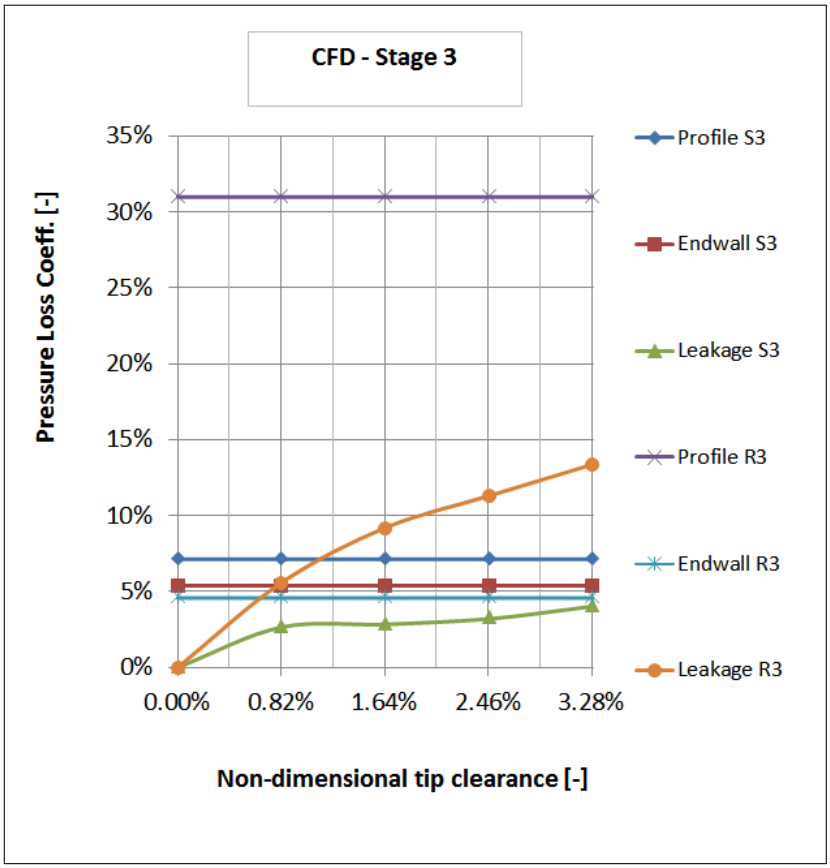

Figure 4.23: Loss breakdown w.r.t. tip clearance based on [98] and [99]

Detailed breakdown showing contribution of each type of loss ca be seen in the Fig. 4.24a and 4.24b. Expectedly, secondary losses are relatively small but for Stator 3 they account for 1/3 of overall loss, just like in conventional machines. Also, as expected, profile loss stands for the vast majority in Rotor 3.

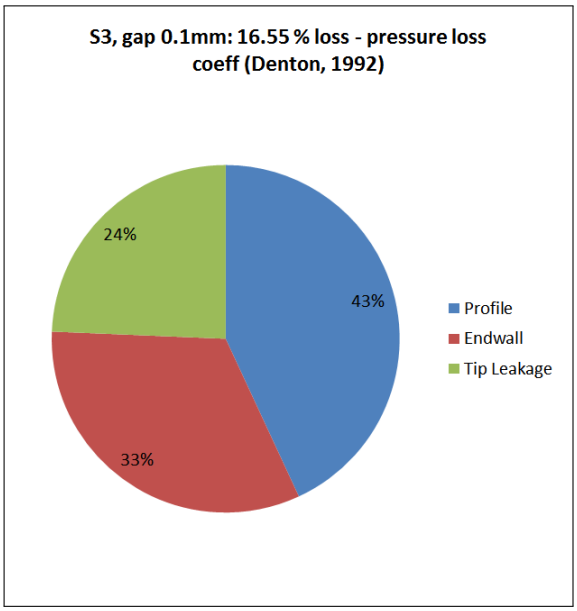

(a) Loss breakdown based for Stator 3

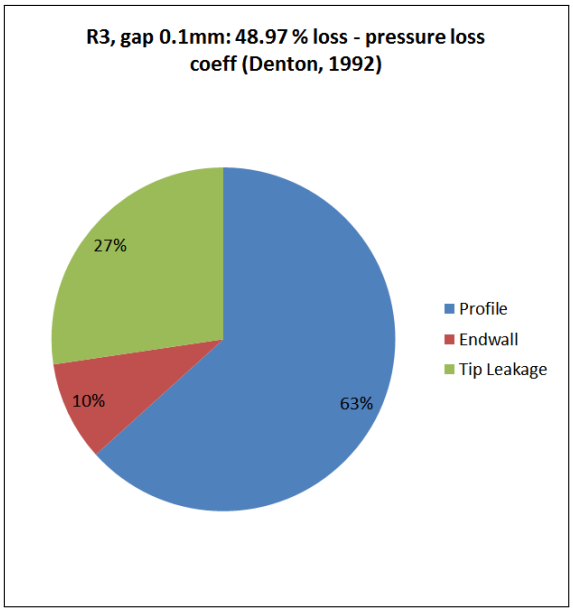

(b) Loss breakdown based for Rotor 3

Figure 4.24: Pressure-based loss breakdown based on [98] and [99]

It can be seen that:

1. Stator 1, Rotor 2 and Rotor 3 are distinguished by the highest profile losses
2. Except Rotor 1, profile losses are the main source of loss
3. Assumption of sealed stationary domains can possibly disturb the trend of rising tip leakage losses at stators
4. Secondary losses are always smaller than profile losses but not negligible, hence it is difficult to decide whether 2D optimisation methods can be successfully used to improve the performance.
5. Stator 3 distinguishes by the smallest overall total pressure loss coefficient

4.5. CFD AND ZTURBO

The aim of a mean-line, in-house design tool for ORC turbines, zTurbo is to enable preliminary fluid-dynamic design and to eliminate the limitations on adopted working fluid and flow regime [13]. Loss model applied in the code follows the methodology proposed by Traupel [74].

The principal geometrical and physical parameters considered in the model are: flow deflection, blade aspect ratio, solidity, trailing edge thickness, surface roughness, Reynolds and Mach numbers and incidence angles (off-design conditions).

It can be seen, that:

1. Profile losses obtained by zTurbo take up much smaller fraction of the overall loss w.r.t. CFD. An exception is the case of Rotor 1, where profile loss estimated by zTurbo is equal to the one of CFD. A tremendous discrepancy (65%) occurs for the Stator 1, where CFD results show that profile loss is the main source of loss in this cascade.
2. Overall loss for Stator 1 estimated by CFD is by almost 6% smaller than that of mean-line prediction. Similar trend occurs for the other stationary domains, Stator 2 and Stator 3 where the discrepancy is of 10% and 4%, respectively. This is arguably due to modelling these cascades as fixed in CFD due to the possibility of applying almost hermetic sealing on the shaft [57].
3. Rotating domains, involving 0.1 mm gaps exhibit larger overall losses to that of mean-line prediction. The aspect ratios of the blades in the considered mini-ORC ROT configuration are small, in the order of 0.51-0.68. The interaction between the tip leakage vortex (see: 4.6b) and the secondary flow is hence larger w.r.t. blades characterised by bigger aspect ratios. Low aspect ratio in small-scale machines can contribute to higher secondary losses w.r.t. larger turbines due to counter-rotating passage vortices which are close to each other. This transfer of vorticity from meridional plane to secondary plane is essentially inviscid, hence it is not itself a loss. The loss results due to mixing because it increases the mixing downstream between BL flow with high entropy and the mainstream flow. This enhanced mixing results in larger entropy generation also seen in the Fig. 4.1b. Fig. 4.7b shows that Rotor 3 is notably badly positioned with respect to relative velocity leaving Stator 3 and the stagger angle requires modification.
4. The fractions of tip leakage losses obtained by zTurbo are noticeably larger, except the case of Rotor 1 where this discrepancy is in the order of 3%. Figure 4.19 shows that tip leakage for the Rotor 1 is almost 2.5 times larger w.r.t. Rotor 2 for the tip clearance of 3.28%. However, Fig. 4.16b shows that the entropy discontinuity at the first stage interface is non-negligible and hence can affect performance parameters.
5. Endwall losses are generally smaller for CFD results, except Stator 2, where this discrepancy is of 4%. From the obtained data it can be seen that although in the CFD results endwall losses are always smaller than profile loss, they are not negligible and have to be accounted for in the blade design.

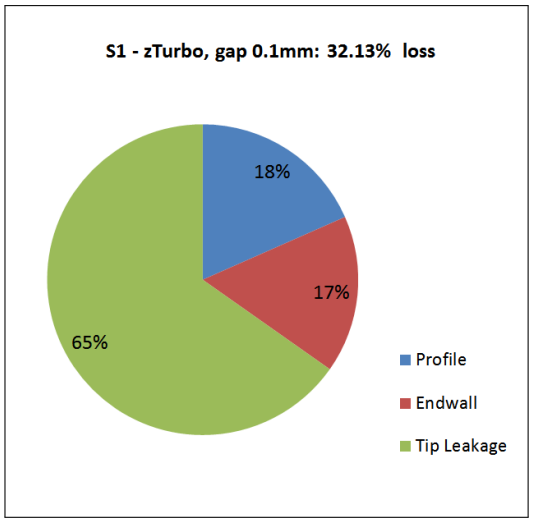

(a) Stator 1

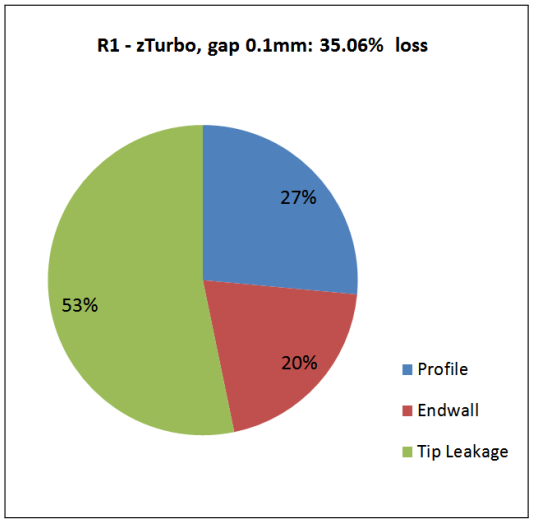

(b) Rotor 1

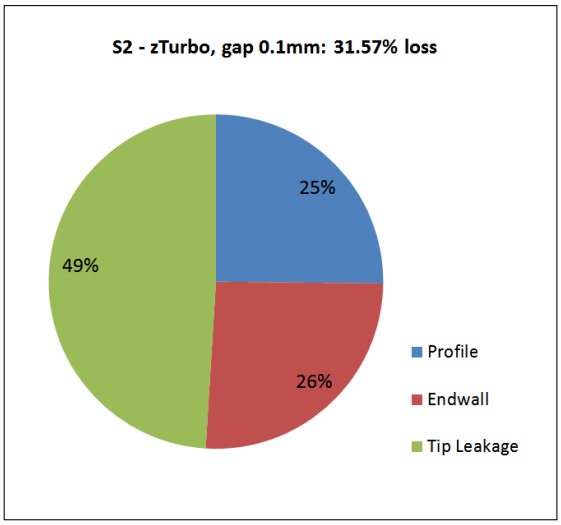

(c) Stator 2

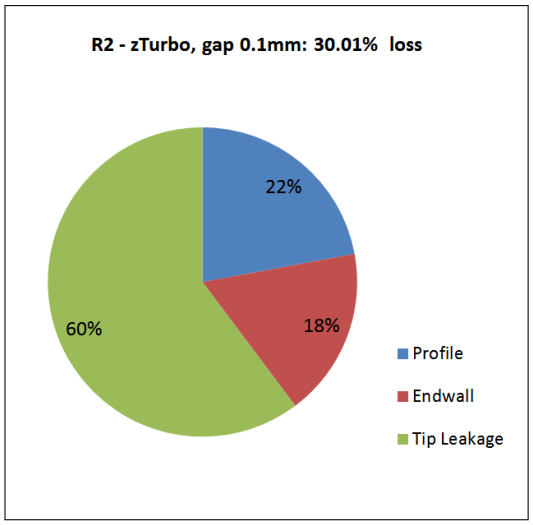

(d) Rotor 2

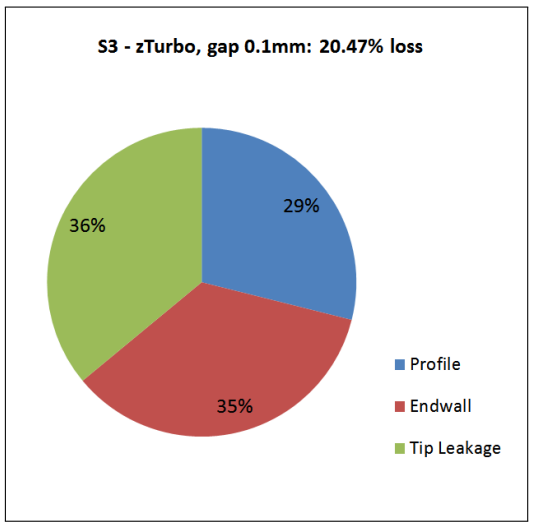

(e) Stator 3

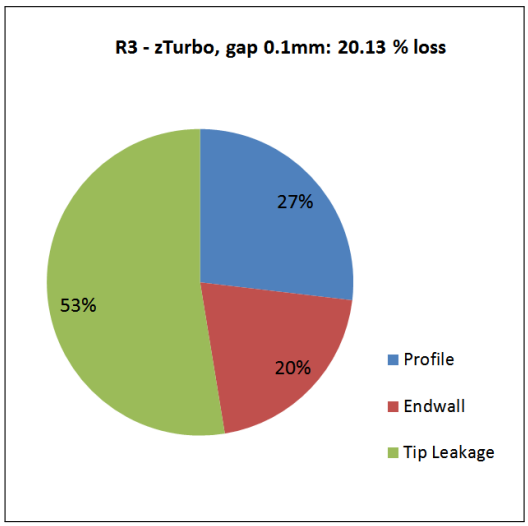

(f) Rotor 3

Figure 4.25: Loss breakdown proposed by Traupel [74] implemented in zTurbo

zTurbo computes kinetic energy loss coefficient w.r.t. isentropic velocity. To compare overall losses with the CFD, a common approach is required. Models compared have 0.1 mm leakage gap.

4.5.1. COMPARISON BASED ON ENTROPY LOSS COEFFICIENT

Entropy loss coefficient has been defined as follows:

1. Stators:

$$\zeta_{s-stators} = \frac{T_2 \cdot (s_2 - s_1)}{0.5 \cdot v^2} \tag{4.18}$$

2. Rotors:

$$\zeta_{s-rotors} = \frac{T_2 \cdot (s_2 - s_1)}{0.5 \cdot w^2} \tag{4.19}$$

where s is the entropy, point 1 and 2 refer to inlet and outlet flow, respectively and v and w refer to absolute and relative velocity, respectively. Inlet and outlet pertains to domain boundary of the given cascade. Table 4.5 presents the results of overall comparison.

Table 4.5: Overall loss comparison between CFD and zTurbo based on entropy loss coefficient

Row	**CFD**	**zTurbo**	Δ	**Row**	**CFD**	**zTurbo**	Δ	**Row**	**CFD**	**zTurbo**	Δ
1	21.12	24.46	3.3%	**3**	15.80	23.45	7.7%	**5**	12.69	12.82	0.1%
2	27.58	27.73	0.1%	**4**	18.66	21.63	3.0%	**6**	12.68	12.45	-0.2%

From the Table 4.5, it can be seen that:

1. The biggest discrepancies occur for: Stator 1, Stator 2, Rotor 2
2. Very good match, within 0.2% occurs for Rotor 1, Stator 3 and Rotor 3

4.6. DIMENSIONLESS STAGE ANALYSIS

Tip leakage and its interplay with secondary flows affect the degree of reaction, flow coefficient and load coefficient - factors which help to roughly predict the performance of the stages.

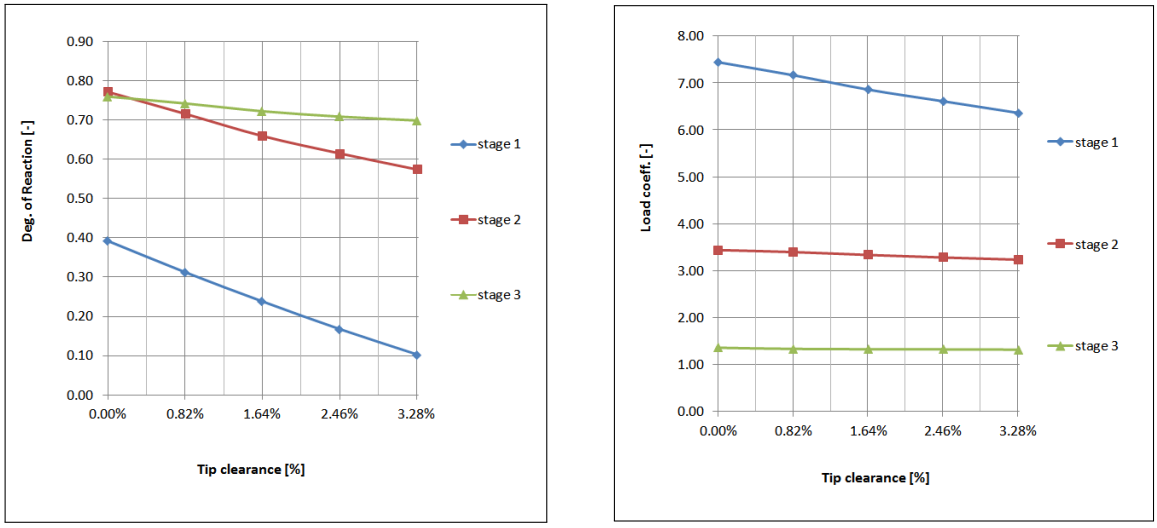

(a) Degreee of reaction

(b) Load coefficient

Figure 4.26: Dimensionless stage analysis w.r.t. tip clearance

Low degree of reaction for the first stage results in high velocities and expansion occurring more in the stator. Low degree of reaction is suitable for compact machines, according to [6] the efficiency can be higher for load coefficients larger than 3.0, which is the case as seen in Fig. 4.26b. Low flow coefficients boil down to higher efficiency and favourable lower velocities. Fig. 4.27a shows that an increase in tip clearance gap contributes to higher flow coefficient, except third stage where this trend is vanishing. Relatively low values of load coefficient w.r.t. centripetal turbines (where it is of 8-12 [6]) result in smaller specific work done by the stage and hence less severe aerodynamic loading. This results in smaller deflection and forces resulting in a decrease of the region of flow deceleration. Resulting lower dissipation coefficient implies lower shear stresses and therefore lower fluid dynamic losses and larger efficiency.

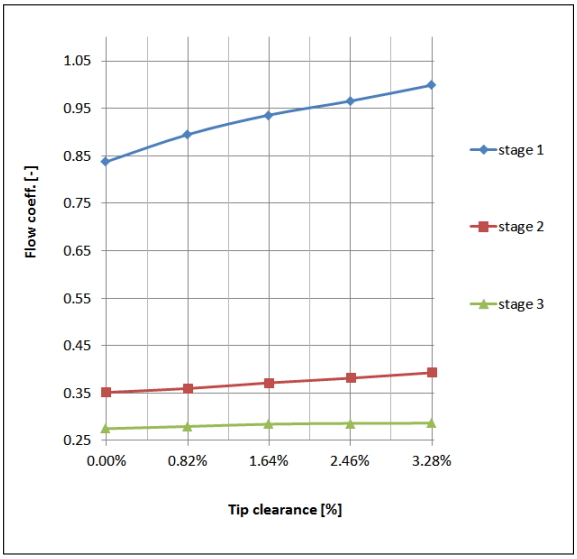

(a) Flow coefficient

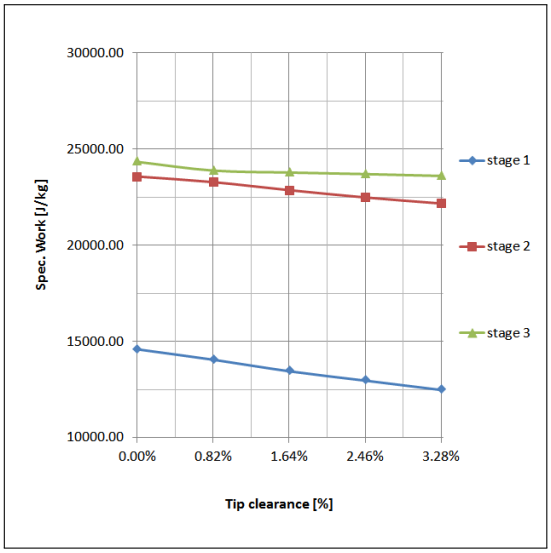

(b) Specific work

Figure 4.27: Dimensionless stage analysis w.r.t. tip clearance

The load coefficient on the first stage is decreased compared to the initial design by applying larger blade solidity of 2.25 due to increased number of blades from 8 do 12 w.r.t. initial case where the separation at the first stator was large, see Fig. A.3a. Smaller pitch results in lower aerodynamic forces on the blade. According to Fig. A.3b low deflection has been also decreased resulting in off-loading this cascade at the expense of lower specific work. Larger wetted area contributes to bigger drag which acts only on the axial component but the flow can be 'guided' more precisely. Blade solidity is an important parameter which is often an optimisation variable to decrease BL dissipation. Flow coefficient has been defined as:

$$\phi = \frac{v_m}{U_{aver}} \tag{4.20}$$

where: v_m is the meridional (radial) velocity component and U_{aver} is the average peripheral speed of the given rotor. Load coefficient has been defined as:

$$\lambda = \frac{w}{U_{aver}^2/2} \tag{4.21}$$

where: w is the specific work of the stage. Degree of reaction is based on [72]:

$$r^* = \frac{\Delta h_{rotor}}{\Delta h_{stage}} \tag{4.22}$$

where: Δh_{rotor} is the static enthalpy drop in the rotor and Δh_{stage} is the static enthalpy drop in the stage.

5

CONCLUSIONS AND RECOMMENDATIONS

5.1. CONCLUSIONS

Transient and steady-state CFD simulations of a mini-ORC ROT for renewable application has been performed and the results have been discussed. It can be concluded that:

1. Overall total-to-static efficiency of the machine is 65.3 % for a 0.1 mm tip leakage gap and sealed stators. It is higher, and in close proximity to the one of 63.1 % obtained by mean-line prediction tool zTurbo. Thermodynamic processes undergone by the working fluid in mini-ORC ROT can be represented by velocity triangles at midspan with a 2.2% discrepancy in overall efficiency w.r.t. two-equation, steady RANS. Relatively uniform blade load, ability to apply tight clearance, tangential deflection in rotors due to Coriolis force and the relative motion w.r.t. the casing contribute to a decrease in 3D effects. This efficiency is expected to be slightly lower if tip leakage is imposed also on the stationary domains, possibly yielding even a better match.

   Total pressure loss coefficient for the first stator, for the steady-state case without tip leakage is of exactly the same value (23%) as the one for transient simulation with free-slip endwalls, accounting only for two-dimensional effects, averaged over the oscillation period. For the rotor, where the endwall boundary layer is more disturbed, steady state case predicts this loss by 3 points higher w.r.t. transient case, which gives 28%. Together with small secondary losses predicted in the stator, accounting for only 14% of the overall loss, 2D estimation/optimisation methods can be possibly used to predict the performance. Naturally growing passage area, allowing for smaller flaring angle, contributes to a decrease in span-wise velocity components and diminishes 3D effects.

   Stage 1 proved to be more susceptible to tip leakage increase. Small aspect ratios, in the order of 0.5, in mini-ORC ramp up the impact of tip leakage vortex compared to larger, conventional machines. The poorest performance (total-to-total efficiency of 51.2%) has been noted for the third stage, which requires profile optimisation and stagger angle modification. Expectedly, increase in tip leakage gap in rotational domains, leads to rise in entropy, which is even slightly more perceivable in low-aspect ratio blades, such as Rotor 1.

2. Fluid-dynamic pattern shows shock-wave interaction in the first stage. Despite decreasing the load in the first cascade by increasing number of blades, aerodynamic performance is still poor. Small number of stages due to low enthalpy drop and low speed of sound in organic fluids lead to high Mach numbers in the first stator. Also, the contribution of increasing peripheral speed along the machine and a small decrease in passage cross section due to the presence of boundary layer in small aspect ratio blades, which is even further thickening along the machine lead to strong shock wave. It has been shown that is not itself a direct source of entropy generation but triggers a noticeable low pressure wake interfering with subsequent cascades leading to enhanced mixing and hence, entropy generation. Transient simulation showed that the high-entropy wake impinges on the leading edge of the rotor, imposing a curl in the velocity vector and thereby making more prone to separation.

Mach number contour maps and pseudo streamlines based on time-averaged velocity showed good stagger angle for the first four, up to five cascades and a noticeable leading edge separation for the last rotor. The leading edge or at least the camber line of this rotor should be more aligned with the relative velocity at the outlet of Stator 3. Stator 1 and Rotor 3 are characterised by the highest entropy generation due to profile losses. Further analysis also showed interaction between the low pressure separation wake in the aft part of the Rotor 3 with the tip leakage jet. Expectedly, larger leakage gap resulted in proportionally bigger, under-turning tip leakage vortex decreasing the work exchange. Closer entropy generation analysis showed that for the Rotor 3, where the blade thickness is larger w.r.t. leakage gap compared to the previous cascades, mixing occurs already in the leakage channel, despite the tip leakage alleviation due to relative motion between the blade and the casing being larger. Due to tip leakage at the rotating domains, blade loading on these domains is slightly reduced due to decrease of mass-flow over the blade.

Secondary losses proved to be smaller than profile losses and peculiar due to ROT configuration. Coriolis force has been found to favourably deflect the flow tangentially for Rotor 1 and Rotor 2. These small deflections (less than 1 degree) are added to highly tangential flow, leading to higher work exchange. Flaring angle didn't show any signs of significant entropy generation. The performance and tangential flow deflection for the first stator has been noted as surprisingly high (by 7 degrees larger) w.r.t. free-slip case. Despite the presence of shearing at the endwalls and passage vortices, entropy generation in the wake is noticeably smaller. It is noteworthy, that a very peculiar convergence trend has been found for this free-slip endwall case.

3. Loss breakdown proposed by Benner [98] resulted in the most physical results but the discrepancy between the order of magnitude of the secondary losses in each cascade makes it cumbersome to conclude whether 3D effects can be neglected. It is suspected that unsteady simulation can overcome the problem of stage interfaces and even transient two-equation RANS can provide the data of higher quality. Using conventional approach, as seen in e.g. [100], led to negative endwall losses. Coull [100] managed to avoid this problem due to using approximately six times larger aspect ratios. Good match has been found between CFD and zTurbo in terms of overall loss estimation. Discrepancies for Rotor 1, Stator 3 and Rotor 3 are 0.1%, 0.1% and 0.2%, respectively. For Stator 1, Stator 2 and Rotor 2 these discrepancies are higher, of 3.3%, 7.7% and 3.0%, respectively.

4. The main design problems are: profile losses and tip leakage. The largest losses and hence design problems are located in the Stator 1, Rotor 2 and Rotor 3. From the design viewpoint, also an issue is computational time, which for transient simulation took 13 days, with only two-equation RANS. Circumferential averaging and mixing plane assumption fail to predict the exact transient interactions between the stages. Vortex structures and even entropy generation are discontinuous.

5.2. RECOMMENDATIONS

The findings, and also difficulties encountered throughout this work spark possible future paths and an outlook to the research:

1. As elaborated in the literature review, still little is known on loss mechanisms tailored to small-scale ORC turbines, especially in radial-outflow configuration. This triggers an entire spectrum of new research questions. There is a need for loss mechanisms based on a different range of applications. It is believed that with the current interest in the ORC technology and growing number of works, a contribution to the body of knowledge is expected.

2. Relatively large computational time and memory storage problems with the current organisation of cluster for the Propulsion and Power Group make it cumbersome to arrange cases requiring larger computational overhead. A very good match has been found between transient and steady-state results for the first stator but it is advised to make judgement based on larger number of configurations tested.

3. A surprisingly large entropy generation in the free-slip endwalls case (Tot. press. loss coeff. of 26%) has been found for the first stator. This, however, as explained earlier, can be unlikely related to the mesh sensitivity and requires checking larger number of cases.

A

MESH INDEPENDENCE STUDY

A.1. QUASI-3D DOMAIN

For quasi 3D cases, each subsequent mesh has been refined by ~ 20 000 more nodes. An array of quasi 3D simulations has been performed for the first stator starting from very coarse mesh of 20 000 nodes and finishing with a very dense of 160 000 nodes. Outlet has not been extended at this stage to check the influence of numerical effect due to closely positioned interface required in the full machine. Static back-pressure has been averaged circumferentially over the entire outlet so as to allow for pressure fluctuations. Almost all results converged with an RMS below 10^{-6} except the coarsest, 20 000 node mesh which converged below 10^{-4}.

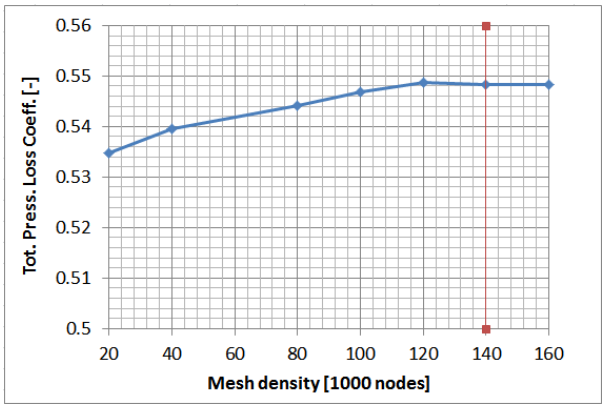

(a) Blue line - tot. press. loss coeff., red line - auxiliary line at a chosen mesh density of 140 000 nodes

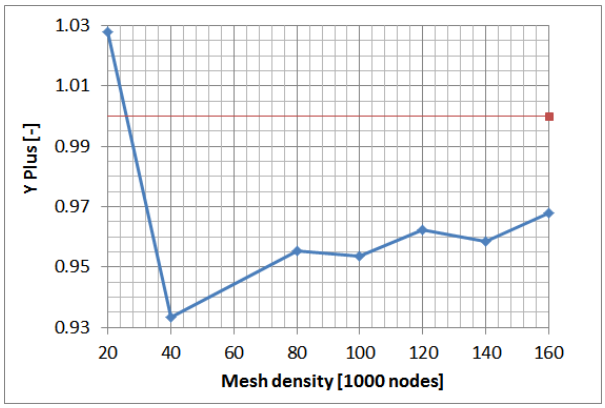

(b) Maximum Y Plus study. Blue - Values of Y Plus, red - auxiliary line at 1.0

Figure A.1: Mesh independence study for initial geometry of the first stator in quasi-3D domain, 2-cell thick mesh, SST model.

As a quasi-3D mesh, a 140 000 node grid has been chosen. The relative error in Tot. Press. Loss Coeff. with respect to the denser, 160 000 node mesh is 0.012%. As shown in the figure A.1b, maximum values of Y Plus comply with the recommended values for SST model. Relatively higher value of maximum Y Plus for a coarse, 20 000 node mesh results from unfavourable edge length ratio of the cells. To maintain prescribed amount of nodes globally, minimum Y Plus offset, and inflation rate, cells need to be more stretched along the streamlines. To decrease computational effort, a minimum of 2 cells in the span-wise direction imposes larger edge length ratios, hence the propagation of information is slower along the streamline with respect to the perpendicular direction. This has been analysed and is visualised in the figure A.2a and A.2b.

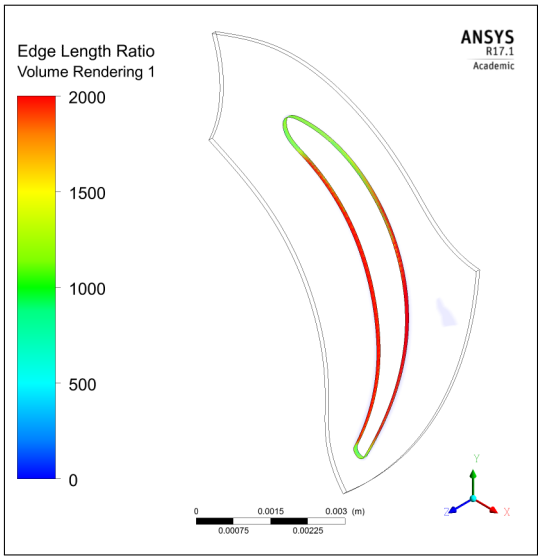

(a) 20 000 node mesh - large Edge Length Ratio

(b) 140 000 node mesh - smaller Edge Length Ratio

Figure A.2: Volume rendering of the Edge Length Ratio in the meshed quasi-3D domain

A.2. MODIFICATION IN THE FIRST STATOR'S BLADE ROW

Early results of Mach number contours showed a need to redesign the first stator blade. To relieve the cascade, also number of blades has been changed from 8 to 12.

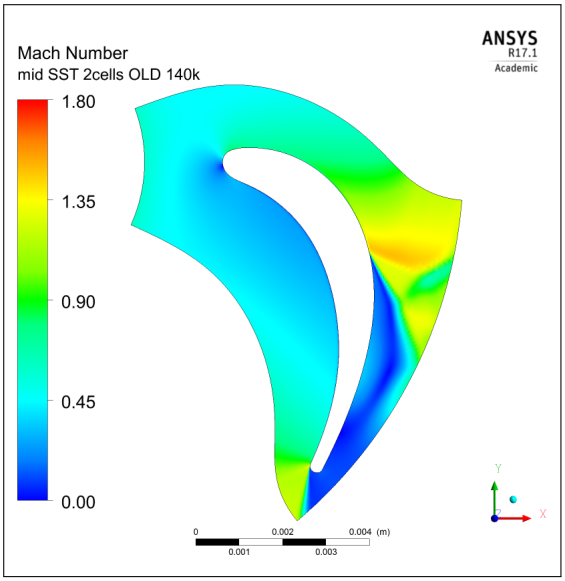

(a) Mach contours for the initial version of first stator in quasi-3D domain - large pressure gradients

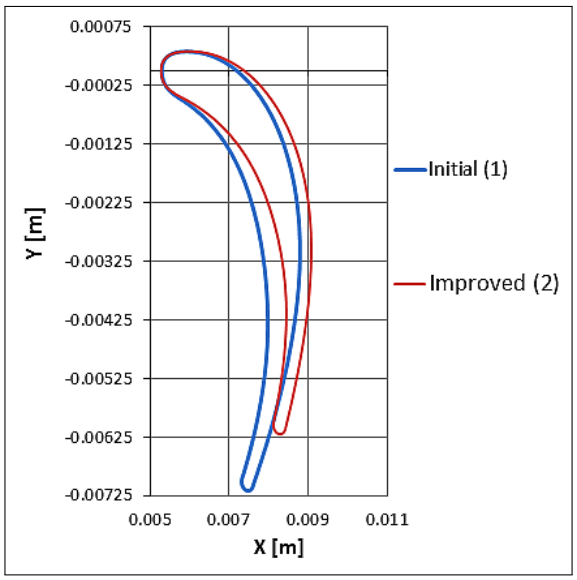

(b) Initial version (blue line) and optimised (red line) blade shape

Figure A.3: Initial geometry for the first stator (left) and required blade modification (right)

Another mesh independence study yielded optimal mesh density of 100 000 nodes. The relative error with respect to the denser 120 000 node mesh is 0.73%. Large discrepancy for meshes denser than 120 000 nodes are due to higher unsteadiness of the convergence. Bigger number of cells, yields larger amount of terms to model (resolving smaller scales) and transient effects can come into play - particularly visible in the convergence rate of total-to-static or total-to-total efficiency.

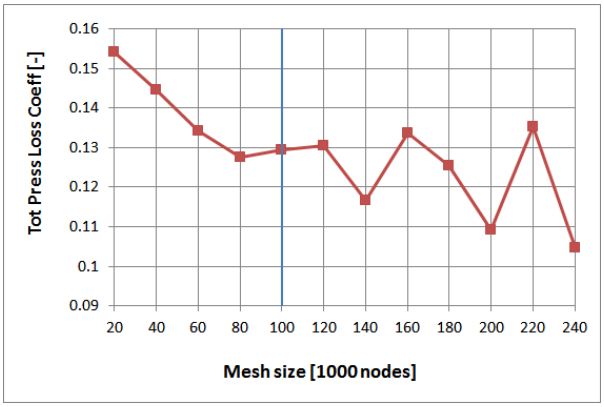

(a) Red - Tot. press. loss coeff., Blue - aux. line to indicate chosen density

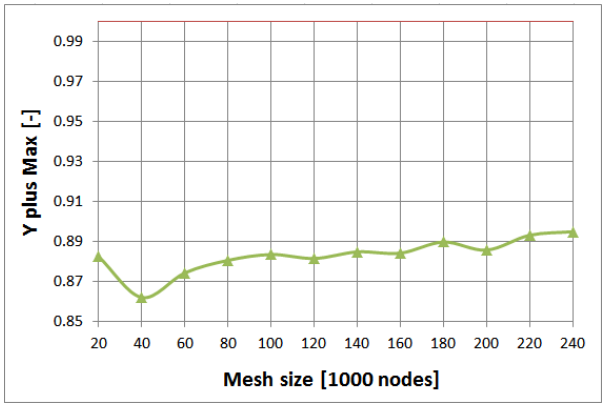

(b) Green - maximum Y Plus, pressure averaged circumferentially

Figure A.4: Mesh independence study for the first stator - redesigned, 2-cell thick mesh, SST model.

All the values of Y Plus Max remain below 1.0 due to using SST model. Similarly, no prolonging of the domain has been done at this stage. The static back-pressure is assumed averaged over the outlet circumference. Meshes between 20 000 and 100 000 nodes inclusively converged with the RMS of 10^{-5} whereas meshes between 120 000 and 240 000 converged to 10^{-4} with significantly larger oscillation periods. The value of total pressure loss coefficient reduced significantly from almost 0.55 to 0.13 [-].

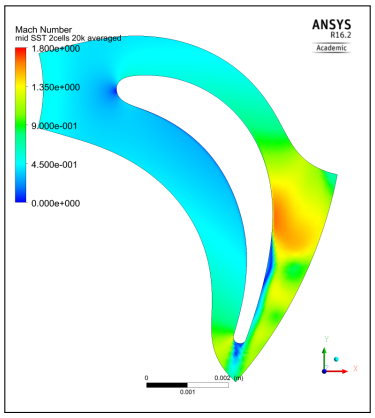

(a) 20 000 node mesh, quasi-3D, SST

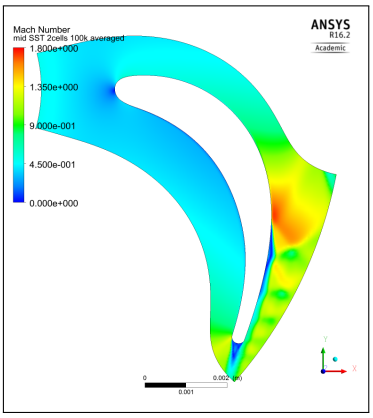

(b) 100 000 node mesh, quasi-3D, SST

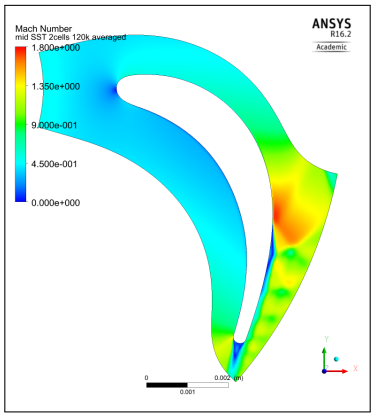

(c) 120 000 node mesh, quasi-3D, SST

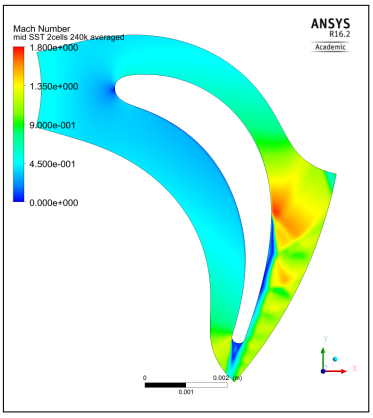

(d) 240 000 node mesh, quasi-3D, SST

Figure A.5: Mesh independence study for quasi-3D domain.

The effect of circumferential averaging becomes more profound with the denser meshes. Imposing static back-pressure circumferentially and large pressure differences in this region results in 'un-physical' (yellow/orange) spots. This numerical effect confirms that for the analysis of the full machine either larger spaces between domains are needed, which is not possible, either a time-marching solution.

A.3. 3D DOMAIN

3D meshes have been refined by 500 000 nodes each beginning from 250 000 node mesh up to 2500 000 nodes. Because 500 000 and 1000 000 mesh domains yielded similar values, an additional domain of 750 000 nodes has been tested. Meshes for node number higher than 2500 000, such as 5000 000 nodes, began to result in unsteady convergence due to similar reasons as in quasi-3D domain. This 750 000 node mesh has been chosen as an optimum wherein the relative error in Total Pressure Loss coefficient with respect to the denser domain of 2500 000 nodes is 1.45%. Since the blade sizes are comparable to each other the order of magnitude has been applied to the remaining cascades.

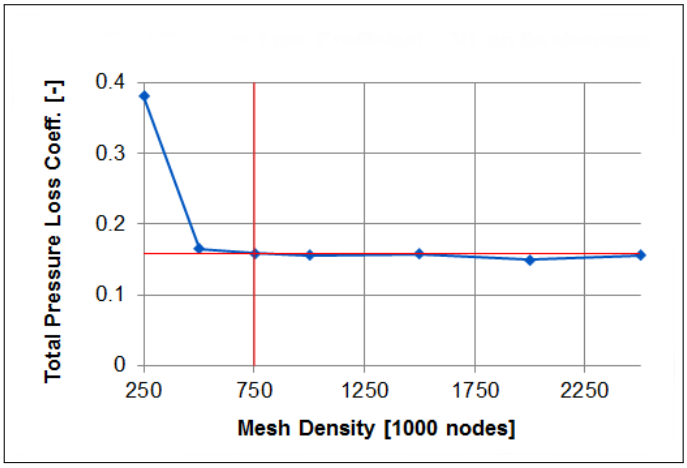

Figure A.6: Mesh independence study for 3D domains

B

ADDITIONAL FIGURES

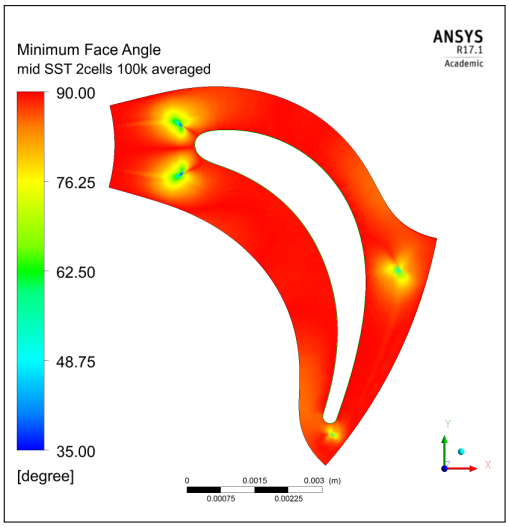

(a) Minimum Face Angle for quasi-3D domain of the first stator

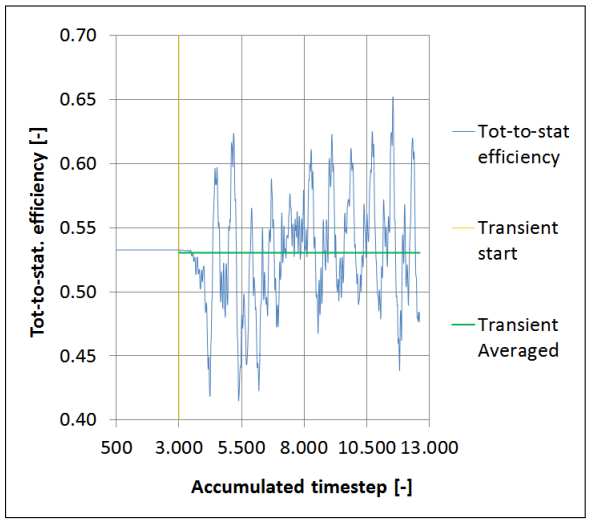

(b) Transient oscillations averaged over the unsteady simulation period

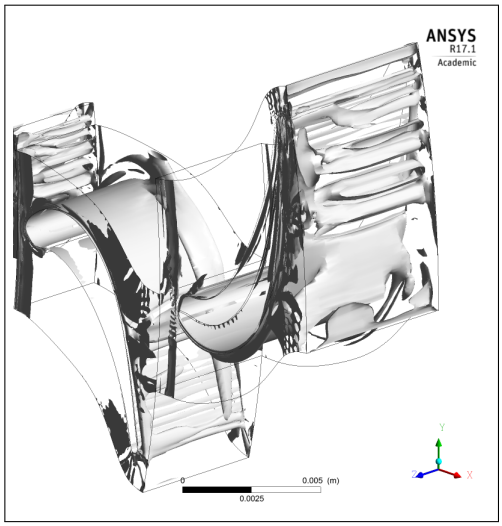

(c) Vortex structure discontinuity

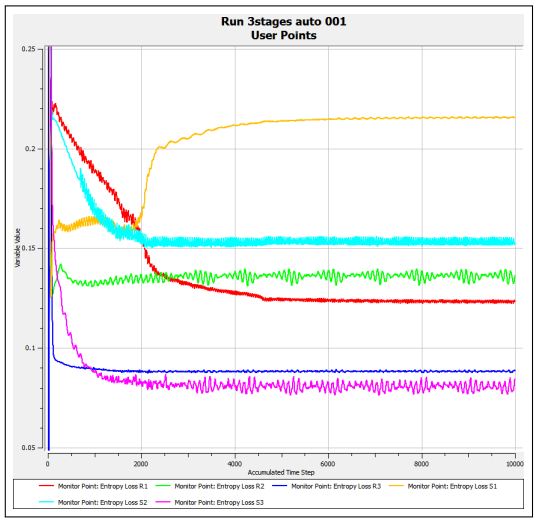

(d) Monitor points for free-slip endwall case

Figure B.1: Additional images

C

Domain Inlet Boundary Layers

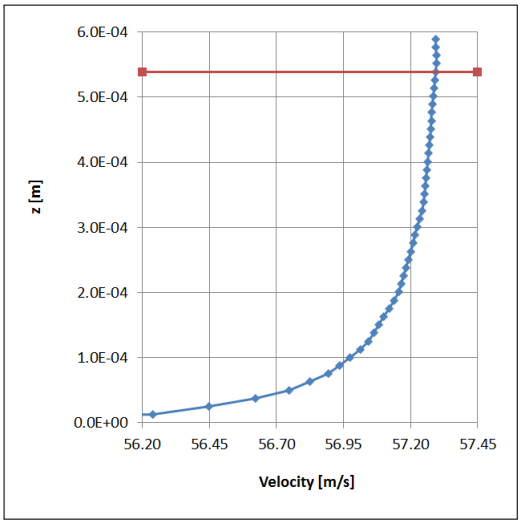

(a) Stator 1 inlet BL

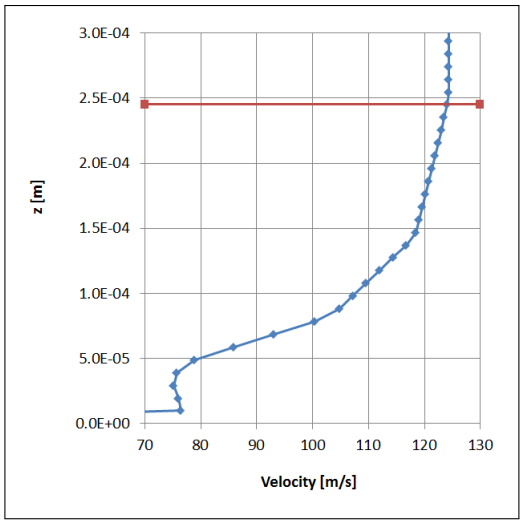

(b) Rotor 1 inlet BL

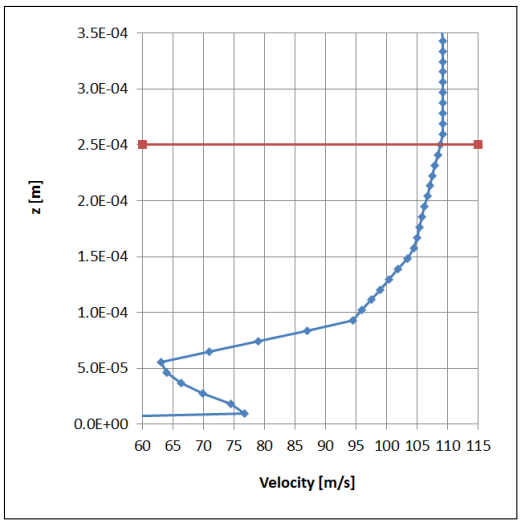

(c) Stator 2 inlet BL

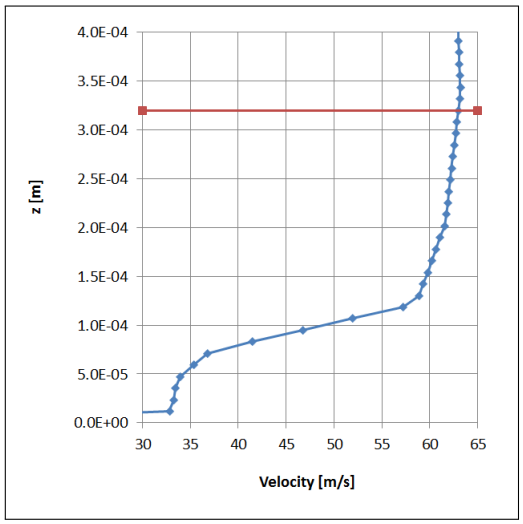

(d) Rotor 2 inlet BL

Figure C.1: Domain inlet BLs

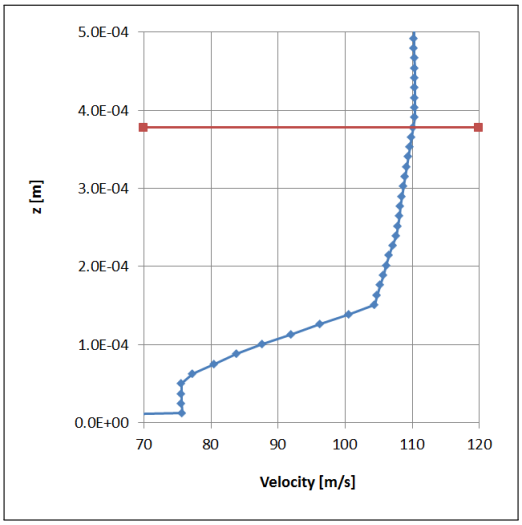

(a) Stator 3 inlet BL

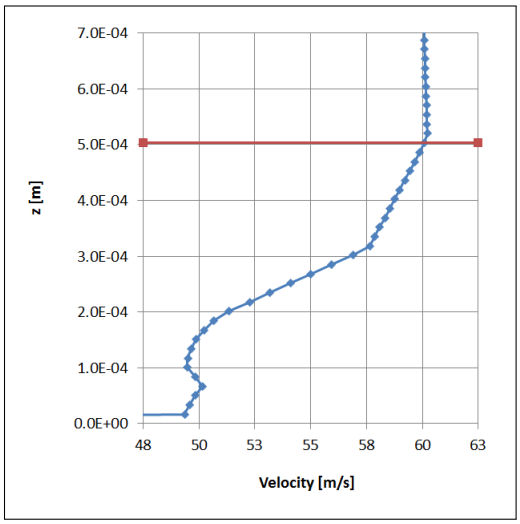

(b) Rotor 3 inlet BL

Figure C.2: Domain inlet BLs

BIBLIOGRAPHY

[1] B. Towler, *The Future of Energy 1st Edition.*

[2] M. Pini, *Preliminary design of a centrifugal turbine for organic rankine cycle applications,* ASME Journal of Engineering for Gas Turbines and Power **135**, 042312 (1 (2013).

[3] I. Obernberger, *State-of-the-art and future developments regarding small-scale biomass chp systems with a special focus on orc and stirling engines technologies,* Proceedings of the International Nordic Bioenergy Conference, Jyva¨skyla¨, Finland, September 2–5 (2003).

[4] E. Prabhu, *Solar trough organic rankine electricity system (stores). stage 1. power plant optimization and economics,* National RenewablevEnergy Laboratory (US), Technical Report No. NREL/SR-550-39433 (2006).

[5] M. Gross, *Looking for alternative energy sources,* Current Biology **22**, R103–R106 (2012).

[6] M. Pini, *Turbomachinery lecture, faculty of aerospace engineering, tu delft,* .

[7] J. Nouman, *Comparative studies and analyses of working fluids for organic rankine cycles - orc,* .

[8] E. Wanga, *Study of working fluid selection of organic rankine cycle (orc) for engine waste heat recovery,* Energy **36**, 3406–3418 (May 2011).

[9] G. Angelino, *A review of italian activity in the field of organic rankine cycles,* International VDI ORC HP Technology Working Fluids Problems, Zurich, Sept. 10–12 , 465 (1984).

[10] A. Verneau, *Emploi des fluids organiques dans les turbines solaires (the use of organic fluids in the solar turbines),* Entropie **82**, 9 (1978).

[11] S. Hickel, *Cfd for aerospace engineering, faculty of aerospace engineering, tu delft,* .

[12] P. Colonna, *Organic rankine cycle power systems: From the concept to current technology, applications, and an outlook to the future,* ASME Journal of Engineering for Gas Turbines and Power **137**, 100801 (2013).

[13] E. Casati and S. Vitale, *Centrifugal turbines for mini-organic rankine cycle power systems,* Journal of Engineering for Gas Turbines and Power **136**, 122607 (2014), harvest Published online July 15, 2014.

[14] S. A. Orszag, *Analytical theories of turbulence,* Journal of Fluid Mechanics **41**, 363 (1970).

[15] R. W. C. P. Verstappen, *Direct numerical simulation of turbulence at lower costs,* Journal of Engineering Mathematics **32**, 143 (October 1997).

[16] S. Wallin, *Engineering turbulence modelling for cfd with a focus on explicit algebraic reynolds stress models,* Royal Institute of Technology, Department of Mechanics (2000).

[17] F. R. Menter, *Two-equation eddy-viscosity turbulence models for engineering applications,* AIAA Journal **32**, 1598 (1994).

[18] J. D. Denton, *Loss mechanisms in turbomachines,* ASME Journal of Turbomachinery **115**, pp. 621 (1993).

[19] F. W. Ofeldt, *Engine,* .

[20] E. Galloway, *History and Progress of the Steam Engine, With a Prcal Investigation of Its Structure and Application* (Printed for T.Kelly, London, 1836).

[21] G. Tissandier, *Moteurs a vapeurs volatiles,* La Nature , 113 (1888).

[22] A. E. Wyss, *Motorboote und Motoryachten, reprinted by Brian Hillsdon and Jim White in 1982.*

[23] F. Shuman, *The Direct Acting Solar Engine - The Prime Mover of an Immediate Future* (Review Publishing & Printing Company, 1907).

[24] L. D'Amelio, *Impiego di vapori ad alto peso molecolare in piccole turbine e utilizzazione del calore solare per energia motrice,* Industria Napoletana Arti Grafiche, Naples, Italy (1935).

[25] L. D'Amelio, *La turbina a vapore ed i cicli binari con fluidi diversi dall'acqua fra le isoterme inferiori,* L'Elettrotecnica **XXIII**, 250 (1936).

[26] H. Tabor and L. Bronicki, *Small turbine for solar energy power package : Tabor, h. and l. bronicki, national physical laboratory of israel, united nations conference on new sources of energy, rome, 1961, 24 p., illus.* Solar Energy **7**, 82 (April–June 1963).

[27] S. K. Ray, *Fluorochemicals as working fluids for small rankine cycle power units,* Adv. Energy Convers. **6**, 89 (1966).

[28] *A comprehensive review of small solar-powered heat engines: Part ii. research since 1950—'conventional engines' up to 100 kw,* Sol. Energy **43**, 197 (1989).

[29] G. Bado, *The ansaldo 35 kw solar power system,* Sun II, Proceedings of the Silver Jubilee Congress, Atlanta, GA, May 28–June 1 **2**, 1090 (1979).

[30] M. Gaia, *Experimental results of the orc engine developed for the borj cedria solar plant,* 8th Solar World Congress, Biennial Congress of the International Solar Energy Society, Perth, Australia, Aug. 14–19, 1983 **3**, 1460 (1984).

[31] J. Larjola, *Power unit for research submersible,* International Conference on Electric Ship (ElecShip 98) , 114 (1998).

[32] S. Quoilina, *Techno-economic survey of organic rankine cycle (orc) systems,* Renewable and Sustainable Energy Reviews **22**, 168 (June 2013).

[33] H. Tabor and L. Bronicki, *Establishing criteria for fluids for small vapor turbines,* SAE Technical Paper **No. 640823** (1964).

[34] *Inmis energy - www.inmis-energy.com,* .

[35] *Turboden - www.turboden.eu,* .

[36] R. Vos, *Introduction to Transonic Aerodynamics.*

[37] D. Nanno, *An rc-1 organic rankine bottoming cycle for an adiabatic diesel engine,* NASA Lewis Research Center, Cleveland, OH **Technical Report No. DOE/NASA/0302-1** (1983).

[38] D. Seher, *Waste heat recovery for commercial vehicles with a rankine process 2,* in *21st Aachen Colloquium Automobile and Engine Technology 2012, Aachen, Germany, Oct 7-9.*

[39] T. Endo, *Study on maximizing exergy in automotive engines,* in *SAE World Congress and Exhibition, Michigan, USA.*

[40] P. L. R. Bove, *Electric power generation from landfill gas using traditional and innovative technologies,* Energy Conversion and Management **47**, 1391–1401 (July 2006).

[41] D. Gewalda, *Waste heat recovery from a landfill gas-fired power plant,* Renewable and Sustainable Energy Reviews **16**, 1779 (2012).

[42] P. D. Turco, *The oregen waste heat recovery cycle: Reducing the co2 footprint by means of overall cycle efficiency improvement,* ASME 2011 Turbo Expo: Turbine Technical Conference and Exposition **Paper No. GT2011-45051**, 547.

[43] B. A. Hedman, *Status of waste heat to power projects on natural gas pipeline,* Interstate Natural Gas Association of America (INGAA), Washington DC. (2009).

[44] M. Visaria, *Steady-state and transient simulation of supertruck waste heat recovery system in gt-suite,* Cummins Inc .

[45] M. Pehnt, *Micro Cogeneration Towards Decentralized Energy Systems.*

[46] R. Dettmer, *The mighty micro,* Engineering and Technology **5**, 42 (2010).

[47] M. Kane, *Micro-cogeneration based organic rankine cycle (orc) system in a district heating network: A case study of the lausanne city swimming pool,* 1st International Seminar on ORC Power Systems (ORC2011), Delft, The Netherlands (Sept. 22–23, 2011).

[48] M. Kanea, *Small hybrid solar power system,* Energy **28**, 1427 (November 2003).

[49] S. Quoilina, *Performance and design optimization of a low-cost solar organic rankine cycle for remote power generation,* Solar Energy **85**, 955 (May 2011).

[50] W. Avery, *Renewable energy from the ocean: A guide to otec,* Oxford University Press, New York (1994).

[51] P. Bombarda, *Performance analysis of otec plants with multilevel organic rankine cycle and solar hybridization,* ASME J. Eng. Gas Turbines Power **135**, 042302 (2013).

[52] A. D. G. Conroy and L. Ayompe, *Validated dynamic energy model for a stirling engine micro-chp unit using field trial data from a domestic dwelling,* Energy and Buildings **62**, 18 (July 2013).

[53] H. U. Frutschi, *Closed Cycle Gas Turbines.*

[54] C. P. W. R. Schleicher, A. R. Raffray, *An assessment of the brayton cycle for high performance power plants,* Fusion Technology **39** (March 2001).

[55] V. Dostal, *A Supercritical Carbon Dioxide Cycle for Next Generation Nuclear Reactors.*

[56] K. Al-Attab, *Externally fired gas turbine technology: A review,* Applied Energy **138**, 474 (15 January 2015).

[57] E. Macchi, *Design criteria for turbines operating with fluids having a low speed of sound,* Closed-Cycle Gas Turbines (Lecture Series 100), von Karman Institute for Fluid Dynamics, Sint-Genesius-Rode, Belgium (1977).

[58] E. Macchi, *Efficiency prediction for axial flow turbines operating with non-conventional working fluids,* ASME J. Eng. Power **103**, 712 (1981).

[59] A. Verneau, *Small high pressure ratio turbines,* Supersonic Turbines for Organic Rankine Cycles From 3 to 1300 kW (Lecture Series 1987-07), von Karman Institute for Fluid Dynamics, Sint-Genesius-Rode, Belgium (1987).

[60] J. Hoffren, *Numerical simulation of real-gas flow in a supersonic turbine nozzle ring,* ASME J. Eng. Gas Turbines Power **124**, 395 (2002).

[61] P. Colonna, *Design of the dense gas flexible asymmetric shock tube,* ASME J. Fluids Eng. **130**, 034501 (2008).

[62] A. Spinelli, *Design of a test rig for organic vapours,* Proceedings of the ASME Turbo Expo (GT2010), Glasgow, UK, June 14–18, ASME Paper No. GT2010-22959 (2010).

[63] L. B. G. Cerri and G. Soraperra, *Non-conventional turbines for hydrogen fueled power plants,* ASME , 9 (2003).

[64] F. Ljungstrom, *The development of the ljungstrom steam turbine and air preheater,* Proc. Inst. Mech. Eng. **160**, 211 (1949).

[65] G. Lozza, *Investigation on the efficiency potential of small steam turbines of various configurations,* 21st Intersociety Energy Conversion Engineering Conference, San Diego, CA, August 25–29 , 1367 (1986).

[66] G. Persico, *Aerodynamics of centrifugal turbine cascades,* Journal of Engineering for Gas Turbines and Power **137**, 112602 (1 (2015).

[67] O. Balje, *A study on design criteria and matching of turbomachines: Part a—similarity relations and design criteria of turbines.* ASME. J. Eng. Power. **84**, 83 (1962).

[68] O. Balje, *A study on design criteria and matching of turbomachines: Part b—compressor and pump performance and matching of turbocomponents.* ASME. J. Eng. Power. **84**, 103 (1962).

[69] E. Macchi, *Design limits: Basic parameter selection and optimization methods in turbomachinery design,* Martinus Nijhoff Publisher, Dordrecht, Netherlands **97**, 805 (1985).

[70] P. Gaetani, *Effects of axial gap on the vane-rotor interaction in a low aspect ratio turbine stage,* Journal of Propulsion and Power **26**, 325 (2010).

[71] C. Rodgers, *A cycle analysis technique for small gas turbines. technical advances in gas turbine design.* Proceedings of the Institution Mechanical Engineers London, 183, Part 3 N (1969).

[72] S. Dixon, *Fluid Mechanics and Thermodynamics of Turbomachinery* (Elsevier Butterworth-Heinemann).

[73] P. Colonna, *Real-gas effects in organic rankine cycle turbine nozzles,* Journal of Propulsion and Power **24**, 282 (2008).

[74] W. Traupel, *Thermische turbomaschinen,* Springer-Verlag, Berlin (1977).

[75] H. Craig, *Performance estimation of axial flow turbines,* Proceedings of the Institution of Mechanical Engineers **185**, 407 (1970).

[76] W. Lang, *Assessment of waste heat recovery from a heavy-duty truck engine by means of an orc turbogenerator,* J. Eng. Gas Turbines Power **135** (Mar 18, 2013).

[77] C. Spadacini, *Fluid-dynamics of the orc radial outflow turbine,* Exergy SpA, Via Santa Rita 14, 21057, Olgiate Olona (VA), Italy **118**, 1 (October 2015).

[78] T. K. C. Martin, *Study of advanced radial outflow turbine for solar steam rankine engines,* .

[79] D. Wilson, *The design of high-efficiency turbomachinery and gas turbines,* MIT Press, Cambridge, MA (1984).

[80] C. Sieverding, *Recent progress in the understanding of basic aspects of secondary flows in turbine blades passages,* ASME, J. Eng. Gas Turbines Power **107**, 248 (April 1985).

[81] O. Sharma and T. Butler, *Predictions of endwall losses and secondary flows in axial flow turbine cascades,* ASME, J. of Turbomachinery **109**, 229 (April 1987).

[82] I. R. A. Duden and L. Fottner, *Controlling the secondary flow in a turbine cascade by a three-dimensional airfoil design and endwall contouring,* ASME, J. of Turbomachinery **121**, 191 (April 1999).

[83] J. Coull, *Blade loading and its application in the mean-line design of low pressure turbines,* ASME J. Turbomach. **135**, 021032 (2013).

[84] A. Howell, *Fluid dynamics of axial compressors and design of axial compressors,* Proceedings of the Institution of Mechanical Engineers **153**, 441 (1945).

[85] A. Carter, *Three-dimensional flow theories for axial compressors and turbines,* Proceedings of the Institution of Mechanical Engineers **159**, 255 (1948).

[86] E. Launder, *The prediction of laminarization with a two-equation model of turbulence,* International Journal of Heat and Mass Transfer **15**, 301 (1972).

[87] D. Ainley, *An examination of the flow and pressure losses in blade rows of axial flow turbines,* Aeronautical Research Council (ARC) (1951).

[88] A. Dahlquist, *Investigation of losses prediction in 1d for axial gas turbines,* .

[89] J. Dunham and P. M. Came, *Improvements to the ainley-mathieson method of turbine performance prediction,* J. Eng. Power **92**, 252 (Jul 01, 1970).

[90] S. C. Kacker, *A mean line prediction method for axial flow turbine efficiency,* J. Eng. Power **104**, 111 (Jan 01, 1982).

[91] M. K. Mukhtarov, *Procedure of estimating flow section losses in axial flow turbines when calculating their characteristics,* Teploenergetika **16**, 76 (1969).

[92] B. Mamaev and A. Klebanov, *Optimal pitch for turbine blade cascade,* Kuibyshev Motor Works (1969).

[93] S. H. Moustapha, *An improved incidence losses prediction method for turbine airfoils,* J. Turbomach **112**, 267 (Apr 01, 1990).

[94] M. W. Benner, *Influence of leading-edge geometry on profile losses in turbines at off-design incidence: Experimental results and an improved correlation,* J. Turbomach **119**, 193 (Apr 01, 1997).

[95] J. Zhu and S. A. Sjolander, *Improved profile loss and deviation correlations for axial-turbine blade rows,* ASME , 783 (2005).

[96] M. W. Benner, *Measurements of secondary flows downstream of a turbine cascade at off-design incidence,* ASME Proceedings - Turbomachinery , 1299 (2004).

[97] O. P. Sharma, *Predictions of endwall losses and secondary flows in axial flow turbine cascades,* J. Turbomach **109**, 229 (Apr 01, 1987).

[98] M. Benner, *An empirical prediction method for secondary losses in turbines - part 1: A new loss breakdown scheme and penetration depth correlation,* Journal of turbomachinery **128**, 273 (April 2006).

[99] M. Benner, *An empirical prediction method for secondary losses in turbines—part ii: A new secondary loss correlation,* ASME **128**, 281 (2006).

[100] J. Coull, *Endwall loss in turbine cascades,* in *Proceedings of ASME Turbo Expo 2016: Turbomachinery Technical Conference and Exposition*, edited by ASME.

[101] M. W. Benner and S. A. Sjolander, *Measurements of secondary flows in a turbine cascade at off-design incidence,* ASME (1997).

[102] A. A. Research, *Release 16.2, help system, cfx modelling guide,* ANSYS, Inc. (2016).

[103] M. Savill, *Synthesis report of the ercoftac transition modeling – transpreturb thematic network activities 1998-2002,* Ecoftac Bulletin **54**, 5 (September 2002).

[104] R. Granger, *Fluid Mechanics*.

[105] J. D. Denton and L. Xu, *The trailing edge loss of transonic turbine blades,* Journal of Turbomachinery **112**, 277 (1990).

[106] J.Delery and J.G.Marvin, *Turbulent shock-wave/boundary-layer interaction,* Advisory Group For Aerospace Research and Development , 90 (1986).

[107] Q. Roberts, *The trailing edge loss of a simulated turbine blade,* .

[108] J. P. Bindon, *The measurement and formation of tip clearance loss,* Journal of Turbomachinery **111**, 257 (1989).

[109] J. T. J. Moore, *Tip leakage flow in a linear turbine cascade,* ASME. J. Turbomach. **110**, 18 (1988).

[110] M. I. Yaras, *Effects of simulated rotation on tip leakage in a planar cascade of turbine blades. parts 1 and 2.* Journal of Turbomachinery **114**, 660 (1992).

[111] J. B. G. Morphis, *The effects of relative motion, blade edge radius and gap size on the blade tip pressure distribution in an annular turbine cascade with clearance,* ASME. Turbo Expo: Power for Land, Sea, and Air **1** (1988).

[112] G. Persico, P. Gaetani, V. Dossena, G. D'Ippolito, and C. Osnaghi, *On the definition of the secondary flow in three-dimensional cascades,* Proceedings of the Institution of Mechanical Engineers, Part A: Journal of Power and Energy **223**, 667 (2009).

[113] J. P. Bindon, *The effect of hub inlet boundary layer skewing on the endwall shear flow in an annular turbine cascade,* The American Society of Mechanical Engineers Paper No. 79-GT-13 (1979).

[114] J. A. Walsh, *Inlet skew and the growth of secondary losses and vorticity in a turbine cascade,* ASME Journal of Turbomachinery **112**, 633 (1990).

[115] R. H. R. Eymard, T. R. Gallouët, *The finite volume method,* Handbook of Numerical Analysis **7**, 713 (2000).

[116] S. V. Patankar, *Numerical Heat Transfer and Fluid Flow* (Hemisphere Publishing Corporation, 1980).

[117] D. Wilcox, *Re-assessment of the scale-determining equation for advanced turbulence models,* AIAA Journal **26**, 1299 (1988).

[118] P. R. Spalart and S. R. Allmaras, *A one-equation turbulence model for aerodynamic flows,* AIAA Paper 92-0439 (1992).

[119] G. J. R. B. E. Launder and W. Rodi, *Progress in the development of a reynolds-stress turbulence closure,* Journal of Fluid Mechanics **68**, 537 (1975).

[120] C. G. Speziale, *Second-order closure models for supersonic turbulent flows,* Institute for Computer Applications in Science and Engineering, NASA Langley Research Center, Hampton, Virginia 23665-5225 (1991).

[121] S. Pope, *A more general effective-viscosity hypothesis.* Journal of Fluid Mechanics **72**, 331 (1975).

[122] S. Jakirlic, *Assessment of the rsm, urans and hybrid models with respect to the different roadmaps including the industrial application challenges,* TU Darmstadt (June 2012).

[123] D. Peng, *A new two-constant equation of state,* Industrial & Engineering Chemistry Fundamentals **15**, 59 (1976).

[124] W. M. Kays, *Turbulent prandtl number—where are we?* Journal of Heat Transfer **116**, 284–212 (1994).